The Dissertation Committee for Gabriel Ricardo Venegas
certifies that this is the approved version of the following dissertation:

The Impact of Salinity Diffusion, Poroelasticity, and Organic Carbon in Sediment Acoustics

Committee:

Preston S. Wilson, Supervisor

Mark F. Hamilton

Michael R. Haberman

Salvatore Salamone

Kevin M. Lee

Megan S. Ballard

The Impact of Salinity Diffusion, Poroelasticity, and Organic Carbon in Sediment Acoustics

by

Gabriel Ricardo Venegas

DISSERTATION

Presented to the Faculty of the Graduate School of

The University of Texas at Austin

in Partial Fulfillment

of the Requirements

for the Degree of

DOCTOR OF PHILOSOPHY

THE UNIVERSITY OF TEXAS AT AUSTIN

August 2019

Dedicated to my wonderful “wee” wife, Toni,

and my adored parents, Jose and Magnolia.

Acknowledgments

Throughout this academic marathon, my mind has been sculpted by overcoming the countless failures. Without the emotional support from my family and the guidance of great minds, the completion of this dissertation would surely not have been possible. To the person who has always had my back and has lifted my spirits without fail from the very beginning, as my best friend, to the very end, now as my wife, Toni Kane, you are my north star when all other lights dim. To my parents, Drs. Jose and Magnolia Venegas, my most heartfelt gratitude for all of your support, love, and encouragement over the years, and for nurturing and inspiring me to pursue this path.

I would like to express my sincerest appreciation to my dissertation advisor, Dr. Preston S. Wilson, who has allowed me the freedom to pursue many diverse research topics, while always providing me a safety net to fall back on when I inevitably became overwhelmed with ideas. I am indebted to him for all of the guidance and patience he has given me during the genesis of this work, and for providing me the opportunity to collaborate with many scientists across multiple institutions.

I am extremely grateful to Dr. Kevin Lee, Dr. Megan Ballard, Dr. Jason Sagers, and Andrew McNeese from the Applied Research Laboratories (ARL), and Dr. Abdullah Rahman from The University of Texas Rio Grande

Valley for all their guidance and time, as they took me under their wings. I am truly fortunate to have coauthors and role models, such as yourselves. I would also like to extend my gratitude to Dr. Mark Hamilton, Dr. Mike Haberman, Dr. Marcia Isakson, and Dr. Preston Wilson for teaching me the necessary fundamentals in the classroom, which were instrumental to the work performed here.

I have had the great pleasure of working with some talented machinists at ARL. JR Watson, Jimmy Stork, and Charlie Crowley not only converted all my engineering drawings into parts vital to all of the studies presented here, but also for their time and feedback throughout the design process that greatly improved the overall success of the science.

My peers, your collective intellect, support, and comradery has helped me thrive in this program. I especially wish to thank Drs. Anthony Bonomo and Benjamin Goldsberry for teaching me everything I know about finite element modeling in COMSOL, and Colby Cushing for showing me the ropes of motion control using the OpenBuilds framework.

After acoustically processing more than 60 sediment cores, I am indebted to all those who helped with the coring and sediment processing. Collecting sediment cores is messy and humbling, yet imperative to the science performed during my time as a graduate student. The five one-meter-long cores presented here were among the most challenging to collect, and I have Dr. Aslan Aslan to thank for his sledgehammer prowess when my arms could hammer no more. In addition, I gratefully acknowledge the help of under-

graduate research assistants Kimbell Bui and Sara Fernandez de la Vega, and graduate research assistant, Ivy Hinson, for their hard work and long hours of sediment processing. Without their efforts, this degree would have taken even longer to complete.

Lastly, I would like to acknowledge the Elizabeth L. & Russell F. Hallberg Foundation Graduate Fellowship in Engineering Acoustics, the Office of Naval Research, and the Applied Research Laboratories Independent Research and Development Program for funding this work.

The Impact of Salinity Diffusion, Poroelasticity, and Organic Carbon in Sediment Acoustics

Publication No. _____

Gabriel Ricardo Venegas, Ph.D.
The University of Texas at Austin, 2019

Supervisor: Preston S. Wilson

To optimize the use of sound in waters on the continental shelf for naval, commercial, and environmental monitoring applications, the acoustic properties of the ocean bottom must be well understood. The effects of 1) pore water salinity variability on acoustic reflectivity, 2) poroelasticity on geoacoustic inference, and 3) organic carbon on sediment properties were formerly-considered insignificant in sediment acoustics, but due to advancements in other areas of underwater acoustics systems and modeling, have now become significant. Three separate but related studies were conducted to begin to quantify these effects. 1) A high-frequency acoustic reflection experiment was performed on a water-clay interface, while varying the salinity of the water. Results demonstrated significant changes in reflectivity at high incident angles, as well as a transient effect explained by a new coupled salt diffusion/reflection model. Using the model, the effective diffusion coefficient of salt in clay was inferred from the experiment, and reflectivity was then simulated at lower frequencies

and longer time-scales. From this modeling effort, at a given time-scale of fluctuation, a characteristic frequency was identified, below which the reflectivity should not be assumed temporally invariant. 2) A model geoacoustic inference procedure was performed on a layered waveguide consisting of water and water-saturated glass beads contained within a glass tube. The resonance frequencies of the system were measured and compared with simulations of the experiment. Within each simulation, various sediment acoustics models were used. The only model that allowed for self-consistency between the inference and an independent set of high-frequency sound speed measurements, was a model that accounted for poroelastic effects. 3) A sediment constituent that has great value to the planet and is ubiquitous in natural marine sediment, organic carbon, has been ignored in sediment acoustics models. To begin to explore this relationship, sediment cores were extracted from a *T. testudinum* seagrass meadow in the Lower Laguna Madre, Texas, USA. A strong correlation between organic carbon and the primary-wave modulus was identified using a custom-built automated broad-band core and resonance logger and an elemental analyzer. The sediment properties attained from the cores were compared, and a theory explaining the correlations was developed. The acoustic sensitivity to organic carbon in a seagrass meadow has demonstrated promise toward developing an acoustic tool to more rapidly quantify marine organic carbon stores, which is needed in climate science. However, a larger-scale study is required to determine its applicability across a broader range of seagrass meadows and sediment types.

Table of Contents

List of Tables

List of Figures

Chapter 1

Introduction

A brief background is provided on the importance of coastal ecosystems and its ties to humankind and the field of shallow water acoustics. Then, a more focused discussion into some of the challenges associated with marine sediment acoustics is provided, including three physical effects often ignored in application. To this end, three separate, but related studies addressing these effects are presented. Lastly, the contents of this dissertation are outlined.

1.1 The importance of coastal ecosystems

Despite covering less than 8% of the ocean's surface area, the continental shelf is home to most oceanic life [1]. This is, in part, due to light's ability to penetrate into the shelf's shallow depths (< 150 m), and allows for primary production to occur, not just within the water column, but on the nutrient-rich terrigenous sediments that comprise the seafloor. Found closer to shore, estuaries, salt marshes, mangrove forests, and seagrass meadows are among some of the most productive and dynamic ecosystems on the planet. Ecosystems such as these provide nesting and feeding grounds for many animals, and estuaries provide humans with strategic port cities, using the rivers to trans-

port goods inland. In fact, twenty-two of the thirty-two largest cities of the world are located in estuaries [2]. Humans have relied on these accumulations of life for thousands of years, accounting for 90% of fishery production worldwide [3]. In addition, one-third of planet's oil and gas reserves are estimated to be deposited within continental shelf and margins [1].

Nations only began to realize the economic value of the shelf in 1930, which, at that time, restricted maritime ownership to only three miles past their shores. The US was the first to gain control of their continental shelf after the Second World War (WW2), although SOund Navigation And Ranging (SONAR) capabilities in the deep ocean were in their naissance. It was not until the end of the Cold War, when strategic interests shifted from the deep ocean to shallower water, such as the continental shelf, bays, harbors, and even riverine environments, fostering applications such as shallow water sonar, port protection, and mine hunting. Aside from military applications, systems that use sound on the shelf have been commercialized and are used to monitor fishery and marine mammal populations, for oil and gas exploration and drilling, underwater communications, as well as the removal of unexploded ordinances in civilian-populated maritime areas. These are a few of the many ways humans exploit sound within the continental shelf.

Although the relationship between humans and these valuable marine ecosystems have been strategically and commercially fruitful, anthropogenic activity has caused these ecosystem to be among some of the most threatened on earth [4, 5]. Salt marshes, mangrove forests, and seagrass meadows are ex-

tremely efficient at converting carbon dioxide (CO_2) into organic carbon and burying it within the sediment. In fact, they comprise, by area, less than 2% of the ocean, yet account for half of all organic carbon stored annually in ocean sediments [6]. As they become damaged and begin to disappear, not only are there fewer carbon sinks left to help absorb anthropogenic emissions, the carbon stores become carbon sources, leading to even higher CO_2 concentrations [7]. Therefore, it is not surprising that the protection and monitoring of these organic carbon sinks is considered vital to mitigate climate change [4]. To quote the French explorer, scientist, naval officer, and conservationist Jacques-Yves Cousteau, "For most of history, man has had to fight nature to survive; in this century he is beginning to realize that, in order to survive, he must protect it" [8]. Perhaps in studying the challenges associated with the human exploitation of sound in a shallow-water environment, some of the findings can be applied to help these environments survive. However, more investigation pertaining to sound propagation in marine sediments is warranted to improve the performance of acoustic applications in shallow water.

1.2 Challenges in shallow-water acoustics

To give some perspective as to the challenges acoustic applications face when operating on the continental shelf, consider the aspect ratio of a typical shallow water waveguide. Continental shelves have an average depth of 60 m, while the range for certain shallow water sonar applications can be on the order of 30 km (500 water depths). For such a waveguide, there are significantly

more acoustic interactions with the seabed than compared with the deep ocean, and sound propagation can, therefore, be highly dependent upon the acoustic properties of the sediment. In addition to the acoustic interactions with the ocean bottom increasing in complexity as the waveguide becomes shallower, the sediment itself becomes more spatially variable and poorly sorted depending upon the energy state of the physical oceanography [1, 9]. Grains that comprise much of the inorganic constituents in marine sediment can vary in diameter by up to 6 orders of magnitude [10]. Generally in shallow high-energy environments, near the tidal zone for example, mostly coarser sand grains settle [9]. Finer particles, such as silt and clay, remain in suspension and are carried to lower-energy areas, such as deep ocean basins, and can take decades to settle to the seafloor [1]. However, fine particles may settle sooner either by bonding to suspended organic matter to form larger flocs, referred to as "marine snow," or by being digested by microalgae or benthic infauna and consolidated into fecal pellets [11]. These flocs can settle on the shelf or get trapped in estuaries, wetlands, mud banks, and seagrass meadows.

The ocean is a spatiotemporally varying system. Acoustic effects of temperature and salinity fluctuations in the water column in the form of salt wedges, internal waves, currents, etc., have been well studied [12, 13]. However, in many applications, the sediment pore water is assumed to be equal to the water above the sediment, which is commonly referred to as "bottom water." The concept of a sound speed ratio, or the ratio between sediment sound speed normalized by the sound speed of the bottom water was defined

on this assumption [14]. This formalism is useful, when the assumption is valid, because if the sound speed ratio was measured in a previous experiment or in the laboratory, the *in situ* sediment sound speed can be calculated by multiplying the sound speed ratio by the sound speed of the bottom water. This quasi-static assumption is violated in many instances, particularly with fine-grained sediments. For example, the effects of the benthic infauna mixing the muddy sediment surface, known as the benthic boundary layer, can alter sediment acoustic properties [15]. Sediment erosion from extreme weather events can also alter sediment properties. In addition, if the sound speed of the bottom water rapidly changes, faster than the temperature or salinity change can equilibrate into the sediment beneath it, the sound speed ratio can change and significantly affect acoustic reflectivity [16, 17].

Since WW2, many sediment acoustic measurements have been performed both *in situ* and *ex situ*, using samples removed from the seabed [14, 18–21]. Acoustic properties of these various types of marine sediments were categorized based on the grain-size-distribution classifications of Folk and Ward [22]. These measurements, however, rarely reported wave speeds and attenuation at more than one frequency. In the post-cold-war era, strategic interests shifted to littoral regions with ocean bottoms exhibiting sandy sediment comprised of relatively well-sorted quartz grains. Since then, extensive work has been published on the acoustic properties of granular sediment, and a multitude of competing frequency-dependent physical models were created. Most of these models derive from Biot's theory for porous rock [23, 24] and

were later adapted to unconsolidated marine sediment [25–27], which describes the acoustic effects of the grain/pore water system. A characteristic frequency, determined by a balance between the pore size and the tortuosity of the sediment, separates two frequency regimes of behavior. At low frequencies, the viscous skin depth is larger than the pore size and the viscosity of the pore fluid dominates, resulting in small relative motion between the fluid and the grains. At high frequencies, the viscous length scales are small relative to the pore size and the tortuosity dominates, resulting in significant relative motion between the fluid and the grains. As the size of the grains become smaller, this characteristic frequency increases. At even higher frequencies, as the acoustic wavelength approaches the grain diameter, a dramatic reduction in sound speed and an increase in attenuation has been observed [28–30], which can be described by multiple scattering theory [29]. The Sediment Acoustics Experiment (SAX99) was conducted in 1999 to compare these sediment models with broad-band direct measurements and geoacoustic inversions of sound speed and attenuation of water-saturated sand [31]. Many of these inversion schemes, however, assumed the sediment behaved like a simple fluid, neglecting poroelastic physics. Even to date, much work in the field of underwater acoustics exploits the assumption that the sediment behaves like a fluid. While physical sediment acoustics models can now describe much of the physics associated with the acoustic dispersion observed in well-sorted sands, pure water-saturated sand is a small subset of all marine sediment found on the shelf. A physical sediment model describing the more complex interactions

as finer grains and organic matter are introduced does not exists.

Mud in the sediment acoustics community has been defined as a fine-grained sediment containing a mixture of silt and clay minerals with particle diameters less than 63 μm in accordance with previous classifications [10], and has largely neglected the effect organic matter (OM) has on bulk geoacoustic properties. When mud is absent of OM and surrounded by high electrolyte concentrations, the interactions among the platelets are dominated by electrostatic van der Waals forces that form complex and porous flocs suspending silt particles. Some modeling has been conducted to address this [32]. Organic matter has been shown to coat clay particles effectively reducing their charge potential and limiting their ability to aggregate [33]. Since small interstitial pores in mud serve as shields against microbial decomposition [34], there could be a preserved fibrous or viscous pore fluid that is neglected by existing sediment acoustics models. This sediment microfabric formed by complex organic-mineral structures have been directly observed and classified in the sedimentology literature via transmission electron micrograph [11], but demonstrating how the sediment fabric affects macroscopic acoustic properties is a topic of ongoing investigation.

1.3 Contributions to the field

As the understanding of acoustic propagation within this complicated waveguide progresses, the aforementioned assumptions and gaps in knowledge require more investigation. To this end, this monograph documents studies

of the following previously, largely neglected effects. 1) The effects of salinity variations of the bottom water on reflectivity from clay via laboratory measurements and modeling. 2) The effects of neglecting frequency-dependent poroelastic physics when inverting for the sound speed of sand-sized glass beads. 3) The effects of organic carbon on the acoustic properties of seagrass-bearing sediments. To conduct the study in 3), a new fully automated broadband core logger was constructed and verified, and is described here. These studies are more fully summarized below.

1.3.1 Effects of salinity variability on reflectivity from clay

Estuarine, riverine, and certain continental shelf environments experience significant variability due to dynamic oceanographic processes, which can cause substantial sound speed fluctuations in the water column as high as 50 m/s over time-scales on the order of a month [12, 13, 35]. In estuarine environments, bottom water salinity can fluctuate from 5 psu to 30 psu in 6 hours [36], while along the continental slope, salinity fluctuation is less extreme and over a longer time-scale [35]. Such variations can produce significant changes in how sound interacts with fine-grained sediments that have a sound speed ratio near unity and can therefore present challenges in applications including shallow water sonar and bottom surveys. To begin to understand these processes, laboratory measurements of the reflection coefficient in the frequency band near 1 MHz were obtained from a water-clay interface while varying the salinity of the bottom water. By modeling the reflectivity of the

clay during the molecular diffusion of salt, the diffusion coefficients were experimentally inferred and simulations at lower frequencies and longer time-scales were performed using the inferred diffusion coefficients. Derived characteristic length scales associated with the molecular diffusion of salt were compared with acoustic wavelengths to identify frequency regimes that are sensitive to salinity fluctuations. Results indicate that salinity fluctuations can cause measurable and significant effects in acoustic reflectivity at frequencies applicable to sonar.

1.3.2 Effects of neglecting poroelasticity

The sound speed of granular sediment has experimentally been shown to vary with frequency, yet in many instances in geoacoustic inversions, the sediment is modeled as a dispersionless fluid to minimize the number of unknowns and decrease the computation time. The effect to which assuming a frequency-independent fluid model with a constant bulk density can skew parameter estimation was investigated in a controlled laboratory layered waveguide. The waveguide consisted of a column comprised of 1-mm-diameter water-saturated glass beads that was suspended in a water-filled glass tube. The phase speed in the waveguide was measured from 1 kHz to 7 kHz and compared with the phase speed simulated in a finite element model of the experiment, where the water-saturated glass beads were modeled as either a fluid with constant bulk density and frequency-independent or frequency-dependent sound speed, or by an effective density fluid model (EDFM) that includes poroelastic physics. In-

ferred sound speed results using these fluid models were compared with direct sound speed measurements taken at different locations along the length of the column at a frequency range from 150 kHz to 450 kHz. Only results inferred using the EDFM agreed with direct measurements.

1.3.3 Broad-band Core and Resonance Logger (CARL)

Sediment core samples help scientists and engineers characterize various physical, biological, and chemical properties found *in situ*. By performing acoustic measurements on these well-characterized samples, more meaningful comparisons can be made among sediment properties. However, techniques to measure the acoustic properties of sediment core samples rarely report more than one frequency. In order to study the frequency dependence of marine sediment from minimally-disturbed *ex situ* core samples in the laboratory, the Core and Resonance Logger (CARL) was created to measure sound speed and attenuation at a broad frequency range. CARL combines the resonance technique [37, 38] with the pitch-catch pulse technique [39, 40], spanning a frequency range from 10 kHz to 7 MHz, and is made from off-the-shelf laboratory equipment. Verification measurements were performed with two oils each possessing a power-law-attenuation frequency dependence. One assumption made by the resonance technique assumes the sediment does not support shear motion. Finite-element modeling quantified the error associated with using the resonance technique on sediments with a finite shear modulus. This error can be ignored, particularly for fine-grained sediments with low shear

modulus values.

1.3.4 Effects of organic carbon on sediment properties

It is estimated that ten percent of all organic carbon absorbed by the ocean each year is stored in seagrass-bearing sediments [6]. However, current methods used to quantify organic carbon are time and labor-intensive as well as expensive, leading to large uncertainties in storage capabilities and difficulties in studying how these ecosystems respond to anthropogenic stressors [41]. Sediments with high organic carbon content have been correlated with highly-porous fine-grained sediments [42, 43]. Acoustic propagation is also sensitive to such sediment properties [9] and could be used to more rapidly quantify and monitor organic carbon stores, yet it has not, to the author's knowledge, been related to organic carbon content. To this end, sediment cores were collected during a field experiment in the seagrass meadows of the Lower Laguna Madre located in South Padre Island, Texas, USA. Sound speeds from 100 kHz to 300 kHz were measured radially as a function of depth within the cores. Cores were subsequently frozen, sliced along the same depth increments, and tested for organic carbon content and other sediment properties. Results demonstrated acoustic sensitivity to organic carbon, and a theory explaining this sensitivity is presented.

1.4 Organization of the dissertation

An outline of the remaining chapters in this document is presented. Chapters 2 and 3 consist of two stand-alone manuscripts submitted to the Journal of the Acoustical Society of America. A study of the effects of salinity fluctuations of the bottom water on the acoustic reflectivity from a clay-water interface is presented in Chapter 2. A study of the effects of neglecting poroelastic physics when inverting for sediment acoustic properties in a laboratory layered waveguide environment is presented in Chapter 3. In Chapter 4, CARL is described, which was then used during a field experiment presented in Chapter 5. Chapter 5 consists of a third stand-alone manuscript submitted to Geophysical Research Letters, which reports the relationship between the organic carbon content and acoustic properties in seagrass-bearing sediment. Conclusions are presented in Chapter 6, and appendices contain supporting information, including data processing algorithms, model descriptions, effects of CARL transducer loading, uncertainty calculations, accounting for bubbly sediment, and engineering drawings. Finally, a bibliography and vita are provided.

Chapter 2

Laboratory measurements and simulations of reflections from a water/clay interface during the diffusion of salt

2.1 Introduction

Certain continental shelf, estuarine, and riverine environments experience significant variability due to various oceanographic processes at a broad range of time-scales such as seasonal variability, tides, surface heating, currents, and salt wedges. These can cause substantial sound speed and density fluctuations in the water immediately above the seabed, also referred to as bottom water, which are often unknown to sonar operators. It is hypothesized that such variations in sound speed over the span of a season or tidal cycle can produce significant changes in how sound interacts with low-velocity fine-grained sediments, which can present challenges in applications including mine detection, port protection, shallow water sonar, and bottom surveys. This is attributed to the fact that the sound speed of fine-grained sediments is often near the sound speed of the water above it [44], where any small variation in the bottom water can cause an intromission angle to appear, disappear, or shift angle over short periods of time, drastically affecting the bottom loss and phase of reflected signals at frequencies in the sonar range. In addition, it is

typically assumed that the sound speed of the sediment's pore fluid is equal to that of the bottom water, such that the sound speed ratio, defined here as the sound speed of the sediment divided by its pore fluid, remains constant. In dynamic environments, this may not be a valid assumption.

Considered here are two mechanisms that can change the sound speed and density of the bottom water: a change in temperature or salinity. In the water column, convection can be the dominant factor contributing to salinity and heat transfer. However, diffusion can play a more important role in the sediment. Wood *et al.* demonstrated through numerical simulations that seasonal temperature changes of ± 4 °C can cause changes in seismic reflectivity particularly at high angles of incidence. However, even at a high angles of incidence, changes in the reflection coefficient were negligible above 600 Hz [16]. Although reflectivity variability due to seasonal temperature fluctuations have been well studied [16, 45, 46], reflectivity effects from shorter time-scale temperature fluctuations have received less attention.

Salinity fluctuations can also have an effect on the reflectivity of marine sediments and, to the author's knowledge, have not been addressed in the literature. This is potentially due to insufficient knowledge of the molecular diffusion coefficient of salt in marine sediments. In Sec. 2.2, two analytical salt diffusion models are derived: one simulating a salt wedge, where sediment is quickly exposed to bottom water of a different salinity than its pore fluid, and one simulating a longer-term seasonal variation modeled as a sinusoidal salinity variation. In Sec. 2.3, we report a high-frequency reflection coefficient

experiment conducted from two fresh-water saturated kaolinite clays at various times after exposure to water of different salinity. By calculating the salinity profile, the modeled reflection coefficient from clay was fit to the data to infer the molecular diffusion coefficient of salt through both clays. Using the experimentally inferred diffusion coefficients at atmospheric temperature and pressure (ATP), Sec. 2.4 presents simulated results of clay reflectivity under both cases derived in Sec. 2.2 within the operating frequency range of most sonar systems. Conclusions are discussed in Sec. 2.5.

2.2 Integrated diffusion/reflection model

The diffusion equation was solved analytically for two types of fluctuations commonly encountered in the ocean. Derivations are provided in the context of molecular salt diffusion for convenience, but can be mapped to heat conduction by replacing the salt concentration with temperature and the molecular diffusion coefficient of salt through the sediment with the thermal diffusivity of the sediment. Analytical solutions yield important insight into characteristic length and time scales of salinity fluctuations relevant to the associated variability in reflectivity investigated in this work.

2.2.1 The salt wedge

A salt wedge is a common phenomenon that occurs in the ocean, where heavier, more saline water travels near the water-sediment interface, quickly displacing the bottom water. This phenomenon can be represented by the dif-

fusion equation with the following 1-D diffusion equation and Dirichlet boundary conditions:

$$\begin{aligned} &\frac{\partial s}{\partial t} = D\frac{\partial^2 s}{\partial x^2}, \qquad x \geq 0, \quad t > 0, \\ &s(x,0) = s_{\mathrm{i}}, \\ &s(0,t) = s_{\mathrm{s}}, \end{aligned} \tag{2.1}$$

where s is the salt concentration, x is the distance from the boundary into the sediment, D is the diffusion coefficient, s_{i} is the initial salt concentration of the sediment, and s_{s} is the salt concentration held fixed at the sediment surface. To simplify the boundary and initial conditions, a change of variables is prescribed such that $\theta = (s - s_{\mathrm{i}})/(s_{\mathrm{s}} - s_{\mathrm{i}})$. Taking the Laplace transform, the partial differential equation simplifies into the following ordinary differential equation:

$$\begin{aligned} &\frac{\partial^2 \Theta}{\partial x^2} - \frac{p}{D}\Theta = 0, \qquad x \geq 0, \quad p > 0, \\ &\Theta(0) = \frac{1}{p}, \end{aligned} \tag{2.2}$$

where $\mathcal{L}\{\theta(x,t)\} = \Theta(x)$ and p is the Laplace variable. Applying the boundary condition and choosing the negative sign, Equation 2.2 has the solution

$$\Theta = \frac{1}{p}\exp\left(- x\sqrt{\frac{p}{D}}\right), \tag{2.3}$$

and the inverse Laplace transform is

$$\theta = \operatorname{erfc}\left(\frac{x}{\sqrt{4Dt}}\right). \tag{2.4}$$

Substituting $\theta = (s - s_\mathrm{i})/(s_\mathrm{s} - s_\mathrm{i})$ into Equation 2.4 and solving for s, the general solution of Equation 2.1 is

$$s(x,t) = (s_\mathrm{s} - s_\mathrm{i})\operatorname{erfc}\left(\frac{x}{\sqrt{4Dt}}\right) + s_\mathrm{i}, \qquad x \geq 0, \quad t > 0, \tag{2.5}$$

and is displayed in Figure 2.1a before and after the disturbance.

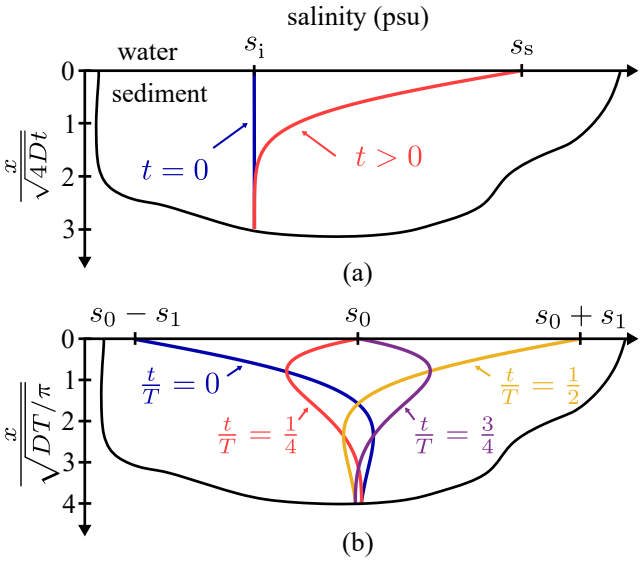

Figure 2.1: The salinity profile solutions in the sediment for (a) the salt wedge and (b) the sinusoidal forcing function. Depth into the sediment is normalized by the characteristic length scale associated with each solution.

2.2.2 Sinusoidal forcing function

For sinusoidally fluctuating bottom water salinity,

$$\frac{\partial s}{\partial t} = D\frac{\partial^2 s}{\partial x^2}, \qquad x \geq 0, \quad -\infty \leq t \leq \infty, \tag{2.6a}$$

$$s(0,t) = s_0 - s_1 \cos(\omega_{\mathrm{T}} t), \tag{2.6b}$$

$$q(\infty,t) = D\frac{\partial s}{\partial x}\bigg|_{x\to\infty} = 0, \tag{2.6c}$$

where s_0 is the mean bottom water salinity and s_1 is the amplitude of salinity variation. The angular frequency of the salinity variation is $\omega_{\mathrm{T}} = 2\pi/T$, where T is the period of oscillation. A zero substance flux q vanishes at $x = \infty$, far below the sediment surface. Superposition allows the salinity variable in Equations 2.6 to be separated into static and sinusoidal varying parts ϕ_0 and ϕ_1, where

$$\frac{\partial \phi_0}{\partial t} = D\frac{\partial^2 \phi_0}{\partial x^2}, \qquad x \geq 0, \quad -\infty \leq t \leq \infty, \tag{2.7a}$$

$$\phi_0(0,t) = s_0, \tag{2.7b}$$

$$\frac{\partial \phi_0(\infty,t)}{\partial x} = 0, \tag{2.7c}$$

which has the trivial solution of $\phi_0(x,t) = s_0$, and

$$\frac{\partial \phi_1}{\partial t} = D\frac{\partial^2 \phi_1}{\partial x^2}, \qquad x \geq 0, \quad -\infty \leq t \leq \infty, \tag{2.8a}$$

$$\phi_1(0,t) = \mathrm{Re}\{-s_1 e^{j\omega_\mathrm{T} t}\}, \tag{2.8b}$$

$$\frac{\partial \phi_1(\infty,t)}{\partial x} = 0, \tag{2.8c}$$

where the oscillatory term in Equation 2.6b is written as a complex exponential for convenience, and $s = \phi_0 + \phi_1$.

The variable, ϕ_1, is assumed to have the form

$$\phi_1(x,t) = \mathrm{Re}\{S(x)e^{j\omega_\mathrm{T} t}\}, \tag{2.9}$$

where $S(x)$ is a complex amplitude that varies with x. Inserting Equation 2.9 into Equation 2.8a, the ordinary differential equation is obtained

$$\mathrm{Re}\left\{S''(x) - \frac{j\omega_\mathrm{T}}{D}S(x)\right\} = 0, \tag{2.10}$$

which has the solution

$$S(x) = C_1 \mathrm{e}^{(1+j)x/L} + C_2 \mathrm{e}^{-(1+j)x/L}, \tag{2.11}$$

where C_1 and C_2 are constants, and the penetration depth, L, is defined as

$$L = \sqrt{\frac{DT}{\pi}}. \tag{2.12}$$

Substituting Equation 2.11 back into Equation 2.9, boundary conditions can be implemented to solve for the constants. Equation 2.8c ensures the

spatial gradient vanishes far below the sediment surface, forcing C_1 to zero. Solving for Equation 2.9 at the interface and equating it to Equation 2.8b, $C_2 = -s_1$. Grouping complex exponentials, evaluating the real part, and combining ϕ_0 and ϕ_1, the final solution can be reduced to

$$s(x,t) = s_0 - s_1 e^{-x/L} \cos\left(\omega_T t - x/L\right), \tag{2.13}$$

which contains an exponential decay term and an oscillatory term with a phase lag linearly dependent on distance below the sediment surface. The final solution is displayed in Figure 2.1b at time increments of $T/4$.

2.2.3 Reflection coefficient model

Once an analytical expression is obtained for the salinity profile in the sediment, the reflection coefficient is computed by first discretizing the profile into thin fluid layers twenty times smaller than an acoustic wavelength. At each layer, the structure of the sediment is assumed constant with depth and unaltered during the diffusion, i.e. the porosity and sound speed ratio are held constant. However, the density and sound speed of the pore fluid can vary with salinity. Under these assumptions, the specific acoustic impedance Z is calculated at each layer and the n-layer reflection coefficient is then calculated using the input impedance method outlined by Brekhovskikh [47]. Impedance at each layer is found using the expression

$$Z(x,t) = \frac{\omega \rho(x,t)}{k(x,t)}, \tag{2.14}$$

where ω is the angular frequency of the acoustic wave, ρ is the density of the sediment, and k is the complex wavenumber in the sediment. Sediment density can vary with depth and time governed by the relation

$$\rho(x,t) = (1-\beta)\rho_{\mathrm{m}} + \beta\rho_{\mathrm{pf}}(x,t), \tag{2.15}$$

where β is porosity, ρ_{m} is the density of the mineral grain and ρ_{pf} is the density of the pore fluid [9]. Seawater density is a function of salinity, temperature, and pressure and was solved for using the UNESCO equation of state [48]. The wave number is also depth and time dependent and is calculated using the expression

$$k(x,t) = \frac{\omega}{\mathrm{SSR} \times c_{\mathrm{pf}}(x,t)} - j\alpha, \tag{2.16}$$

where SSR is the sound speed ratio and α is the attenuation in Np/m, which are both assumed constant. The sound speed of the pore fluid, c_{pf}, is salinity, temperature, and depth dependent calculated using Equation 7 in Coppens [49].

2.3 Experiment

A high-frequency laboratory experiment was performed to determine the diffusion coefficients in reconstituted model sediments composed of two kaolinite clays. The two types correspond to card house and card pack microstructures [50]. High frequencies were used in order to acoustically capture the small length scales associated with diffusion over a short period of time. Using the theory derived in Sec. 2.2, the molecular diffusion coefficient of salt at ATP was inferred from the experiment.

2.3.1 Kaolinite samples

Two types of kaolinite-based clays obtained from Imerys Performance Minerals were prepared in the laboratory: Hydrite RS-A and Hydrite Flat DS. In 2016, Ballard and Lee characterized the same types of clay and reported that the RS-A was a more porous clay with a fluid-like consistency suggestive of a card-house flocculation, while the Flat DS was less porous with a slightly higher shear modulus suggestive of a card-packed flocculation [50]. Both minerals were similar in composition and thickness, however the RS-A platelets were about an order of magnitude shorter than the Flat DS platelets [50]. The samples were prepared by mixing the dry kaolinite powder with distilled water until homogeneous. The mixture was poured into a two-part polycarbonate container held together and sealed with butyl putty, shown in Figure 2.2. The bottom section of the container served as the sample holder, while the top section, the tower, allowed for clay to fill the container past the top of the sample holder. The samples were placed in a vacuum chamber at 9.1 kPa and vibrated by an eccentric mass shaker for 24 hours to remove any air bubbles entrained by the mixing process. The extra layer of clay above the sample holder insured that the air-water interface of the settled sample remained much higher than the top of the sample holder and allowed for the clay in the sample to settle faster. Guided by slots in the sample holder, a thin polycarbonate divider was inserted through the butyl putty, bisecting the clay, and trapping the sample beneath it. This method of sample preparation minimized the introduction of air into the sample and achieved a repeatably smooth and flat interface

suitable for ultrasonic reflection measurements.

The tower and excess clay were removed and the sample's mass and volume was measured to calculate the average density of the clay. The porosity was calculated by rearranging Equation 2.15 into

$$\beta = \frac{1 - \rho/\rho_{\mathrm{m}}}{1 - \rho_{\mathrm{pf}}/\rho_{\mathrm{m}}}, \tag{2.17}$$

where ρ_{m} is the known particle density of the kaolinite mineral. The density and porosity were assumed constant with sample depth.

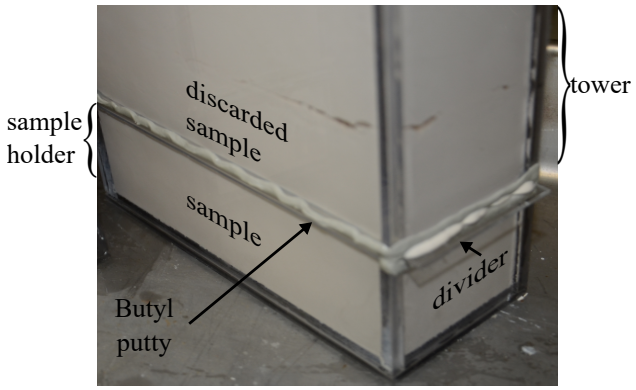

Figure 2.2: The sample preparation container consisted of a tower mated with the sample holder and sealed with butyl putty (gray). The divider bisected the sample preserving the water-clay interface.

2.3.2 Description of the experiment

The reflectivity of both types of clays were assessed by measuring the reflection coefficient as a function of angle. The reflection coefficient apparatus (Figure 2.3a) consisted of a stepper motor that turned a lead screw, which translated a follower. The translation of this follower precisely altered the angle

between two 1.27-cm diameter 1 MHz transducers whose beams intersected at a point elevated 5.08 cm from the base plate (Figure 2.3b). The water/clay interface of the sample was designed to intersect this point to within a 0.0127 cm tolerance. A pulser-receiver was operated in through-transmission mode, such that the reflected pulse was digitized by the oscilloscope and acquired by the computer.

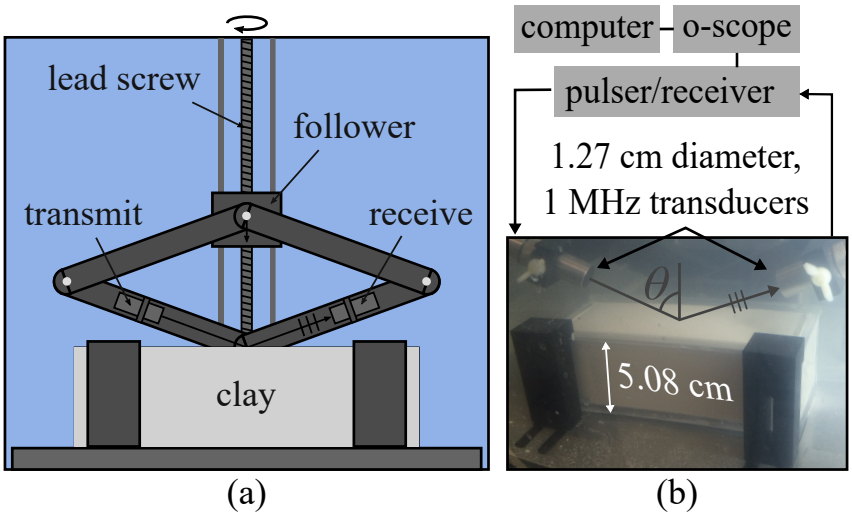

Figure 2.3: (a) Schematic of the reflection apparatus with the clay sample in place. (b) Photograph of the transducers forming an angle of incidence θ with respect to the normal of the clay-water interface. The clay-water interface was located 5.08 ± 0.0127 cm above the base plate.

Before placing the sample in the apparatus, the incident (non-reflected) pulse was measured by aligning the transducers 180 degrees from each other and acquiring the transmitted pulse through the water. Next, the sample was installed in the apparatus, the divider was carefully removed exposing the clay to the surrounding water, and reflected pulses were then acquired as a function

of angle. The reflection coefficient at each angle was calculated by taking the ratio of the Fourier transform of the reflected pulse to the Fourier transform of the incident pulse. The same apparatus and methodology described in Sagers *et al.* [51] was used in this work.

The experiment consisted of three cases. Case 1 was a baseline reflection measurement of RS-A and Flat DS under fresh water. In Case 2, the apparatus and sample were transferred to a 3.6% salinity bath. Reflection coefficient measurements were made every 2–3 minutes until the bottom loss curve converged to a steady state. In Case 3, after having exposed the sample to salt water for 2 hours, the apparatus and sample were transferred back to the fresh water bath and measurements were taken every 2–3 minutes until convergence was achieved. Note that an incident pulse was acquired in each bath prior to inserting the sample into the apparatus and exposing it to the bottom water. The divider was carefully and slowly replaced over the sample while underwater, before transferring the sample in and out of each bath, to preserve the interface and minimize air contamination. Prior to conducting the reflection coefficient measurements presented in Sec. 2.3.3, several tests were run in fresh water to assure the reflection from the sample was not changing due to uncontrolled phenomena, such as continued settlement of the sample, sample alteration due to reinserting the divider, or transferring the sample in and out of the bath. In addition, the sample, fresh and salt water baths were all maintained at room temperature to minimize any heat transfer during the experiment.

2.3.3 Results

Case 1 was used to characterize the acoustic properties of the clay samples before the salinity of the bottom water was varied. Figure 2.4 plots bottom loss (BL), defined as $\mathrm{BL} = -20\log_{10}(|\mathrm{R}|)$, and phase ($\angle$R), where R is the complex-valued reflection coefficient, versus angle of incidence, for RS-A at 1 MHz and Flat DS at 1.5 MHz. The reason why the reflection coefficients were measured at different frequencies for each clay type is discussed in Section 2.3.4. A lossy fluid-fluid plane-wave reflection coefficient model was fit to the measurement to obtain the inferred sound speed ratio and attenuation, and the results are tabulated in Table 2.1.

Table 2.1: Acoustic properties of RS-A and Flat DS at 1 MHz and 1.5 MHz, respectively.

property	symbol	RS-A	Flat DS
mineral density[T]	ρ_{m} (kg/m^3)	2580	2580
density[M]	ρ (kg/m^3)	1328	1554
porosity[M]	β	0.79	0.65
sound speed ratio[I]	SSR	0.965	0.991
attenuation[I]	α (dB/λ)	0.19	0.54

[T] Tabulated from manufacturer.
[M] Measured properties.
[I] Inferred properties from Case 1.

Both fresh-water-saturated clays showed good agreement with the reflection coefficient model and possessed angles of intromission at different angles of incidence. A model of a finite-beam reflection from a fluid-fluid interface [52] with parameters from Table 2.1 yielded bottom loss and phase curves which were indistinguishable from those calculated from the plane-wave

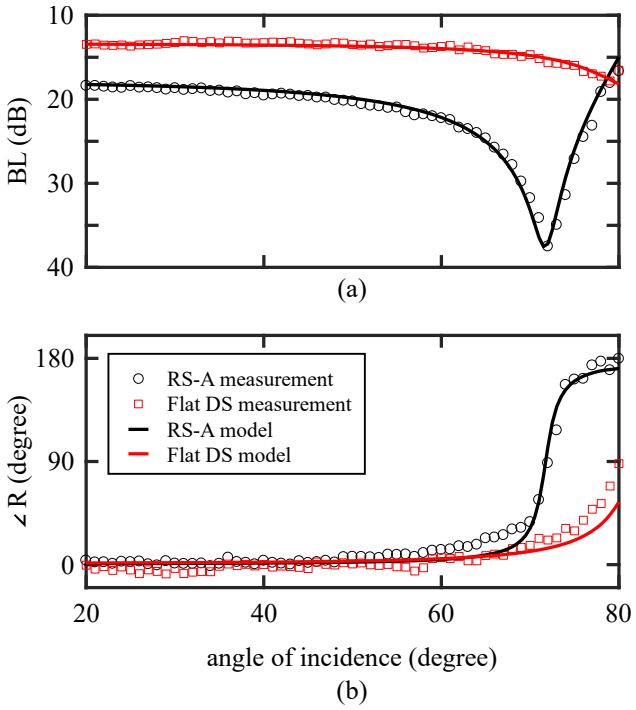

Figure 2.4: Measurements and best-fit models of (a) bottom loss (BL) and (b) phase (∠R) as a function of angle of incidence for RS-A (black) and Flat DS (red), under fresh water.

model, suggesting minimal contributions from the finite-beam. The inferred sound speed ratio of the RS-A and Flat DS kaolinite clays are 0.965 and 0.991, respectively.

Figure 2.5 displays bottom loss of Flat DS taken from Cases 1–3 denoted as fresh, salt, and fresh after salt, respectively. Even though Cases 1–3 represented bottom water fluctuations that perturb its density and sound speed by less than 3%, these fluctuations can lead to drastic changes in bottom loss at high angles of incidence. RS-A bottom loss varied up to 15 dB

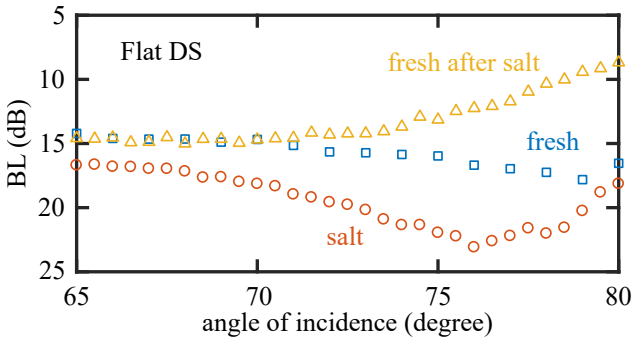

Figure 2.5: Bottom loss (BL) as a function of angle angle of incidence from Flat DS over fresh water (blue squares), immediately after exposing to salt water (red circles), and over fresh water again (yellow triangles) after exposing Flat DS to salt water for 30 minutes.

at high incident angles due to associated shifts in its intromission angle. Special attention, however, is brought to Flat DS. Flat DS under fresh water can contain either an angle of intromission when saturated with fresh water or a critical angle after being exposed to salt water for two hours, demonstrating that salt has altered its acoustic properties. This plot corresponds to the first measurement taken after the samples were exposed to the bottom water. Since it took a finite amount of time to begin the reflection coefficient measurement after exposing the bottom water to the clay, the salt had already begun to diffuse in or out of the sample, leading to a deviation in predicted bottom loss curves immediately after exposure.

2.3.4 Diffusion coefficient inference

In order to infer the molecular diffusion coefficient of salt in the two clays, the reflection coefficient model assuming a salinity profile dictated by

Equation 2.5 was fit to the data from Case 2 as a function of time. For the case of a salt wedge in the ocean, where convection is a dominant mode of salinity transport in the water halfspace, the surface salinity, s_{s}, can be assumed to equal the salinity of the salt wedge. However due to the static nature of the laboratory experiment, convection is minimized, and the 1-D diffusion problem must be solved in both the bottom water and clay half spaces with different diffusion coefficients and initial salt concentrations. At time $t = 0$, the two half spaces come into contact, represented mathematically by imposing an equal substance flux at the water-clay interface. A similar approach is found elsewhere [53] with regards to heat transfer via conduction. Rather than assuming the surface salinity of the clay is equal to the saline bath in Case 2, the two fluxes are equated and the surface salinity is solved for in the following manner:

$$\begin{aligned} q_{\mathrm{c}}\Big|_{x=0} &= -\, q_{\mathrm{w}}\Big|_{x=0}, \\ s_{\mathrm{s}} &= \frac{s_{\mathrm{i,w}}\sqrt{D_{\mathrm{w}}} + s_{\mathrm{i,c}}\sqrt{D_{\mathrm{c}}}}{\sqrt{D_{\mathrm{w}}} + \sqrt{D_{\mathrm{c}}}}, \end{aligned} \tag{2.18}$$

where $s_{\mathrm{i,w}}$ and $s_{\mathrm{i,c}}$ are the initial salt concentrations in the water and clay, respectively. D_{w} is the molecular diffusion coefficient of salt in water equal to 1.6×10^{-9} m^2/s [54], and D_{c} is the unknown effective diffusion coefficient in the clay. In the experiment the initial salt concentration in the clay is zero and the negative sign insures the direction of the diffusion flux remains constant across the boundary. Substituting Equation 2.18 into Equation 2.5 and setting

s_i to zero yields the salinity profile in the clay as a function of time

$$s(x,t) = s_{\mathrm{i,w}}\left(\frac{\sqrt{D_\mathrm{w}}}{\sqrt{D_\mathrm{w}}+\sqrt{D_\mathrm{c}}}\right)\mathrm{erfc}\left(\frac{x}{\sqrt{4D_\mathrm{c}t}}\right). \tag{2.19}$$

The effective diffusion coefficient of the clay will serve as the fitting parameter. The diffusion coefficient of salt in water is assumed to be significantly higher than in clay. This causes the salinity at the surface to approach that of the water and gives the salinity profile in the water a more gradual slope. Since, at high incident angles, the transducers are fairly close to the surface of the clay, the salinity profile in the water was approximated as a constant equal to the surface salinity. The diffusion coefficient in the clay is also assumed to be constant as a function of depth, time, and salinity. The bottom loss was then evaluated using the relations in Sec. 2.2.3 with properties in Table 2.1.

Figures 2.6a–b show measured bottom loss of RS-A and Flat DS at 1 MHz and 1.5 MHz, respectively, as a function of angle at various times after the salt water is exposed to the clays (colored symbols). The solid lines are best-fit bottom loss model curves evaluated at and colored to correspond with the same times as the experiment. Inferred effective diffusion coefficients for RS-A and Flat DS were $5 \times 10^{-10}\mathrm{m}^2/\mathrm{s}$ and $7 \times 10^{-11}\mathrm{m}^2/\mathrm{s}$, respectively. Model fits were performed by minimizing the sum of the least squared error between measurement and model. Since diffusion coefficients differed by an order of magnitude, analysis was performed for Flat DS at 1.5 MHz to capture reflectivity variations of comparable order to variations observed with RS-A. The model provides good agreement with the data for both clays and

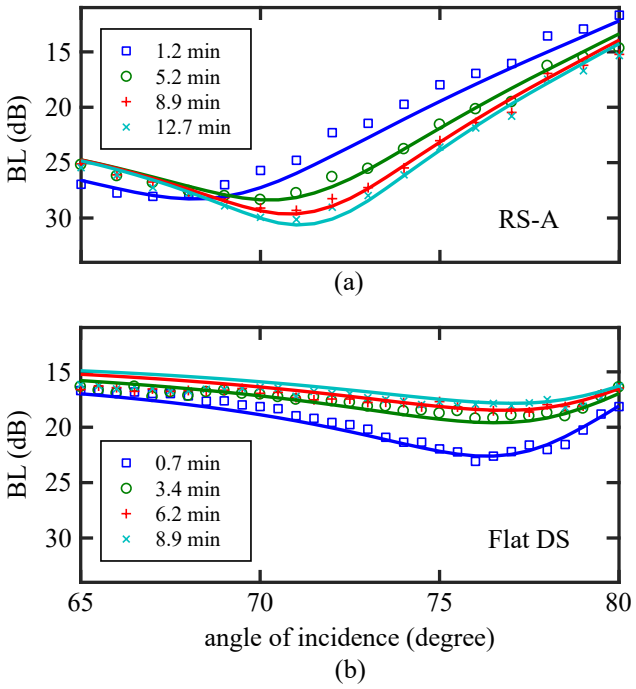

Figure 2.6: Bottom loss (BL) as a function of angle of incidence for (a) RS-A and (b) Flat DS during the molecular diffusion of salt. Symbols represent measured bottom loss and the solid lines with corresponding color represent the best-fit modeled bottom loss. This fitting process was used to infer the diffusion coefficient of salt in both clays.

tracks the intromission angle well. This serves as supporting evidence that the reflectivity change seen in the experiment is due to molecular diffusion of salt into the clays. Also in a controlled and static environment, the reflectivity appears insensitive to any potential change in microstructure caused by a change in salinity affecting parameters such as porosity, sound speed ratio, and attenuation, which were held fixed in the model.

Interestingly, while both clays were composed from the same kaolinite mineral [50], their diffusion coefficients differed by more than an order of mag-

nitude. A relation for diffusion coefficient of sediments currently exists in the literature [55] and is

$$D_{\mathrm{c}} = D_{\mathrm{w}} \frac{\beta \delta}{\tau}, \tag{2.20}$$

where τ is tortuosity and δ is constrictivity. Constrictivity is a parameter bounded by zero and one, where zero represents closed pores and one is a material with open pores much larger than the diffusing substance [55]. Assuming a tortuosity of 1.25, deemed appropriate by Stoll for fine-grained sediment [56], yields constrictivity values of 0.49 and 0.08 for RS-A and Flat DS, respectively. Ballard and Lee findings [50], identifying RS-A as a card-house and Flat DS as card-packed flocculation, could provide insight as to why these clays have such different diffusion coefficients. A card-house flocculation could provide a less constrictive path for salt molecules to travel in and out of the clay. More investigation is warranted to support this claim and to further understand how and which measurable sediment properties affect the diffusion coefficient.

2.4 Simulations

Using the diffusion coefficients inferred in Sec. 2.3.4, the modeled reflectivity after a salt wedge or during a seasonal sinusoidal fluctuation outlined in Sec. 2.2 are applied to lower frequencies and longer time scales more applicable to the sonar application. The magnitude in salinity fluctuations is maintained between 0 psu and 36 psu to emphasize the effect in reflectivity, however such drastic salinity fluctuation can be observed during a tidal cycle or salt wedge in estuarine or riverine environments [36].

2.4.1 Salt wedge

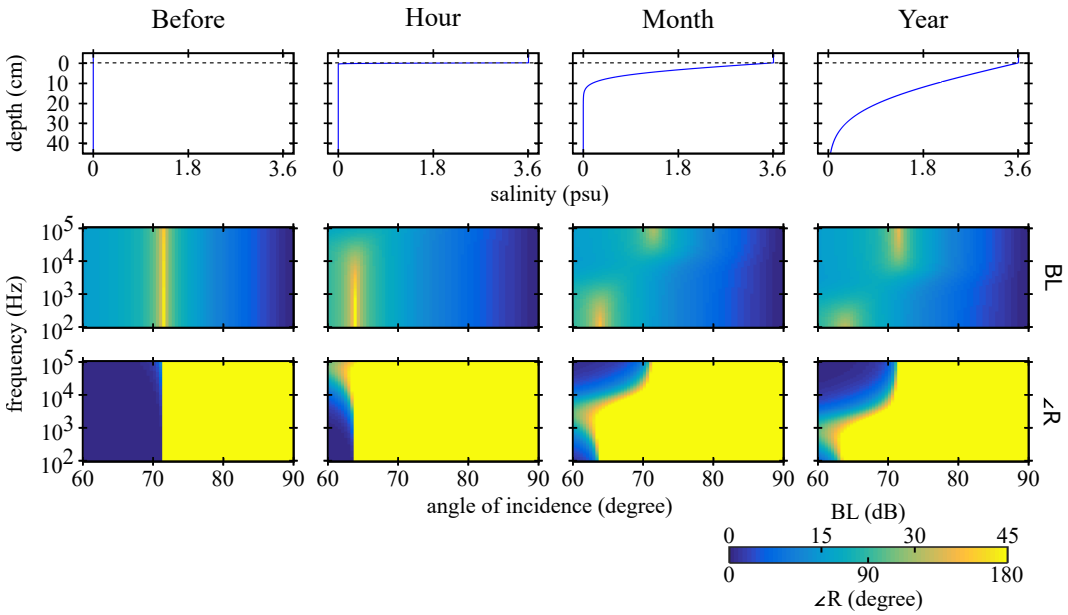

Figure 2.7: Simulations of the salt wedge passing over and diffusing into RS-A are shown. Salinity profiles as shown with the corresponding bottom loss (BL) and phase (∠R) in color as function of frequency and angle of incidence.

The first, second, and third row of plots in Figure 2.7 simulate the salinity profiles, bottom loss, and phase, respectively, before and at various times after a salt wedge passes over a fresh-water-saturated RS-A clay. Bottom loss and phase are shown in color and are plotted as functions of frequency and angle of incidence. The clays were assumed non-dispersive at lower frequencies and the attenuation was linearly extrapolated from Viscous Grain Shearing fits plotted in Figure 5 in Ballard and Lee [50].

Before the salt wedge, the bottom loss and phase are frequency independent, aside for the power law attenuation. Within the first hour after

exposing the clay to salt water, the intromission angle shifted down by almost 10 degrees. On the time-scale of minutes, hours, or even days after a salt wedge occurs, drastic changes in reflectivity can occur in the sonar frequency range. If diffusion in the clay continues for months or years, the shifted angle of intromission disappears and original angle of intromission begins to appear at higher frequencies. Between these angles of intromission, there is a frequency band that spans a couple of orders of magnitude that exhibits a weak intromission angle. More importantly in this regime, the reflected pulse can be phase inverted depending on the transmitted frequency. Also, as this transition region moves down in frequency with time, a pulse transmitted at a single frequency could phase invert within a matter of days or weeks, depending on the transmitting frequency and diffusion coefficient.

2.4.2 Seasonal/tidal variability

When the bottom water salinity fluctuates seasonally, the associated salinity profile, bottom loss, and phase are shown in Figure 2.8 for both RS-A and Flat DS. Note that for RS-A, seasonal changes in salinity can affect reflectivity below 20 kHz. The simulated salinity profiles in Flat DS are shown to affect the entire sonar frequency band. Seasonal fluctuations can also cause Flat DS to exhibit either a critical angle of an angle of intromission, depending on if it is spring or fall, respectively. For Flat DS, reflections in the spring also can exhibit complex phasing depending on the operating frequency. For example, at a high angle of incidence above 100 kHz, the reflected signal

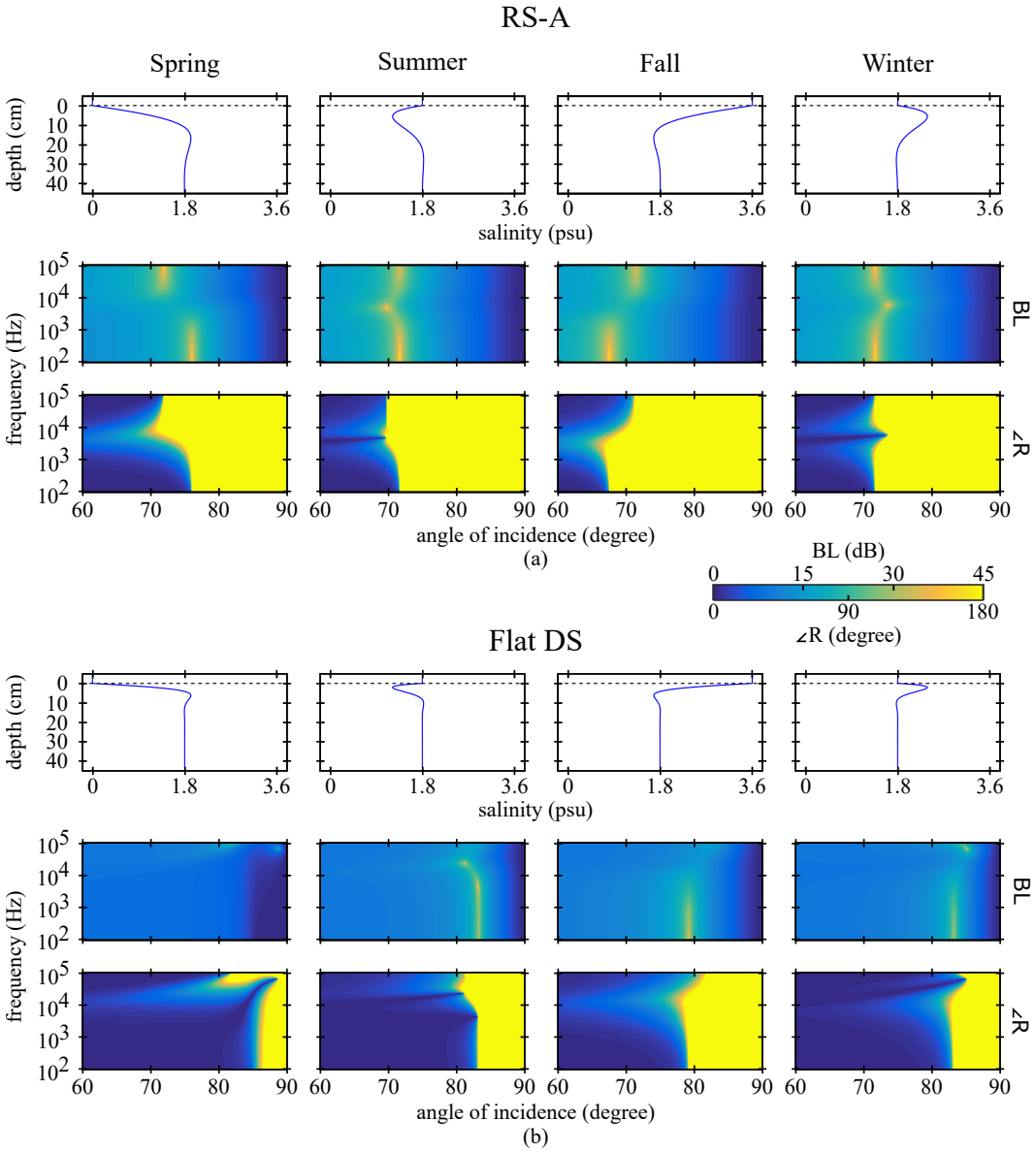

Figure 2.8: Simulations of the salinity profiles in RS-A (a) and Flat DS (b) from a seasonal sinusoidal salinity forcing condition at the sediment surface are shown. Bottom loss (BL) and phase ($\angle$R) from RS-A and Flat DS are plotted in color as a function of frequency and angle of incidence.

is phase inverted, characteristic of a soft bottom, while below 10 kHz, the phase of the reflected signal is preserved, characteristic of a hard reflector. While such extreme salinity fluctuation may not be realistic seasonally, the time-scale and salinity fluctuation were chosen to facilitate interpretation of the variability in reflectivity. Extending Figure 2.8 to a tidal cycle, where such drastic salinity fluctuations have been observed [36], the characteristic frequency increases by nearly a factor of 30 where any acoustic signal below 500 kHz is affected by the bottom water fluctuation. These phenomena could have profound effects in long-range shallow water sound propagation, where many of the bottom interactions occur at high angles of incidence. Long-range propagation studies investigating variability in received signals due to salinity fluctuations, however, are left to future works.

2.4.3 Discussion

The benefit to deriving the salinity profiles analytically and experimentally inferring salinity diffusion coefficients is that it provides insight as a closed form expression for the characteristic lengths relevant to acoustic reflection. For a salt wedge, if the characteristic length of the salinity gradient defined from Equation 2.5 as $\sqrt{4D_{\mathrm{c}}t}$ is smaller than an acoustic wavelength in the clay, the salt wedge could result in significant changes in reflectivity. Similarly for a sinusoidal bottom water fluctuation, the exponential decay term in Equation 2.13 contains a characteristic length that is proportional to the square root of the diffusion coefficient and period of oscillation described by

Equation 2.12. To first order, this characteristic length could also be compared with an acoustic wavelength in the clay to determine which operating frequency range would be affected by such a bottom water fluctuation. If the operating frequency is high enough, such that $\lambda < L$, the reflected wave only senses the sediment near the surface, where the pore fluid is equal to the bottom water. However at a lower frequency, where $\lambda > L$, the reflected wave is insensitive to the thin sediment layer attributed to the diffusion process, and the pore fluid should not be assumed equal to that of the bottom water. Although when the sound speed ratio is close to unity and the wavelengths are of comparable order to the length scales, reflectivity can become quite complex.

A more practical comparison can be performed between the operating frequency and period of variability. Figure 2.9 displays two black diagonal lines that separate three regions of interest for the Flat DS clay, where reflectivity is either insensitive to temperature and salinity bottom water variability (green), sensitive to salinity bottom water variability only (yellow), or sensitive to both temperature and salinity bottom water variability (red). The line that separates the green and yellow regions represents where the acoustic wavelength in the clay is equal to the penetration depth of salinity diffusion inferred in this work, while the line that separates the yellow and red regions represents where the acoustic wavelength in the clay is equal to the penetration depth of heat conduction investigated in Reference 16. A thermal diffusivity value equal to 3×10^{-6} m/s was used in Figure 2.9, which is consistent with tabulated values for a sediment of comparable porosity [16]. While the regions

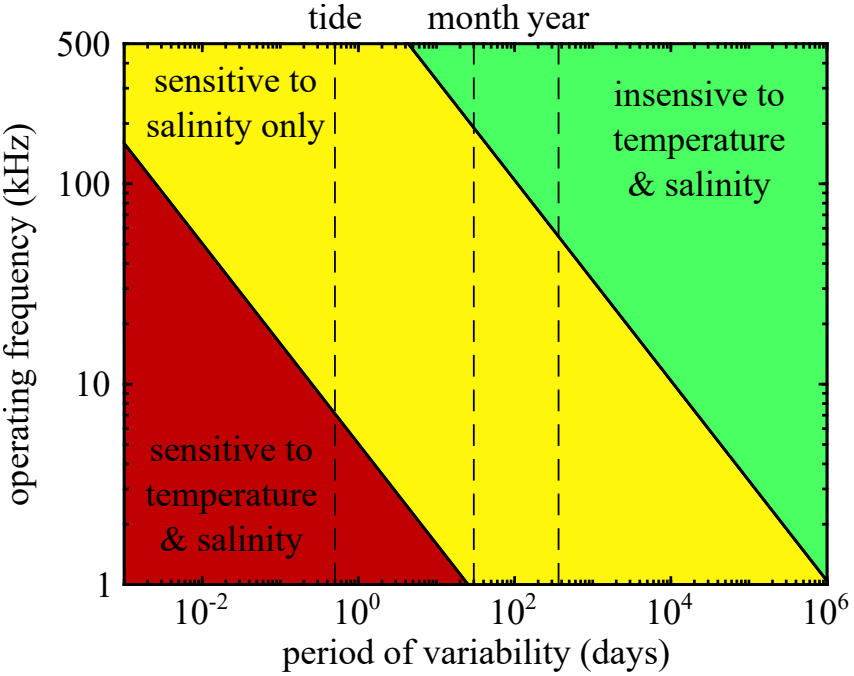

Figure 2.9: For a Flat DS clay, operating frequency and period of variability regions sensitive to salinity (yellow) and both temperature and salinity (red) bottom water variability are shown. Also, a region where reflectivity is insensitive to bottom water variability (green) is shown. Periods of variability typically encountered in the ocean are displayed with vertical dashed lines for reference.

shown in Figure 2.9 are subject to shift depending on the coefficient of thermal diffusivity and salinity diffusion of natural sediments, the representation effectively couples acoustic reflectivity from the sediment with the physical oceanography above the sediment. In other words, for a given location with high levels of bottom water variability, this representation allows the operator to easily determine which frequencies are affected or unaffected.

Simulations presented in Figures 2.7 and 2.8 represent idealized condi-

tions at ATP. The effect of changing the temperature and pressure at depth could affect the diffusion coefficient of the pore fluid, D_{w}, from Equation 2.20 and is expected to change proportionally to the pore fluid density ρ_{pf} such that

$$\frac{D_{\mathrm{w}'}}{D_{\mathrm{w}}} = \frac{\rho_{\mathrm{pf}}}{\rho_{\mathrm{pf}'}}, \tag{2.21}$$

where the prime signifies the fluid at the ocean bottom [57]. According to Equation 2.21, the increase in fluid density at depth would, therefore, decrease the diffusion coefficient of the pore fluid. However, the change in density between water at ATP and water at a temperature of 4 °C and a depth of 100 m would reduce the diffusion coefficient of water by less than 0.1%.

Compaction (dewatering) may be a more confounding effect that has been demonstrated to alter the microstructure in naturally consolidated marine clays [58], as well as laboratory bentonite and kaolinite clays [59] by reorienting the clay platelets producing long narrow voids. Such a card-packed orientation could significantly decrease the porosity, permeability [60], and, similarly, the constrictivity parameter in Equation 2.20, as a function of depth. The simulations performed here, however, assumed the microstructure did not change properties as a function of depth, and while this assumption may be reasonable for the high-frequency experiment discussed in Sec. 2.3, at lower frequencies and longer diffusion lengths, this effect should be taken into account.

2.5 Conclusion

Results indicate greater attention should be granted to pore water temperature and salinity diffusion, for a more accurate determination of reflectivity from fine-grained sediments in environments with significant bottom water temperature and salinity fluctuations. The diffusion equation was solved for fixed and sinusoidally varying salinity boundary conditions emulating a salt wedge and seasonal variability, respectively, and characteristic lengths were derived. The variation in acoustic reflectivity from two kaolinite clays due to bottom water salinity variability was investigated experimentally in the laboratory at high frequencies and simulated at frequencies relevant to many sonars. This work was performed to isolate and quantify changes in reflectivity caused by molecular diffusion of salt into clay, a major constituent in fine-grained sediments.

Experiments and models showed bottom water variability over sediment with a sound speed ratio near unity caused the sediment to appear acoustically soft or hard at high incident angles, depending upon the operating frequency, the diffusion coefficient of the sediment, and the time-scales after the fluctuation. The molecular diffusion coefficient of salt in RS-A and Flat DS kaolinite clays were experimentally inferred to be 5×10^{-10} and $7 \times 10^{-11} \mathrm{m}^2/\mathrm{s}$, respectively, which are several orders of magnitude slower than the thermal diffusivity used in Wood *et al.* [16]. While Wood *et al.* reported seasonal temperature variability to affect reflectivity below 600 Hz due to temperature gradients with long characteristic lengths, the slower molecular diffusion co-

efficient of salt in clay decreases the characteristic diffusion lengths, and thus affects reflectivity at shorter wavelengths and higher frequencies. Generally in an environment where the temperature and salinity of the bottom water is highly variable, if the acoustic wavelength is larger than the characteristic length-scale of the diffusion or conduction, the temperature or salinity of the bottom water should not be assumed equal that that of the pore fluid. However, at high frequencies, where the acoustic wavelength is smaller than the characteristic length-scale of the diffusion or conduction, the temperature or salinity of the bottom water can be assumed equal to that of the pore fluid. For rapid diurnal fluctuations observed in riverine and estuarine environments within the sonar operating frequency, it is recommended that the salinity of the pore fluid should be assumed equal to the time-averaged salinity of the bottom water, rather than the instantaneous salinity of the bottom water. Characteristic length scales derived in Sec. 2.2 and Figure 2.9 can also provide insight into how temperature fluctuations over shorter time-scales can affect reflectivity. For example, decreasing the period of oscillation from a year to a tidal cycle for Flat DS could increase the characteristic frequency to about 7 kHz, which is within the operating frequency range for many active sonar systems.

Unlike the controlled conditions achieved in the laboratory, there are several other factors that could accelerate the mass transfer of salt and heat transfer into or out of the top layer of sediment in the ocean, such as hydrodynamic convection or bioturbation. More investigation with different clay

minerals, such as smectite or illite, as well as the effect temperature and pressure at depth have on diffusion is warranted to better understand the molecular salt diffusion in marine clays.

The idealized clay measured in the present work and many natural fine-grained sediments found in the deep ocean have such low shear speeds and high shear attenuation [50], they can be approximated as a fluid. However, as the grains become more coarse, the validity of the simple fluid approximation is questioned in Chapter 3.

Chapter 3

An illustration of the effect of neglecting poroelastic physics of water-saturated glass beads in a laboratory waveguide inference process

3.1 Introduction

Sound propagation in a shallow water waveguide, such as on the continental shelf, is dependent upon the acoustic properties of the boundary conditions. Extensive work has been published on the acoustic properties of granular sediment creating a multitude of competing predictive models. Experiments such as the Sediment Acoustics Experiment 1999 and 2004 (SAX99 and SAX04, respectively) have been conducted to attempt to validate sediment models with inversions and direct measurement [31, 61].

Geoacoustic inversion is an attractive and useful tool to characterize large quantities of the ocean bottom without the need for labor intensive and invasive coring operations. In many instances involving geoacoustic inversions, it is advantageous to obtain a well characterized model of the waveguide, with well constrained inputs such as the sound speed profile in the water column, sea state, bathymetry, or number of sediment layers to minimize the number of unknowns and yield a more accurate estimate of geoacoustic properties

of the seabed. Due to the often large number of unknown variables, it is tempting to minimize the number of sediment acoustic properties for which to invert, by assuming the sediment behaves like a lossy fluid with a frequency-independent bulk density and sound speed, despite the fact that dispersion and shear waves have been repeatedly observed in granular sediments. In addition, these assumptions neglect the dynamics of the grain-pore water system [25,27] and may poorly predict the sediment sound speed [19, 62]. Figures 4 and 5 in Reference 26 reported theoretical reflection and transmission curves modeling the sediment as a simple fluid with constant bulk density or a fluid with an effective density taking poroelastic effects into account. It was determined that differences between the two cases were largest at normal incidence and increased with frequency [26], though an experiment demonstrating this effect was not reported.

The aim of this paper is to experimentally demonstrate and quantify the effect of neglecting poroelastic physics in water-saturated glass beads (WSGB), during a mid-frequency sound speed inference process, within a laboratory layered waveguide, while modeling the WSGB as an effective fluid with various physical behaviors. In addition, high-frequency direct sound speed measurements were conducted and compared with the inference results. It was found that self-consistency between the measurements, the inference results, and the sediment model predictions was only achieved when accounting for poroelastic physics that resulted in dispersion due to a reduction in effective density. Section 3.2 introduces the fluid sediment acoustics models used to describe the

WSGB in the inference process. Section 3.3 describes the laboratory measurements performed. Next, Section 3.4 describes the finite element model (FEM) simulation of the layered waveguide used in the inference process, and includes a validation of the simulation. Subsequently, Section 3.5 compares the inferred sediment sound speeds to direct measurements, and concluding remarks are made in Section 3.6.

3.2 Fluid sediment models

Marine granular sediments are known to have a shear modulus several orders of magnitude smaller than their bulk modulus and are often approximated as a fluid. Fluid models are advantageous due to their simplicity and are more easily integrated into geoacoustic inversions of sediment containing stratification and complicated bathymetry. The simplest model uses a purely real, frequency-independent density and will be referred to as the constant density fluid model (CDFM). Poroelastic effects were accounted for using an effective density fluid model (EDFM), in which the density is complex and frequency-dependent. More complex sediment models are beyond the scope of the present paper.

3.2.1 Constant density fluid models

In the CDFM, the density of the sediment is determined by a mixture law

$$\rho = (1 - \beta)\rho_{\mathrm{g}} + \beta\rho_{\mathrm{w}}, \tag{3.1}$$

where β is the porosity of the sediment, and ρ_{g} and ρ_{w} are the grain and pore water density, respectively. Bulk density is calculated either by dividing the sediment wet weight by the volume it occupies or, using Equation 3.1, with $\beta = 1 - m_{\mathrm{dry}}/\rho_{\mathrm{g}}V$, assuming the grain density, pore water density, volume (V), and dry mass (m_{dry}) are well known.

To account for the experimental observations of dispersion in granular sediments [31,38,63–65], a frequency-dependent fluid model (FDFM) is sometimes used, with a constant, frequency-independent density equal to the bulk density, and with a frequency dependent sound speed, which also implies a frequency-dependent bulk modulus [66,67].

3.2.2 Effective density fluid model

Another more physical approach is to use the effective density fluid model (EDFM) [26], which was developed as a simplification of Biot's poroelastic model [23,24] taken at the limit of vanishing frame rigidity. The Biot poroelastic model predicts three waves: a fast and slow compressional wave as well as a shear wave. The slow compressional wave and shear wave velocities

are much lower than the fast compressional wave velocity and do not exist in the EDFM. The dispersion predicted by the fast compressional wave has two frequency regimes. A sound speed minimum is reached at the low frequency limit, where there is no relative fluid-solid motion [23], while a sound speed maximum is reached at the high frequency limit, where relative fluid-solid motion dominates the behavior [24]. The EDFM greatly reduces the number of input parameters from the full poroelastic model, while preserving the inertial effect due to relative fluid-solid motion that describes much of the dispersion seen in SAX99 and SAX04.

The EDFM has recently been modified to include thermal and granularity effects [68] in an effort to better describe behavior observed at the low and high-frequency limits [29, 31]. At the low frequency limit, it is hypothesized that the wave motion is no longer a predominately adiabatic process and thus heat is transferred between the fluid and grains, which effectively reduces the sound speed. Granularity effects are implemented using doublet mechanics (DM), developed to describe a frequency regime where continuum mechanics begins to break down, but where the grain diameter remains less than a half-wavelength. Grains are assumed to be arranged in a cubic tetrahedral packing and are inherently non-isotropic. Applying DM to the EDFM, the angle of wave propagation in the latice is evaluated at $\theta = 30°$, which corresponds to the direction of maximum sound speed. Sound speed data in this frequency regime [28–30] has shown a significant decrease in sound speed described in the literature by the presence of multiple scattering among grains.

The equation governing the modified EDFM (mEDFM) sound speed is

$$c = \sqrt{K_{\text{eff}}/\rho_{\text{eff}}}, \tag{3.2}$$

where K_{eff} is the effective bulk modulus of the sediment and ρ_{eff} is the effective density of the sediment. The effective bulk modulus incorporates both thermal and granularity terms in the form

$$K_{\text{eff}} = \zeta_{\text{DM}} \left(\frac{1-\beta}{K_{\text{g}}} + \frac{\beta}{\tau_{\text{th}} K_{\text{w}}} \right)^{-1}, \tag{3.3}$$

where K_{g} is the bulk density of the grain, and $K_{\text{w}} = \rho_{\text{w}} c_{\text{w}}^2$ is the adiabatic bulk density of water. The thermal term τ_{th} is defined as

$$\tau_{\text{th}}(\omega, \gamma, \nu) = \left[\gamma - (\gamma - 1) \left(1 - \frac{2}{b} \frac{J_1(\Upsilon)}{J_0(\Upsilon)} \right) \right]^{-1}, \tag{3.4}$$

where $\Upsilon = \sqrt{-i\omega\gamma a_{\text{p}}^2/v}$, ω is the angular frequency, γ is the ratio of specific heats of water, ν is the thermal diffusivity of water, and J_0 and J_1 are cylindrical Bessel functions. The granularity stiffness multiplier is represented by the following Taylor series of order $(d/\lambda)^6$

$$\begin{aligned} \zeta_{\text{DM}} = & \frac{1}{4\Gamma(4)} \left(4\Gamma(4) - \left(\frac{d}{\lambda} \right)^2 \frac{2^5 \pi^2}{4!} \Gamma(6) \right. \\ & \left. + \left(\frac{d}{\lambda} \right)^4 \frac{2^7 \pi^4}{6!} \Gamma(8) - \left(\frac{d}{\lambda} \right)^6 \frac{2^9 \pi^6}{8!} \Gamma(10) \right), \end{aligned} \tag{3.5}$$

where

$$\Gamma(n) = \cos(\theta)^n + \cos(60^\circ - \theta)^n - \cos(60^\circ + \theta)^n. \tag{3.6}$$

The effective density of the sediment is that presented in the original paper [26],

$$\rho_{\text{eff}} = \rho_{\text{w}} \left(\frac{\tau(1-\beta)\rho_{\text{g}} + (\tau - 1)\beta\rho_{\text{w}} + \frac{i\rho F \eta}{\rho_{\text{w}} \omega \kappa}}{\beta(1-\beta)\rho_{\text{g}} + (\tau - 2\beta + \beta^2)\rho_{\text{w}} + \frac{i\beta F \eta}{\omega \kappa}} \right), \tag{3.7}$$

where τ is the tortuosity, κ is the permeability, and ν is the viscosity of water. The function F predicts how fluid motion deviates from Poiseuille flow as frequency increases, assumes cylindrical pores, and is given as

$$F(\epsilon) = \frac{\frac{\epsilon}{4}T(\epsilon)}{1 - \frac{2i}{\epsilon}T(\epsilon)}, \tag{3.8}$$

where the function

$$T(\epsilon) = \frac{-\sqrt{i}J_1(\epsilon\sqrt{i})}{J_0(\epsilon\sqrt{i})}, \tag{3.9}$$

and where the parameter $\epsilon = a_{\mathrm{p}}\sqrt{\omega\rho_{\mathrm{w}}/\eta}$ is a function of the pore size parameter $a_{\mathrm{p}} = \sqrt{8\tau\kappa/\beta}$. It is worthwhile noting $\rho_{\mathrm{eff}}(\omega \to 0) = \rho$.

3.3 Description of the measurements

3.3.1 Layered waveguide

The layered waveguide used in this work is a model waveguide constructed in the laboratory (see Figure 3.1) that consisted of a water-saturated glass bead column (WSGBC) confined by a nylon tulle net sleeve, surrounded by an annular layer of water, a Pyrex glass tube, and air. A 0.8 mm-thick neoprene rubber membrane was clamped to the bottom of the glass tube to keep the water from leaking out of the waveguide. The waveguide was terminated at the top with an air/water interface, and at the bottom with several sheets of expanded polystyrene (EPS) foam, approximating pressure release boundary conditions. The model sediment was comprised of 1 mm-diameter soda lime glass beads chosen due to their uniform grain diameters and well-tabulated material properties. Also, the beads are largely crack free, thereby minimizing

the possibility of air bubbles residing inside grain crevices [69]. To prepare the WSGBC, the sleeve was first filled with dry beads and sewn shut using nylon monofilament, resulting in an air-saturated glass bead column (ASGBC). Approximating the ASGBC as a cylinder, the length and mean diameter were measured to calculate the volume. The mean diameter was calculated by using several caliper readings along the length of the column. The mass of the ASGBC was also measured. Both volumetric and mass measurements of the ASGBC discounted the thickness and mass of the sleeve.

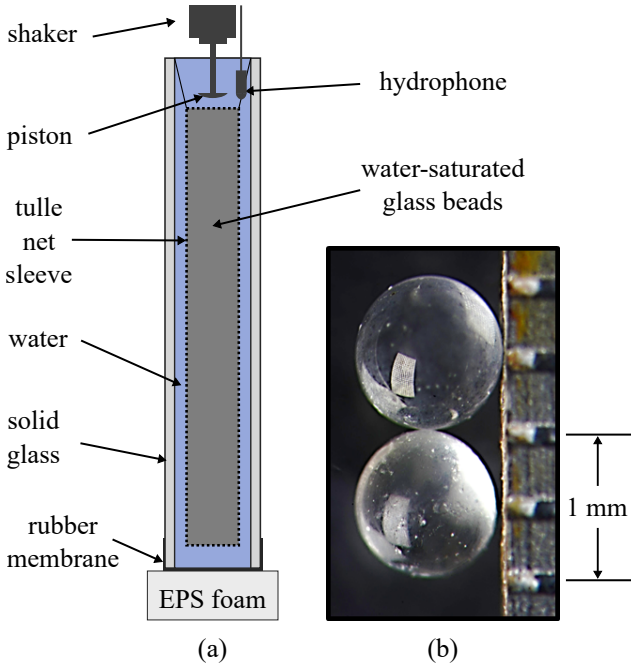

Figure 3.1: A schematic of the layered waveguide experiment is shown in (a) terminated by air and foam. Layers were comprised of water-saturated 1-mm-diameter soda-lime glass beads confined by a nylon tulle net sleeve, water, solid glass, and air. The piston source and hydrophone receiver were located in the water layer. A photomicrograph of two typical beads is shown in (b) next to a machinist's rule.

Next, the ASGBC was submerged under fresh water. The WSGBC was then degassed underwater by agitating it for three days in a vacuum chamber at 9.1 kPa, and transferred into the glass tube under degassed water in a tank to minimize the reintroduction of air bubbles into the WSGBC. The entire water-saturated layered waveguide was removed from the tank and placed atop the EPS foam sheets. The WSGBC was then suspended, and centered axially and radially in the glass tube. A piston attached to an electro-mechanical shaker and hydrophone were placed within the water layer near the top of the waveguide and the system was left overnight to allow any potential entrained air bubbles to dissolve back into the degassed water.

3.3.2 Resonance measurement

Carefully maintaining the height of the water flush with the top of the tube, a PC-based data acquisition system (DAQ) sent 10 sequential one-second-duration logarithmic chirps (0.5 kHz to 8 kHz) through an amplifier to the shaker, ensonifying the waveguide. The acoustic pressure was then sensed by the hydrophone, and the resulting signal was preamplified and acquired by the DAQ. The cross and auto power spectrums of the received hydrophone signal and the source voltage signal were calculated and averaged across the 10 received chirps. The transfer function H_{SR}, which represents the drive-voltage-normalized pressure spectrum within the waveguide, and coherence C_{SR} between source and received signals were then calculated using the ex-

pressions

$$H_{\mathrm{SR}}(\omega) = \frac{\overline{G}_{\mathrm{SR}}(\omega)}{\overline{G}_{\mathrm{SS}}(\omega)}, \tag{3.10}$$

$$C_{\mathrm{SR}}(\omega) = \frac{|\overline{G}_{\mathrm{SR}}(\omega)|}{\overline{G}_{\mathrm{SS}}(\omega)\overline{G}_{RR}(\omega)}, \tag{3.11}$$

where $\overline{G}_{\mathrm{SR}}$ is the averaged cross power spectrum, $\overline{G}_{\mathrm{SS}}$ and $\overline{G}_{\mathrm{RR}}$ are the averaged auto power spectrums of the source and received signals, respectively. The amplitude of the drive signal was adjusted to achieve near-unity coherence, ensuring a sufficient signal-to-noise ratio and an absence of nonlinearity. The local maxima of the magnitude of the transfer function were used to determine the resonance frequencies of the waveguide. At resonance, the coherence did not fall below 0.99. Each resonance frequency was matched to its associated axial mode number $m = 1, 2, 3...$. The start and end frequencies of the chirp were chosen well below the frequency of the first higher-order mode to eliminate any ambiguity in pairing resonance frequencies with modes and to only excite the lowest order, plane-wave-like modes of the elastic-walled waveguide. The axial component of the phase speed in the waveguide was calculated as

$$c_{\mathrm{ph}} = f_m \lambda_m, \tag{3.12}$$

where f_m is the system's resonance frequency, $\lambda_m = 2L/m$ is the wavelength between two pressure release boundaries at axial mode number m, and L is the length of the waveguide. Resonance techniques have been successful at measuring effective medium sound speeds of bulk materials such as sediment [20, 21, 38, 70] or suspended scatterers in water such as methane hydrates [71], bubbly liquids [72–74], and seagrass [75–79], while to the authors'

knowledge, this work is the first to apply such a technique for a layered waveguide inference process.

3.3.3 Direct high-frequency sound speed measurement

Direct, high-frequency sound speed measurements were performed radially at several positions along the length the WSGBC. These measurements served as an independent data set to compare with the sound speeds determined from the layered waveguide inferences. After the resonance measurement was performed, the layered waveguide was submerged into a 1.5 m by 0.9 m by 0.9 m water-filled tank, where the WSGBC was removed from the glass tube and vertically suspended. The system was kept submerged overnight to allow the temperature to reach equilibrium. An aluminum fixture was used to position and align two 12.7-mm-diameter, 1 MHz immersion transducers on either side of the WSGBC (Figure 3.2). The face of the transducers were positioned flush to the inside walls of the fixture, which were separated at a fixed distance of 46.3 mm, and the face of both transducers were located 2.8 mm on either side the WSGBC. The fixture was rigidly mounted to a positioning system that translated the transducers vertically relative to the stationary WSGBC. Circular guides on the top and bottom face of the fixture kept the WSGBC in a consistent position in relation to the transducers during the experiment. At each position, the function generator produced a 1-ms-duration, logarithmic chirp (1 kHz to 1 MHz) every 100 ms. Since the target frequency range (100 kHz to 500 kHz) was below the resonance frequency of

the transducer, a logarithmic chirp was used to enhance the energy in the target frequency band. The chirp was amplified and directed to the transmit transducer (TX). After propagation through the WSGBC, the signal was received by the receive transducer (RX), pre-amplified, and acquired by the oscilloscope (sampled at 5 MHz), where 512 averages were performed. A reference measurement was also performed through water without the WSGBC present.

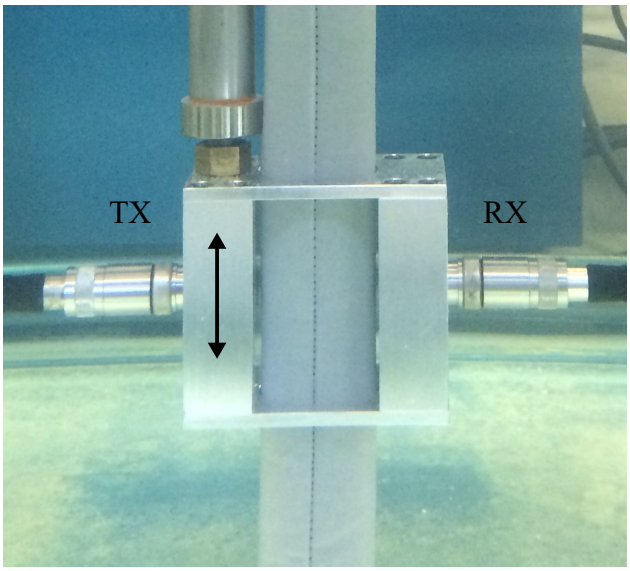

Figure 3.2: Direct high frequency sound speed measurement across diameter of WSGBC as a function position along the length of the column.

Due to the presence of the fixture and the duration of the signal, received chirps both with and without the WSGBC were composed of direct and secondary arrivals. In order to isolate the direct arrival, the impulse response was calculated by convolving the received signals with the inverse of

the generated chirp given by

$$s^{-1}(t) = \mathscr{F}^{-1}\left\{\frac{1}{\mathscr{F}\{s(t)\}}\right\}, \tag{3.13}$$

where $\mathscr{F}$ and $\mathscr{F}^{-1}$ are the Fourier and inverse Fourier transforms, respectively, and where $s(t)$ is the chirp resampled at 2 MHz. The chirp was resampled such that the Nyquist frequency and the maximum frequency of the chirp were equal to avoid singularities when performing the spectral inverse. Once the inverse chirp was transformed back into the time domain, it was resampled to the original sampling rate of 5 MHz and convolved with the received signals, resulting in the impulse response. The extra-wide bandwidth of the chirp, when compared with the target frequency range, allowed for sufficient pulse compression to successfully isolate the direct arrival. Further description of these signal processing techniques are described in References 80, 81, and 82.

After the impulse responses through the WSGBC and through water alone were calculated, the direct arrivals were windowed, and the sound speed was calculated by

$$c = \frac{c_{\mathrm{w}}}{1 - \frac{c_{\mathrm{w}}\Delta\phi}{\omega D}} \tag{3.14}$$

where $\Delta\phi$ is the unwrapped phase of the cross power spectrum between the two received impulse responses, and D is the diameter of the WSGBC [9]. Since the diameter of the WSGBC was large compared to the diameter of the transducer, the WSGBC diameter was assumed to be the primary path length through the WSGBC. Path length deviations due to the finite curvature of the WSGBC were included in the experimental uncertainty. The author is aware

that the sound speed calculated by Equation 3.14 is analogous to the free-field phase speed through the WSGB, unconstrained by the waveguide. However, throughout this monogram, the free-field phase speed will be explicitly referred to as sound speed to avoid confusion.

3.4 Inference process

To infer the sound speed of the WSGB within the sleeve, a two-dimensional axisymmetric FEM was created in COMSOL to simulate the resonance measurement. The water and WSGB were modeled as fluids. The glass tube was modeled an elastic solid, and the fluid-structure interaction physics was invoked in COMSOL to couple the domains. The top and bottom of the water were defined as pressure release boundaries, and the outer glass tube surfaces in contact with the air were defined as free. The material properties and dimensions of the glass tube (Table 3.1) were either provided by the manufacturer or directly measured. The water had a density of 998 kg/m^2 and a sound speed determined by the water temperature of the experiment [83]. The WSGBC suspended in the water domain had a length of 0.513 m and a mean radius of 2.036 cm, matching that measured in the experiment. A stainless steel piston was prescribed a vertical acceleration across the frequency band of the experiment in 1 Hz increments. Following solution of the FEM, the acoustic pressure, at the same location as the hydrophone in the resonance measurement, was extracted and normalized by the amplitude of the piston acceleration. Phase speeds were extracted from the normalized spectra us-

ing the same procedure that was used in the resonance measurement, and previously described in Section 3.3.2.

Table 3.1: Glass tube properties used in the FEM simulation of layered waveguide measurement.

tube property	symbol	value
density[T]	ρ_t (kg/m^3)	2230
Poisson's ratio[T]	ν	0.2
Young's modulus[T]	Y (GPa)	60
length[M]	L (m)	0.61
inner radius[M]	b (cm)	2.56
outer radius[M]	d (cm)	3.49

[T] Tabulated properties
[M] Measured properties

The domain representing the WSGB was modeled as a fluid, using either the CDFM, FDFM, or mEDFM. For the CDFM, the bulk density of the WSGB domain was held fixed while the frequency-independent sound speed was varied until the sum of the squared error was minimized between phase speeds extracted from the simulation and measured in the resonance measurement. For the FDFM, the bulk density was held fixed like in the CDFM, however the sound speed of the WSGB was varied at each resonance frequency until the simulated phase speed matched the measured phase speed. The bulk density was calculated using Equation 3.1, by first determining $\beta = 1 - m_{\text{dry}}/\rho_g V$. The grain density was taken from Argo [65], where glass beads of the same material and manufacturer were used. When modeling the WSGB as a mEDFM, all parameters were either measured directly or taken from the literature except permeability and tortuosity. The Kozeny-Carmen relation [84] was used

to couple the two and is given by

$$\kappa = \frac{\beta^3 d^2}{36 K_0 \tau^2 (1-\beta)^2}, \tag{3.15}$$

where the shape factor $K_0 = 2$ was assumed for cylindrical pores. Thus coupled, the tortuosity was left as the independent fit parameter. For each tortuosity value, the simulation would assign a complex frequency-dependent sound speed from Equation 3.2 and effective density from Equation 3.7 to the WSGB domain, and compute the normalized pressure spectra. The tortuosity was varied until the simulated phase speed reached agreement with the measured phase speed, through minimization of the error function displayed in Equation 2.140 in Sen and Stoffa [85]. The resulting best-fit set of mEDFM parameters were then used to calculate the frequency-dependent effective density and sound speed of the WSGB. For the frequency band of the layered waveguide resonance measurement, the tulle net sleeve was experimentally determined to have a negligible effect, as its presence did not affect the locations of the peaks in the pressure spectrum when exciting a water-filled waveguide with and without the empty tulle net sleeve, and was, therefore, not included in the simulation.

3.4.1 Verification of the simulation

Prior to working with the glass beads, the simulation was verified for a water-filled case. The acoustic response of the system in absence of the sleeve filled with glass beads was measured, and the results were compared to the simulation. These were also compared to the predictions of an exact analytical

expression for the phase speed in a liquid-filled, infinite-length, lossless elastic tube waveguide with walls of arbitrary thickness, as given by Equation 5 of Lafleur and Shields [86] using glass tube properties from Table 3.1. The comparison to this analytical model addresses the effect to which the phase speed calculated within a finite length tube compares to a tube of infinite length, as well as verification that the resonance frequencies of the experiment have been paired with the correct mode.

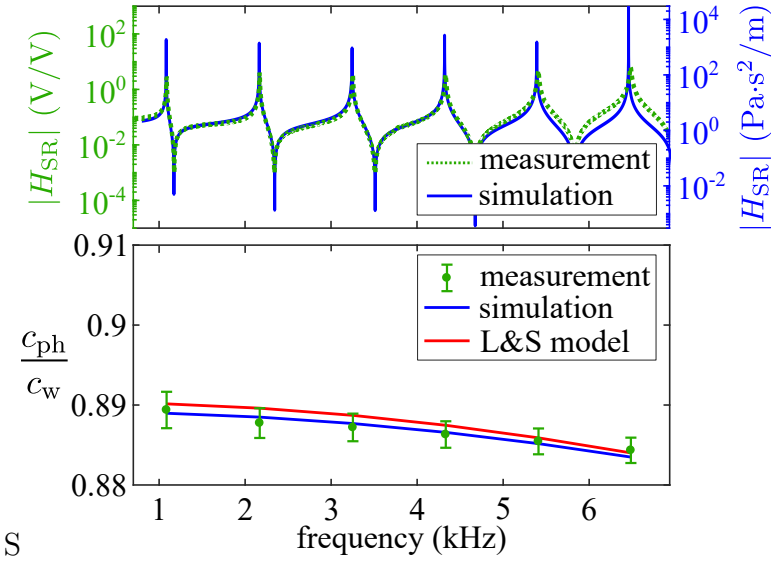

Figure 3.3: Top: Magnitude of the transfer function (H_{SR}) of resonance measurement (dotted green line) and simulation (solid blue line) of the finite-length water-filled waveguide. Bottom: Normalized phase speed in the measured (green dots) and simulated (blue line) water-filled waveguides of finite length, and exact phase speed of water-filled waveguide of infinite length (red line). Experimental error bars represent measurement uncertainty from the tube length, spectral resolution, and temperature resolution of the thermocouple.

The measured and simulated pressure responses are shown in the top panel of Figure 3.3. The resonance frequencies, identified as local maxima

of the transfer functions, in both the measurement and the simulation are in agreement. The source and receive signals used to calculate the transfer function in the experiment, described by Equation 3.10, however, had different units and magnitudes compared with the simulation and were, therefore, plotted on different vertical axes. The resonances in the measurement exhibited a lower quality factor than the resonances of the simulated system due to losses in the glass tube, rubber membrane, and EPS foam boundary condition not present in the simulation. This discrepancy, however, did not affect the values of the resonance frequencies and, therefore, did not affect the phase speed calculation shown in the bottom panel of Figure 3.3. The green data points in Figure 3.3 were calculated from the measured resonance frequencies using Equation 3.12. The blue curve represents phase speeds extracted from the simulation. The red curve is the prediction of an exact analytical model for an infinite length tube. The small difference between the two models is attributed the effect of the finite length tube, as described below.

The phase speed in the water-filled waveguide, in the measurement, simulation, and modeling results, was reduced by roughly 11% from the intrinsic sound speed of water, and exhibited negative dispersion, as expected from existing theory. The finite stiffness of the glass tube resulted in the general reduction in phase speed, while the mass of the glass tube wall was responsible for the negative dispersion [86]. The measurement error bars were determined by propagating uncertainty in the length of the waveguide and the finite spectral resolution of the transfer function through Equation 3.12, as

well as the resolution of the temperature probe used to determine the sound speed of the water [83] as the normalization factor.

The phase speed calculated from the simulation is about 0.2% lower than the phase speed predicted by the analytical model. This is most likely due to the free end boundary conditions of the elastic tube in measurement and simulation, which effectively increases the compliance of the tube terminations, thereby decreasing the overall phase speed in the waveguide. An exact analytical model for a finite-tube, liquid-filled elastic tube waveguide, to the authors' knowledge, does not currently exist and although this effect is quantifiable, it is within the measurement uncertainty and beyond the scope of this work, since the layered waveguide measurement will only be compared with the finite-length FEM simulation.

The agreement between the simulation, the analytical model, and the experiment verifies the following assumptions: 1) The foam bottom boundary condition in the measurement adequately emulates a pressure release boundary condition modeled in the simulation. 2) The material properties of the glass tube tabulated in Table 3.1 used in the simulation and exact analytic model are accurate within experimental error. 3) The manner in which the phase speed is calculated in the experiment and simulation is consistent, to within experimental error, with the phase speed of a layered waveguide of infinite length.

3.4.2 Effects of including the sediment layer

Next, the WSGBC was introduced into the FEM simulation using the mEDFM. The absolute value of the simulated pressure field along the radial dimension is shown in Figure 3.4. The pressure was normalized by the maximum value at each resonance frequency to compare the various pressure fields at different axial mode numbers, m. Although the radial pressure field diverged from plane wave motion as the value of m increased, modes were relatively planar to within 6%.

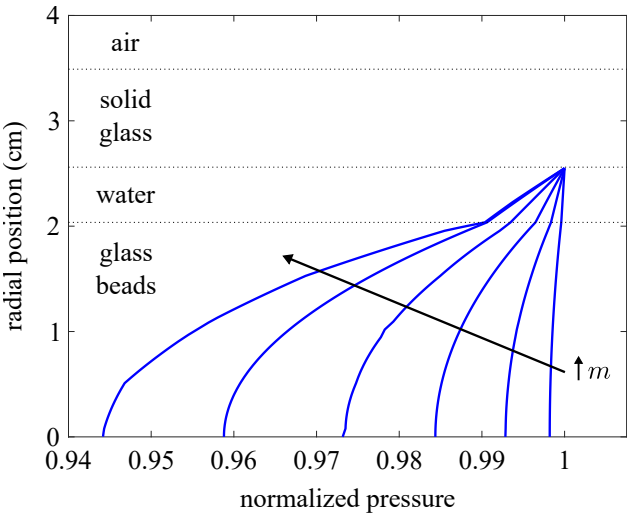

Figure 3.4: Normalized pressure field within the waveguide as a function of radial position. The dotted lines distinguish the different layers in the waveguide. The radial position equal to zero represents the line of rotational symmetry. As the axial mode number m increases in the direction of the black arrow, the planarity decreases.

For mode numbers $m = 1, 2, 3$, the absolute value of the pressure field near the middle of the WSGB layer ($r = 0.1$ cm) and at the outer edge of the

water layer ($r = 2.46$ cm) is plotted along the axial direction in Figure 3.5. The pressure along the middle of the WSGB layer could only be plotted to 59 cm due to the presence of the piston. Pressure was normalized by the maximum value at each mode in either layer. Axial standing-wave patterns in both layers were identical. This observation verified the assumption, represented by Equation 3.12, for extracting phase speeds from resonance frequencies for a finite-length layered waveguide. In other words, at the resonance frequencies of the layered system, although the pressure and particle velocity may be different as a function of radius, the phase speed is equal.

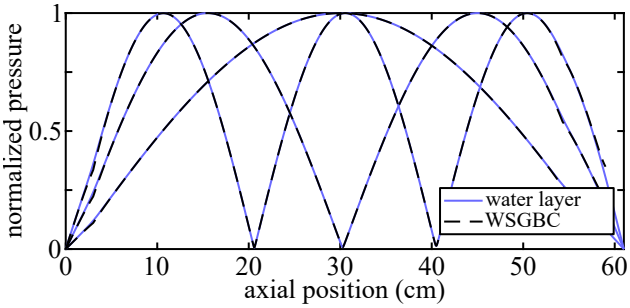

Figure 3.5: Normalized pressure field within the water layer and the WSGBC in the waveguide as a function of axial position for $m = 1, 2, 3$.

3.5 Results

As described in Section 3.3, resonance frequencies observed in the measured system are directly related to the frequency-dependent phase speeds of the plane-wave-like modes in the layered waveguide. However, those phase speeds differ from and are dependent upon the intrinsic sound speeds in both the water layer and in the WSGBC. The finite-element simulation was used

to determine the resonance frequencies of the system, using three different effective medium approaches to represent the WSGBC within the simulation. The input parameters of those fluid models were varied until the resonance frequencies predicted by the simulation agreed with the resonance frequencies observed in the measurements, yielding inferences of the acoustic properties that were compared with direct sound speed measurements.

3.5.1 Resonance measurement/simulation phase speed comparison

In Figure 3.6, the measured phase speed in the waveguide is compared with the best-fit simulation considering the WSGB as a mEDFM, CDFM, and FDFM. The mEDFM better described the dispersion observed in the experiment, while the CDFM over predicted the waveguide phase speed below 4 kHz and under predicted the waveguide phase speed above 4 kHz by at most 8 m/s. For some applications in forward modeling, this level of agreement is acceptable, since the measurement uncertainty of a typical ocean waveguide can be of comparable order. Since the FDFM was individually fit to each measured phase speed data point, agreement with the measurement was expected. However, when inferring sediment physical parameters from measured waveguide phase speed, drastic differences arise depending on which fluid model is used.

Table 3.2 displays the best-fit model parameters associated with the results in Figure 3.6. The inferred tortuosity value from the mEDFM simulation is higher than that reported for sand, but is consistent with the findings from several experiments using monodisperse glass beads [65, 87–89]. Also, tortuos-

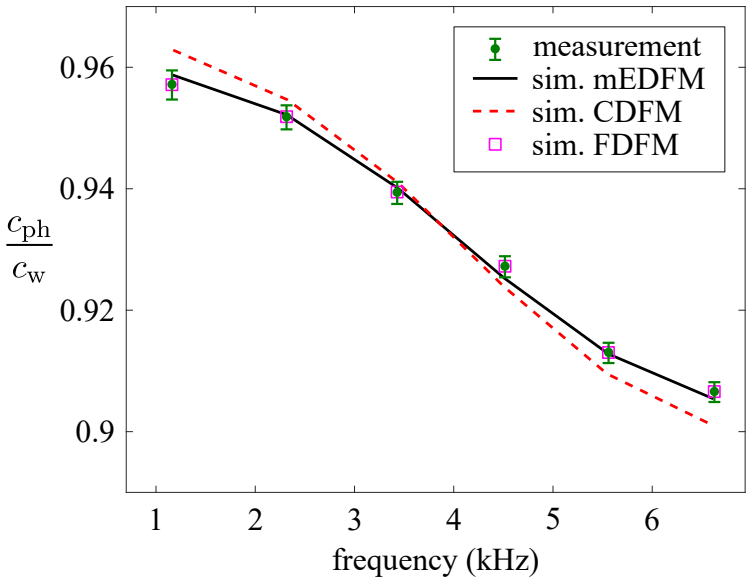

Figure 3.6: The measured phase speed in the layered waveguide as a function of frequency (green data points and error bars). Error bars were propagated from the uncertainty of the waveguide length, and finite spectral and temperature resolution. The black solid line, red dashed line, and magenta squares are the best-fit simulated phase speeds modeling the WSGB as an mEDFM, CDFM, and FDFM, respectively.

ity has been shown to be inversely proportional to porosity [87]. The relatively low measured porosity reported for these WSGB could explain the higher tortuosity value. Next, the sound speed value required for the CDFM simulation to fit the measurement is uncharacteristically high for glass beads [65]. The inferred sound speed assuming an FDFM is also uncharacteristically high, and ranged from 1906 m/s near 1 kHz to 2035 m/s near 7 kHz.

Table 3.2: CDFM and mEDFM simulation input parameters that achieved the best waveguide phase speed agreement with experiment.

model	parameter	symbol	value
mEDFM	density of water[T]	ρ_{w} (kg/m^3)	998
	density of grain[T]	ρ_{g} (kg/m^3)	2487
	bulk modulus of water[T]	K_{w} (GPa)	2.21
	bulk modulus of grain[T]	K_{g} (GPa)	39.8
	viscosity of water[T]	η (Pa $\cdot$ s)	9.63×10^4
	porosity[M]	β	0.31
	permeability[C]	κ (m^2)	5.30×10^{-10}
	tortuosity[F]	τ	1.27
	mean grain diameter[M]	d (mm)	1
	ratio of specific heats[T]	γ	1
	thermal diffusivity of water[T]	ν (m^2/s)	1.49×10^{-7}
CDFM	bulk density of sediment[M]	ρ (kg/m^3)	2025
	sound speed of sediment[F]	c (m/s)	1970

[T] Tabulated parameter.
[M] Measured parameter.
[F] Fit parameter.
[C] Coupled to fit parameter using Equation 3.15.

3.5.2 Inferred/direct sound speed comparison

The inference results are shown in Figure 3.7. The black x's are the inference results when the mEDFM was used within the simulation to model the WSGB. The red crosses and the magenta squares are the inference results when using the CDFM and the FDFM, respectively. The high-frequency sound speeds measured directly through the WSGB are shown with the blue circle data points along with blue error bars that represent the 95% confidence intervals for those depth-averaged measurements. The mEDFM model predictions, below, at and above the frequency range of the inferences are also

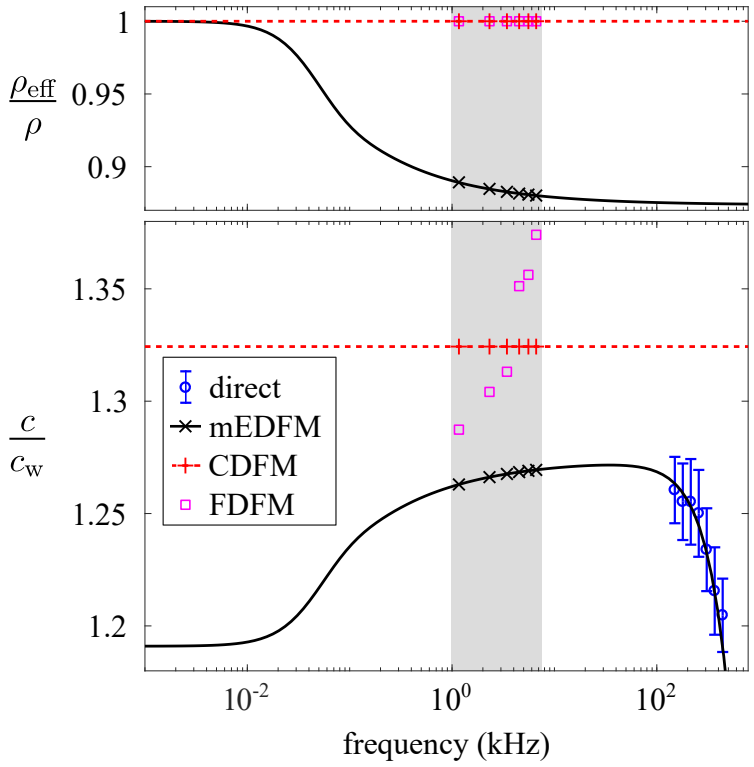

Figure 3.7: Results of the layered waveguide inferences using three different sediment models are shown. The gray regions indicate the frequency band of the inference. Top: Inferred density normalized by sediment bulk density. Bottom: Inferred sound speed ratio. Inferred sound speeds using mEDFM (black x's), CDFM (red crosses), and FDFM (magenta squares) compared with high-frequency direct measurements (blue circles). Error bars represent 95% confidence interval of the depth-averaged sound speed. The black solid line and red dashed lines extend the mEDFM and CDFM, respectively, to a wider frequency range to compare inference results with direct sound speed measurements.

shown in Figure 3.7 using solid black lines. The inference results at the resonance frequencies of the system coincide with the black x's, which overlay the solid line by definition. The dashed red line is used to visually extend the frequency range of the inference result for the CDFM, and it is clear that the

direct measurements (blue circles) match the mEDFM much better than the CDFM.

Although sound speed was estimated only at each measured resonance frequencies for the FDFM and could not be extended outside the frequency range of the layered waveguide experiment, sound speed trended toward non-physically high values inconsistent with the direct measurements. The non-physical sound speed values inferred from modeling the WSGB as an FDFM also supports the claim that, within the frequency range measured in the layered waveguide (1 kHz to 7 kHz), the observed phase speed dispersion could not be explained by a frequency-dependent bulk modulus.

When modeling the glass beads as a fluid in a frequency regime where the effective density predicted by the mEDFM deviated significantly from the bulk density, neglecting poroelastic effects by assuming a constant bulk density yielded a gross overestimation of sound speed by between 36 m/s near 1 kHz to 156 m/s near 7 kHz. The physical mechanism that causes the reduction in effective density is due to the relative motion between the fluid and the grains. Without accounting for this rheological effect, inferences can produce nonphysical estimates of sediment sound speed as was originally mentioned by Williams [26]. Theoretically, this overestimation is diminished as the frequency approaches that of the low frequency limit, where the mEDFM predicts a convergence in the effective density to the bulk density. In the case of a granular sediment with mean diameter of 1 mm, this convergence occurs on the order of 10 Hz. For sands in the SAX99 experiment, for example, the

low frequency limit occurs at a higher frequency on the order of 100 Hz.

3.6 Conclusion

A layered waveguide system, consisting of a model water-saturated sediment, comprised of 1-mm-diameter glass beads, overlaid by a layer of water and solid glass, was constructed in the laboratory. The sound speed within a model water-saturated sediment was inferred by fitting the phase speed in a simulation of the system with the phase speed measured in the experimental system, in the frequency band from 1 kHz to 7 kHz. The WSGB domain in the simulation was modeled as either a mEDFM, CDFM, or FDFM. At frequencies from 150 kHz to 450 kHz, direct sound speed measurements within the WSGB were also obtained. Sound speed inferences made with the mEDFM agreed with the direct measurements, while inferences made with the CDFM or FDFM significantly overestimated the sound speed of the WSGB and did not agree with direct measurements. For the layered waveguide and frequency range used in this work, self-consistency between inferences and direct measurements was only achieved if the sediment model used in the inference accounted for the inertial effects between the grains and pore water.

The ability to measure the sound speed of marine sediment at a broad frequency range was crucial in this work to test the models. In Chapter 4, a fully-automated apparatus is presented capable of measuring the sound speed and attenuation across a frequency range that spans nearly four orders of magnitude.

Chapter 4

The Core And Resonance Logger (CARL)

4.1 Introduction

The collection of sediment cores is ubiquitous across a multitude of science and engineering disciplines. There are many methods to acquire core samples, but, in general, sediment samples are taken at depth by inserting a tube into the sediment, extracting the trapped sediment from the seabed, and taking the sample to either a shipboard or shoreside laboratory for processing. The coring process can yield information about biological, geological, chemical, and mechanical properties of the sediment, such as quantifying benthic infauna, mineral composition, grain size distributions, geologic age, chemical composition, density, porosity, permeability, etc.

Many acoustic measurements have also been performed in the laboratory on a broad range of marine sediments extracted from the ocean bottom, mainly utilizing pulse or resonance techniques [18, 20, 21, 40, 70, 90–92]. It has been shown that sediments *in situ* behave differently than at atmospheric pressure and temperature [9]. To account for this, Hamilton instituted the term "velocity ratio," refered to here as the sound speed ratio, which normalizes the sound speed of the sediment by the sound speed of the pore fluid [19].

Sound speed ratio measured in the laboratory can then be corrected to *in situ* by multiplying the sound speed ratio by the sound speed of the *in situ* pore fluid calculated from *in situ* salinity, pressure, and temperature using empirical relations [49]. This correction has been validated by measurements performed in References 70, 91, and 92, which demonstrated that the change in sediment sound speed at different pressure, temperature, and salinity, was approximately proportional to the change in pore water sound speed over the same conditions. As discussed in Chapter 2, in environments where the bottom water experiences high levels of variability, the author recommends measuring the pore fluid salinity and temperature of the sediment to more accurately calculate the sound speed ratio. Sediment attenuation has been shown, in laboratory measurements at high frequencies (500 kHz to 1 MHz), to decrease with temperature in sandy sediments, and increase with temperature in muddy sediments [93, 94]. However, this effect is small compared with the variability observed among different types of marine sediments.

Performing acoustic measurements on sediment core samples is beneficial, because it allows the acoustic properties to be compared with various other sediment properties from the same sample. This is not the case, for example, when comparing *in situ* acoustic measurements with sediment properties obtained from a nearby sediment core, particularly in sediments with high levels of spatial variabliy. The U.S. Naval Oceanographic Office was the first [9] to develop the pulse technique to measurement sediment sound speed within cores using oil-filled transducers that couple externally to the core liner

walls [39] and was later adapted by others [40]. This technique is typically performed at high frequencies in the hundreds of kilohertz by comparing the transmitted pulse through a reference sample of known sound speed with that of the cored sample. A resonance method was also established, where the resonance frequencies of a cylindrical sediment core in the tens of kilohertz were used to infer the sample sound speed [20, 21, 37, 70]. The aforementioned measurement techniques have appeared extensively in the literature and were used to create the classical data sets used by naval and underwater acoustics communitities. However, compressional and shear wave speeds and attenuations were typically reported at just a single frequency.

Recently, as sonar and modeling capabilities have improved, there has been more interest in quantifying the acoustic properties of marine sediment in a broader frequency band and at finer frequency resolutions [31, 64]. For example, a laboratory experiment was performed in large 0.8-m-tall, 0.686-m-diameter container of water-saturated sand by combining both high and low frequency methods to measure dispersion predicted by sediment models [38]. The work reported in Reference 38 also inspired the measurement presented in Chapter 3. While both experiments included broad-band acoustic measurements on a controlled laboratory sediment, they are not practical to use on core samples from the field.

Geotechnical companies have recently been manufacturing intricate and expensive multi-sensor core loggers that can automate the time-consuming logging process. The objective of this chapter is to present the methodol-

ogy of how to build and use an automated broad-band Core and Resonance Logger (CARL) from relatively inexpensive off-the-shelf parts and laboratory equipment, such that this technology becomes more accessible to scientists. Section 4.2 describes the CARL apparatus and its methodology. The efficacy of CARL is validated in Section 4.3, by comparing measurements made in two oils using CARL, to measurements made with a more standard immersion technique. The effect of sample rigidity is addressed in Section 4.4 and conclusions are summarized in Section 4.5.

4.2 Description of CARL

CARL, in its present form, is a fully automated broad-band core logger capable of measuring the speed of sound in a field-collected core or a laboratory sample, up to a meter in length, from 10 kHz to 7 MHz and attenuation from 100 kHz to 7 MHz. The attenuation measurement from 10 kHz to 100 kHz requires further investigation and is, therefore, not included in this chapter. Different versions of CARL could be adapted to different core lengths and different frequency ranges, as needed by the user. CARL has two modes of operation shown in Figure 4.1. The first is a pitch-catch mode that resembles a conventional core logger, and the second is a resonance mode.

The apparatus is comprised of a frame that consistently positions the core sample in a vertical orientation. Elastic straps at the top and bottom of the core maintain the sample in place during the measurement. A one-meter-

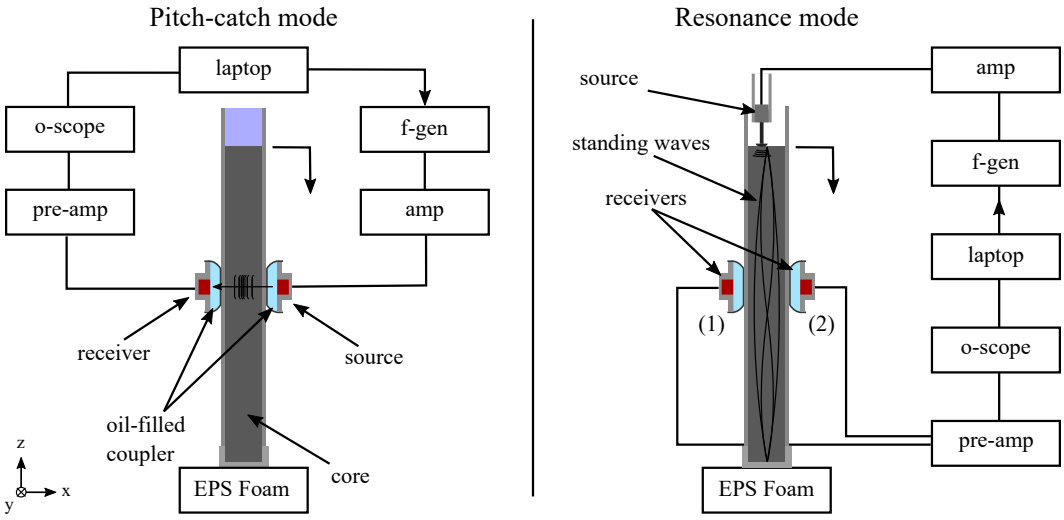

Figure 4.1: Schematic of CARL performing both modes of operation.

long V-Slot NEMA 17 Linear Actuator Bundle purchased from OpenBuilds[1] consists of a stepper motor that turns a lead screw, which vertically translates a follower. The follower is rigidly attached to two oil-filled CARL transducers (described in detail below) positioned on opposite sides of the sample's diameter (Figure 4.1). Olympus Ultrasonic Couplant B is placed on the contact surfaces between the transducer and core liner to minimize friction while improving acoustic coupling. Transducers of various frequency ranges are used within the oil-filled assembly to broaden the frequency range of the system. The distance between the transducers can be manually adjusted to accommodate any core liner with an outer diameter less than 20 cm. A Matlab-based graphical user interface (GUI) is programmed to control the vertical position

[1] openbuildspartstore.com/v-slot-nema-17-linear-actuator-bundle-lead-screw/

of the transducers by sending gcode[2] to the gshield-mounted[3] Arduino Uno, which interprets the command and supplies the appropriate number of steps to the stepper motor to translate the transducers.

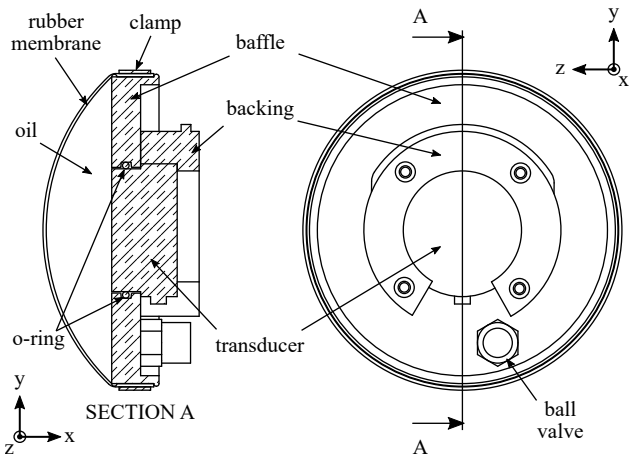

Figure 4.2: Section-view drawing of a removable oil-filled CARL transducer.

The transducer assemblies are comprised of a pair of Olympus contact transducers each housed in an oil-filled enclosure comprised of a 0.8-mm-thick sheet of neoprene clamped to an aluminum baffle (Figure 4.2), similar in appearance to the oil-filled core logger transducer housing found in Richardson [40]. The deformable rubber membrane provides adequate coupling to the cylindrical surface of the sample. The baffle is machined such that when the transducer is inserted into the baffle through an o-ring-sealed bore, the active surface of the contact transducer remains flush with the baffle surface. The baffle also contains a one-way ball valve used to fill the enclosure with oil.

[2]Gcode is a widely used numerical control programming language.
[3]synthetos.myshopify.com/collections/assembled-electronics/products/gshield-v5

To avoid the entrapment of air bubbles during assembly, the transducers were assembled under degassed oil (Nye Lubricant Synthetic Oil 182S) using the following procedure. The housing and an empty syringe were placed into an empty container and held under vacuum at 10 Pa of absolute pressure. Under vacuum, degassed oil was flushed through the housing, which flowed into the ball valve and out through the bore, filling the container with oil. After the housing was kept under oil and under vacuum for one hour, the container was returned to atmospheric pressure. Assembled under oil, the transducers were slowly submerged into the oil-filled container without entrapping any bubbles, inserted into the housing, and bolted in place with an aluminum backing. Still under oil, the empty syringe pulled 30 mL of the surrounding degassed oil that was then injected through the ball valve, filling the housing with oil and completing the assembly process. This process was repeated to fill three pairs of transducers using the Olympus contact transducers V101-RM, V102-RM, and A120S-RM with resonance frequencies at 500 kHz, 1 MHz, and 7.5 MHz, respectively.

4.2.1 Pitch-catch mode

In pitch-catch mode, CARL measures sound speed and attenuation as a function of frequency and depth within the core. At each depth, tone busts at the desired center frequencies f_c are created in and uploaded to the function generator by the GUI. The number of cycles n is rounded down to the nearest

half-cycle determined by

$$n = \frac{1}{2}\left\lfloor 2(\sqrt{2}-1)\frac{Df_c}{c}\right\rfloor, \tag{4.1}$$

where D is the inner diameter of the core measured with a telescoping bore gauge when the sample is placed between the transducers, and c is the sound speed of the sample, which is estimated before performing the measurement. This calculation is performed so the direct arrival does not overlap with the multipath from the walls of the core liner. A Tukey window was applied on the first and last 25% of the tone burst to minimize transients caused by the transducer's response. After the signal is generated, it is amplified and emitted from the source transducer, which produces a compressional wave that propagates across the diameter of the sample. The transmitted signal is then sensed by the receive transducer on the opposite side of the core. The received signal is conditioned by a pre-amplifier, displayed on the oscilloscope, and acquired by the laptop. Multiple receive pulses of the same center frequency are typically averaged 10 times to improve the signal-to-noise ratio (SNR).

To improve SNR across a wider frequency band, equalization is performed such that the received pulses transmitted through a water-filled core liner are 75% of the maximum amplitude before the pre-amplifier clipped the signal. The equalization is preformed until the pulse amplitude sent from the function generator surpasses the recommended maximum input voltage of the amplifier. SNR curves are plotted in Figure 4.3 through a water-filled core liner using the three transducer pairs. The solid and dashed lines show the

SNR before and after equalization, respectively. The 7.5 MHz transducer is not equalized, since the received tone bursts could not produce a sufficiently high-amplitude signal to clip the pre-amplifier. The tone-bursts emitted from the 7.5 MHz transducer were, therefore, generated with an amplitude equal to the maximum recommended input voltage of the amplifier across all frequencies. Due to the coupling between the contact transducer and the oil-filled housing, the resonance frequency of the CARL transducers is reduced, particularly for the 7.5 MHz transducers. The noise level measurement was performed on the portion of the signal before the arrival of each pulse.

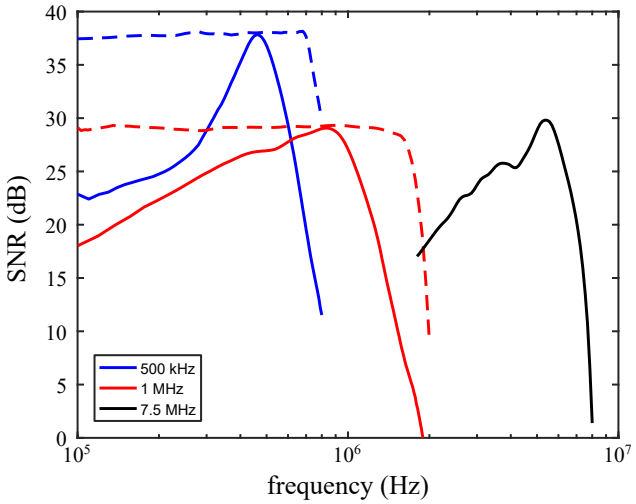

Figure 4.3: SNR for three CARL transducers through a water-filled core liner. Equalization yields a flatter response and improved SNR across a wider frequency band as shown by the dashed lines.

The amplitude and time delay of the receive pulse are affected by an inherent system response, in addition to from the time delay and attenuation associated with the signal propagating through the sample. To isolate the

contribution from the sample, the technique requires a reference measurement with identical equipment and on a core liner filled with a known material. Degassed distilled water of known temperature is typically used as the reference material [9], and the sample sound speed c and attenuation α are calculated by

$$c = \frac{c_{\mathrm{w}}}{1 - \frac{c_{\mathrm{w}}\Delta t}{D}}, \tag{4.2}$$

$$\alpha = \frac{20}{D}\log_{10}\left[\frac{|S_{\mathrm{w}}(f_{\mathrm{c}})|}{|S_{\mathrm{s}}(f_{\mathrm{c}})|}\right], \tag{4.3}$$

where Δt is the time delay between receive pulses through the water and sample-filled core, and S_{w} and S_{s} are the Fourier transforms of the receive pulses through the water and sample-filled core, respectively. The attenuation measurement is particularly sensitive to variability in the contact area made between the rubber housing and core liner. This variability can be caused by differences in core liner geometry, either as a function of depth, or between the reference core liner and sample core liner. To minimize attenuation uncertainty, the reference measurement is made at various depths for each core liner before the sample is collected or prepared. The signal processing algorithm processes the sample signal twice relative to the nearest two reference measurements, and performs an interpolation in depth.

The signal processing algorithm by which the time delay and the ratio of spectral amplitudes are calculated is automated based on established methods [95]. This algorithm, however robust, is always checked in post-processing by manually inspecting the normalized time-aligned raw signals to

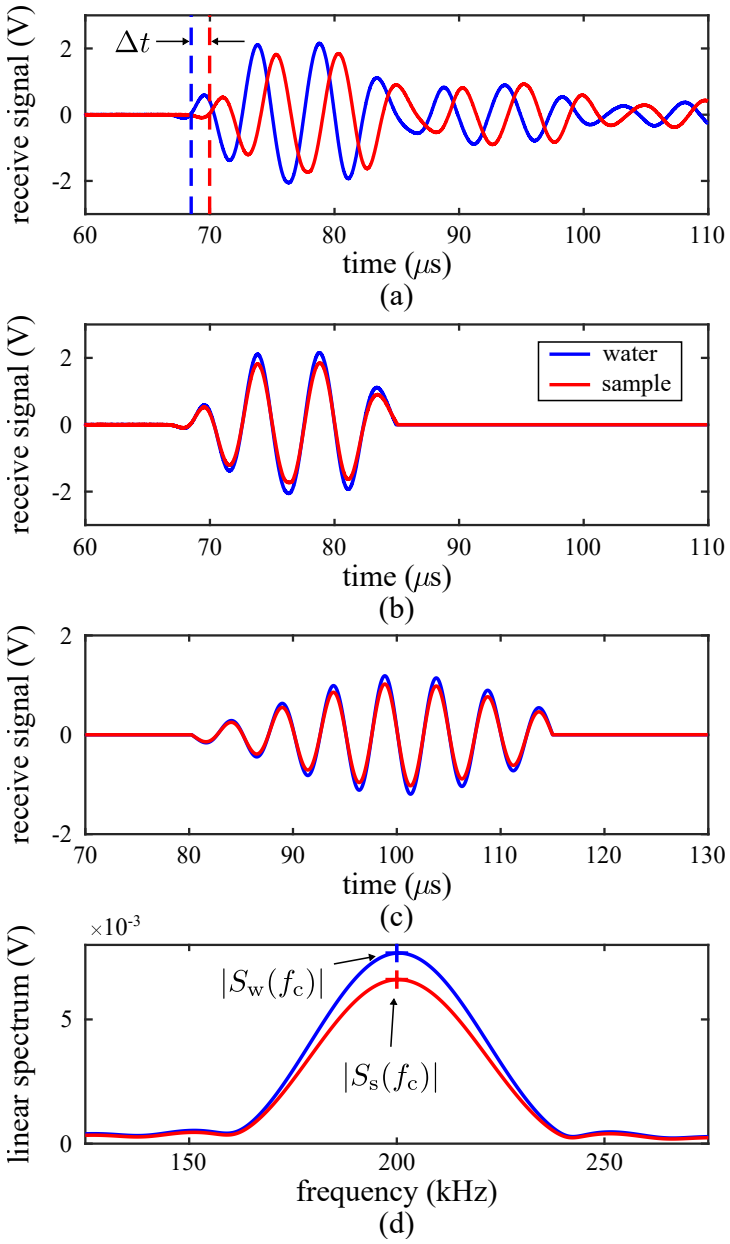

Figure 4.4: Example steps from the signal processing algorithm used to (a) determine the time delay between reference (blue) and sample (red) pulses marked by vertical dashed lines, (b) gate direct arrivals, (c) filter the signals, and (d) evaluate spectral amplitudes to calculate sound speed and attenuation of the sample at 200 kHz.

make sure the correct time delays were determined. At frequencies lower than the resonance of the transducer, the transducer can ring significantly causing a reverberant tail that can reflect from the core walls and contaminate the signal. Example received pulses through the degassed water (blue) and the sample (black) using 500 kHz transducers at a center frequency of 200 kHz are plotted in Figure 4.4 at various steps throughout the algorithm. The phase fronts of the pulses are time aligned and the signals are segmented to minimize multipaths caused by transducer response (Figures 4.4a–b), using automated techniques described in Appendix A. The time delay between the vertical dashed lines represents the time delay between the two pulses, in absence of the inherent system response. The signals are then band-pass filtered with a fourth-order Butterworth filter at cutoff frequencies 10% less than and greater than the center frequency of the pulse, and similarly segmented in Figure 4.4c. Next, the spectral amplitudes of the processed signals are evaluated at the center frequency of the pulse in Figure 4.4d. After the time delay and ratio of spectral amplitudes are evaluated with respect to the nearest two reference signals, a linear interpolation in depth is performed and the sound speed and attenuation are calculated using Equations 4.2–4.3.

4.2.2 Resonance mode

In resonance mode, CARL measures the effective sound speed of the entire cylindrical sample. If there is a water layer above the sample, it is drained. The air-sediment interface and the sample-foam interface at the top

and bottom of the sample, respectively, act approximately as pressure-release boundary conditions. A tonpilz transducer attached to a piston is vertically positioned such that the surface of the piston is in contact with or slightly buried under the air-sample interface, and radially positioned in line with the CARL transducers. To excite only the axisymmetric modes, the piston can be centered between the two CARL transducers, but to excite both axisymmetric and non-axisymmetric modes, the piston should be placed approximately two-thirds of the distance between the two CARL transducers. Logarithmic chirps from 1 kHz to 30 kHz of 0.4-s-duration are continuously transmitted into the sample during the measurement. The repetition of the signal excites standing waves in the sediment cylinder at frequencies within the chirp's bandwidth. During resonance mode, both transducers (the pair of receivers pictured in the right side of Figure 4.1, labeled as (1) and (2)) function as receivers on the outside of the core liner and due to the liner's thin and compliant walls, the standing wave pattern within the sample can be sensed through the walls as a function of depth. Received signals are then conditioned by the pre-amplifier, displayed on the oscilloscope, and acquired on the laptop. The cross-spectrum, G_{TR}, between the transmitted signal and the received signal, and auto-spectrum, G_{TT}, of the transmitted signal, are computed and averaged for each transducer. The transfer function, H, and coherence, C, are then calculated using the relations

$$H(f) = \frac{\overline{G}_{\mathrm{TR}}(f)}{\overline{G}_{\mathrm{TT}}(f)}, \tag{4.4}$$

$$C(f) = \frac{|\overline{G}_{\mathrm{TR}}(f)|}{\overline{G}_{\mathrm{TR}}(f)\overline{G}_{\mathrm{TT}}(\omega)}, \tag{4.5}$$

where the subscripts T and R represent the transmitted signal from the function generator and received signal acquired by the laptop, respectively. The amplitude of the transmitted signal and the gain of the pre-amplifier are adjusted to insure a coherence above 0.95 is achieved at each resonance.

Figure 4.5a displays, in color, the magnitude of the transfer function for CARL transducer (1) as a function vertical position z normalized by the length of the sample L. A value of $z/L = 0$ represents the intersection between the air-sample interface and the middle of contact area made by core logger transducers. The bright areas mark the resonances and associated standing-wave patterns of the sample-filled core liner and allow for the unambiguous identification of the axial mode number at each resonance. The reader may notice that, for each standing-wave pattern shown in Figure 4.5a, the resonance frequency decreases near the anti-nodes. This reduction is attributed to mass loading from the CARL transducers when they contact an area of high pressure amplitude. A finite element model (FEM) demonstrating this effect is presented in Appendix C. To overcome the mass loading, the resonance frequency of the system without the presence of the CARL transducers is estimated by performing a fine-resolution scan in depth, where the scan begins with the contact area completely above the air-sample interface and ends when the air-sample interface intersects the middle of the contact area. The expanded fine-resolution scan (the top plot in Figure 4.5a) shows the measured

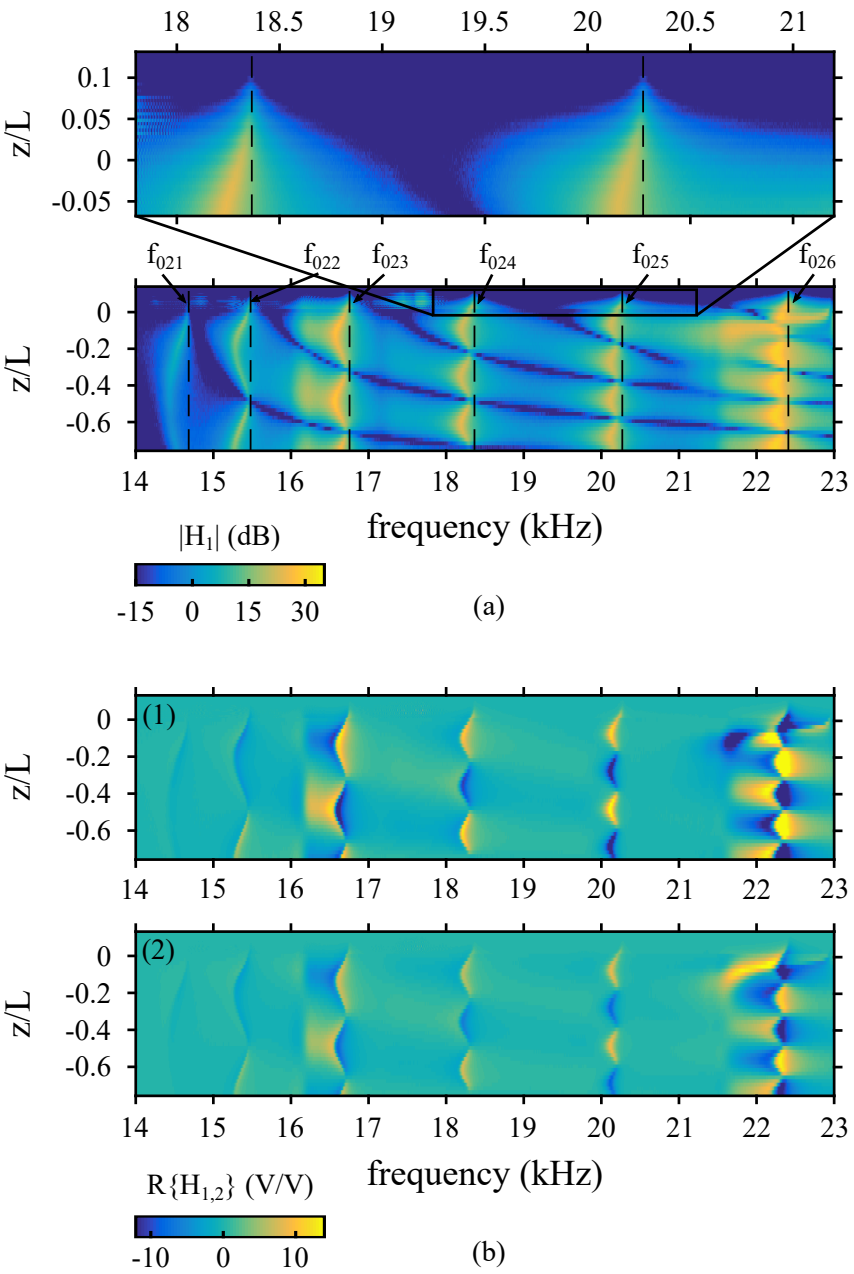

Figure 4.5: (a) Magnitude of the transfer function of the system as a function of depth and frequency as sensed by receiver (1). (b) The real part of the transfer function as sensed by receivers (1) and (2).

resonance frequency approaching an asymptote as the transducer's contact area is raised above the air-sample interface. These frequency asymptotes, marked by vertical dashed lines, are identified as the resonance frequencies of the system.

After each resonance frequency has been identified and paired with a given axial mode, the axial phase speed assuming two pressure release boundary conditions is calculated by

$$C_{nm}(f_{nml}) = f_{nml}\frac{2L}{l}, \tag{4.6}$$

where f_{nml} is the resonance frequency at circumferential mode number n, modal branch number m, and axial mode number l, and L is the axial length of the sample. The circumferential mode number can be identified using Figure 4.5b, which displays the real part of the transfer function between the input signal and signal received by both CARL transducers, as a function of frequency and normalized depth. This depiction identifies each mode as either axisymmetric $n = 0$ (equal phase between each transducer) or non-axisymmetric $n \neq 0$ (opposite phase between each transducer).

The dispersion relations in Appendix B describe a fluid-filled elastic tube waveguide and are used to infer the unknown free-field sound speed of the sample. If axisymmetric modes are sensed, dispersion relations developed by Lafleur and Shields should be used [86]. If non-axisymmetric modes are sensed and if the core liner wall is much smaller than the average of its inner and outer radii, dispersion relations developed by Fuller and Fahy should be

used [96]. Both models require knowledge of the inner radius, wall thickness, density, Young's Modulus, and Poisson's ratio of the elastic tube material, as well as the density and measured phase speed C_{nm} of the sample. In the thin-wall approximation, which is valid here, the fluid-filled elastic shell radius is the average between the inner and outer radii.

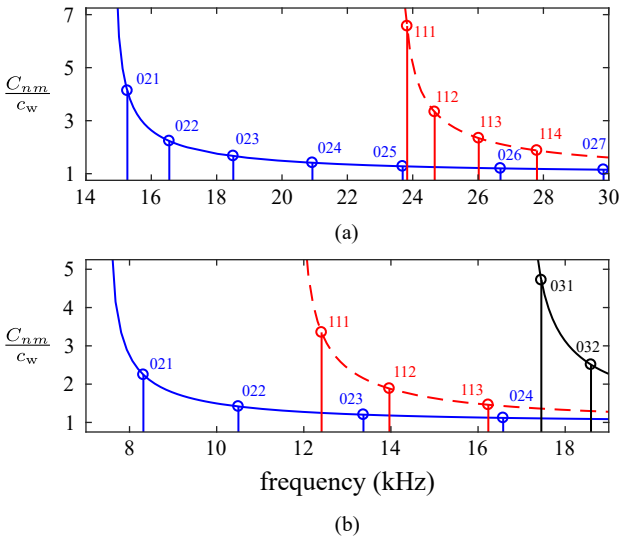

Figure 4.6: The phase speed of the $m = 2$ axisymmetric modes (blue solid lines), $m = 3$ axisymmetric mode (black solid line), and non-axisymmetric modes (red dashed lines) are plotted as a function of frequency for a water-filled 20-cm-long 7.3-cm-diameter core liner (a) and 14.52-cm-diameter core liner (b). The resonance frequencies (circles), labeled with the corresponding mode numbers, are predicted.

All six resonances identified in Figure 4.5 are from the axisymmetric modes of the system, since the non-axisymmetric modes (i.e. $11l$) cut on at a higher frequency. However, if the diameter and length of the liner are comparable in size, the non-axisymmetric modes will occur at a similar frequency band to axisymmetric modes of similar axial mode numbers [38, 97]. For example,

using Equations 4.6 and B.8–B.11 with properties from Table 4.1, Figure 4.6 predicts the various modes found in two 20-cm-long water-filled core liners of the same material with inner diameter $D = 7.3$ cm and $D = 14.52$ cm, denoted in Table 4.1 as D7 and D14. For D14, the additional information provided by CARL is important to minimize the ambiguity associated with pairing a resonance frequency with a given mode of the system. Depending on the aspect ratio and sample material, modes may overlap such as modes 025 and 111 in Figure 4.6a, which should not be used to infer the sample sound speed. As with any enclosure, modal density increases with frequency. To facilitate the identification of modes in the sample, it is best to remain in a frequency regime of low modal density, below which higher-order modes cut on, such as $n > 1$ and $m > 2$. Generally, in order for there to be sufficient transduction by the CARL transducers to sense the standing-wave pattern of the sample, the core liner's wall must be thin and have a compliance on the order of the sample compliance. For these waveguides, the lower-order axisymmetric modes, i.e. $00l$ or $01l$ equivalent to the ET0 and ET1 modes in Lafleur and Shields, are weakly sensed by CARL, and are therefore not used to infer the sound speed of the sample.

4.3 Verification of CARL

Sound speed and attenuation of castor oil (Super Brand Castor Oil #1: Batch 11107010) and a synthetic petroleum-based oil (Nye Lubricants Synthetic Oil 182S) were measured with CARL in pitch-catch mode with the

Table 4.1: Core liner properties used in Figure 4.6.

tube property	symbol	D7[a]	D14[b]
density	ρ_t (kg/m^3)	1190	1190
Poisson's ratio	ν	0.3	0.3
Young's modulus	Y (GPa)	1.31	1.31
inner radius	b (cm)	3.65	7.26
outer radius	d (cm)	3.81	7.58

[a] Used to create Figure 4.6a.
[b] Used to create Figure 4.6b.

three pairs of transducers. Sound speed was measured at a lower frequency in resonance mode using the procedure outlined in Section 4.2 using core liner 7.3D from Table 4.1. Tone bursts with center frequencies at 100 kHz, 200 kHz, 400 kHz, and 600 kHz were sent from the 500 kHz transducer. Tone bursts sent from the 1 MHz transducer had center frequencies of 100 kHz and 200 kHz to 1.8 MHz in 200 kHz intervals. The 7.5 MHz transducer sent tone bursts from 2 MHz to 3.5 MHz in 250 kHz intervals. Due to the equalization performed on the 1 MHz CARL transducer, there was sufficient SNR to measure across the same frequency band of the 500 kHz transducer. An Agilent 33522A function generator and DSO-X 2004A oscilloscope were used for both modes of operation. For the pitch-catch mode, an EMI Model 240L RF power amplifier and a Panametrics ultrasonic pre-amplifier were used. For the resonance mode, a Krohn-Hite 7500 amplifier and a Brüel and Kjær conditioning pre-amplifier were used. Before testing, the samples were degassed in a vacuum chamber at 9.1 kPa of absolute pressure and vibrated by an eccentric mass shaker for four hours. The oil was shaken to accelerate the rise of bubbles in

the viscous fluid. The sample was returned to atmospheric pressure and temperature, and stored over night to allow for the sample temperature to reach equilibrium and for any bubbles to dissolve into solution. CARL pitch-catch measurements were performed at four different depths along the sample. Any variability among depths was incorporated as a 95% confidence interval and combined in quadrature with the uncertainty due to a ± 0.5 mm uncertainty in the width of the sample. Uncertainty was calculated using relations outlined in Appendix D. Acoustic properties were also measured and verified using a standardized pitch-catch measurement at 1 MHz. The oils were maintained at a constant temperature throughout the experiment.

4.3.1 Standard pitch-catch measurement

Two 1 MHz immersion transducers, held a fixed distance apart by the same time-of-flight structure used in Chapter 3, were submerged in degassed fresh water of known temperature. A pulser-receiver in through-transmission mode was used to generate, receive, and pre-amplify the pulses, which were then acquired using an oscilloscope. The water was replaced with degassed castor oil and synthetic oil and the measurements were repeated for each oil.

The received pulses were digitally band-pass filtered with a fourth-order Butterworth at cutoff frequencies 10% less than and greater than the center frequency of the pulse. The time delays Δt associated with the maximum of the cross-correlations between the pulse transmitted through the water and through the oils were calculated. The spectral amplitude ratios between the

pulse transmitted through the water and through the oils were also attained. Sound speed and attenuation were then calculated using Equations 4.2–4.3, where D was the transducer separation distance. Measured sound speed and attenuation values at 1 MHz are shown in Table 4.2.

The attenuation of various types of oils have been shown to have a power-law frequency dependence of the form

$$\alpha = \alpha_0 \left(\frac{f}{10^6} \right)^y, \tag{4.7}$$

where α_0 is the attenuation at 1 MHz in decibels per centimeter per megahertz, f is the frequency in hertz, and y is the power-law exponent [98]. The power law exponent of castor oil at the temperature of the experiment ($T = 22.2^{\circ}$C), was extrapolated using Figure 5b in Reference 98 and was 1.69. Power-law exponent for the synthetic oil was not found in the literature, and instead was inferred by fitting Equation 4.7 to the synthetic oil attenuation measurements performed by CARL. Note that during this fitting process, α_0 was fixed to the measured attenuation from the standard pitch-catch measurements.

Dissipative dispersion required by causality was calculated using Kramers–Krönig relations described by Waters *et al.* [99] and is given by

$$c(f) = \left[\frac{1}{c_0} + \hat{\alpha}_0 \tan\left(\frac{\pi y}{2} \right) \left(|2\pi f|^{y-1} - |2\pi f_0|^{y-1} \right) \right]^{-1}, \tag{4.8}$$

where c_0 is the measured sound speed at frequency $f_0 = 1$ MHz, and $\hat{\alpha}_0$ has units of nepers per meter and is calculated by

$$\hat{\alpha}_0 = \frac{100\alpha_0}{8.686} \left(\frac{10^{-6}}{2\pi} \right)^y. \tag{4.9}$$

Table 4.2: Properties of castor and synthetic oils measured by the standard pitch-catch measurements at 1 MHz.

property	symbol	castor oil	synthetic oil
density[1]	ρ (kg/m^3)	961	840
sound speed ($f = 1$ MHz)	c_0 (m/s)	1519.2	1448.3
attenuation ($f = 1$ MHz)	α_0 (dB/cm/MHz)	0.7578	0.3911
Power-law exponent	y	1.69	1.57

[1] Taken from manufacturer specifications

4.3.2 Comparison with CARL measurements

A comparison between measurements made by CARL and by the standard pitch-catch measurement is shown in Figure 4.7, between 15 kHz and 4 MHz. The minimum frequency was limited to the value of the lowest measured resonance frequency of the sample and the maximum frequency was limited due to low SNR from the high-viscosity oils. To within experimental uncertainty, sound speed and attenuation measurements performed by CARL agreed with the measurements made at 1 MHz by the standard immersion pitch-catch measurement. The measurements made by the 1 MHz CARL transducer from 100 kHz to 600 kHz also overlapped with the measurements made using the 500 kHz CARL transducers.

4.4 Effects of sample rigidity

Shear waves have successfully been measured in marine sediments, though are largely neglected in application, since the shear wave speed and attenuation are an order of magnitude slower and two orders of magnitude

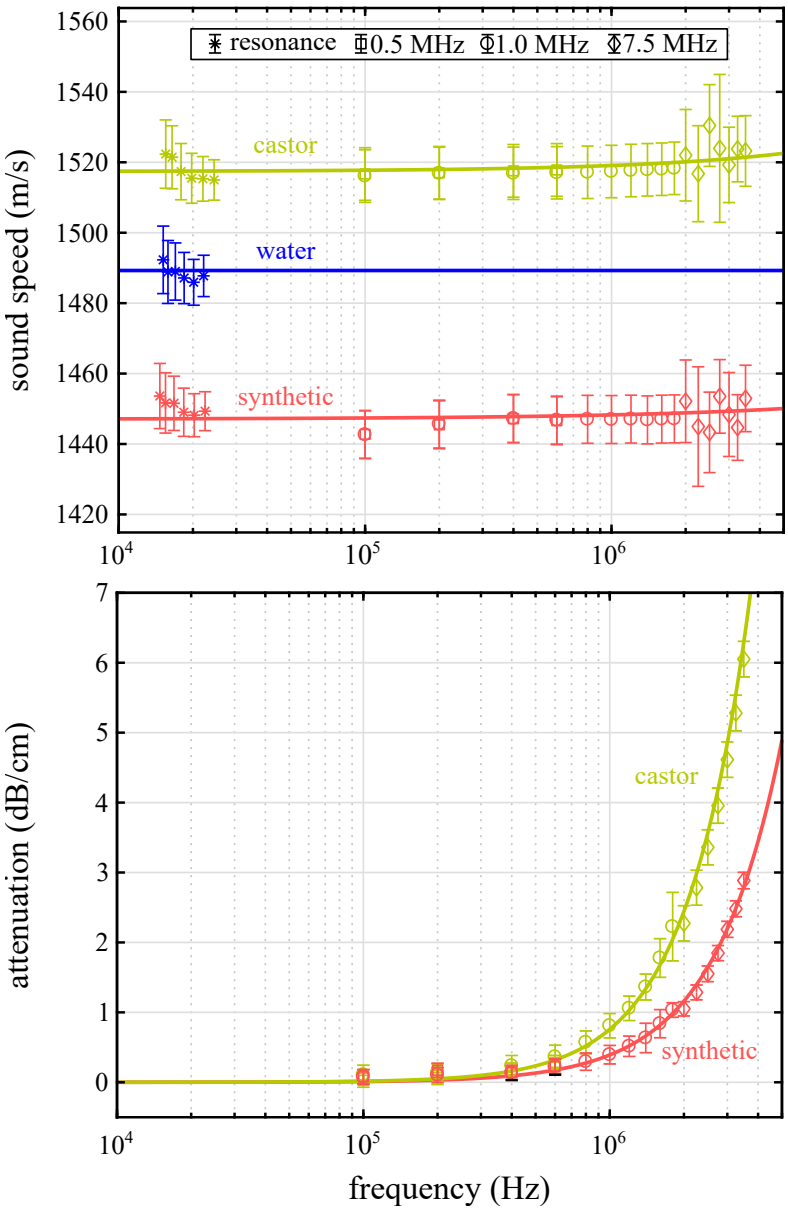

Figure 4.7: Intrinsic sound speed and attenuation as a function of frequency for castor oil (yellow points) and synthetic oil (red points) are plotted in resonance mode (asterisk) and pitch-catch mode using the 0.5 MHz (squares), 1 MHz (circles), and 7.5 MHz (diamonds) CARL transducers. Sound speed and attenuation values measured by a standard pitch-catch method (solid lines) agree with CARL data. Error bars represent a ± 0.5 mm uncertainty in the length and width of the sample.

higher compared with the compressional wave speed and attenuation, respectively [100]. The elastic tube models used to infer the sample sound speed using the resonance technique, described in Section 4.2.2, assumes the sample does not support shear motion. The error associated with this assumption was investigated and quantified by simulating a medium sand as an elastic solid contained within Liners A and B from Table 4.1 using finite elements in COMSOL. A medium sand is defined by the Wentworth scale [10] as a sand with a mean grain size between 0.25 mm and 0.5 mm, and elastic properties were taken from Hamilton *et al.* [101] and displayed in Table 4.3. This data set was chosen due to the uncharacteristically high values of measured shear speed as compared with marine sediment shear speed data compiled in Reference 9. The author is aware that, according to findings presented in Chapter 3, the model for a medium sand should include poroelastic physics. However for the purpose of investigating the effect of shear on the resonance mode, the sediment was modeled as an elastic solid.

Table 4.3: Properties of a medium sand used in FEM simulation.

property	symbol	value
density	ρ (kg/m^3)	2010
compressional-wave velocity	c_p (m/s)	1778.5
compressional-wave attenuation factor	α_p (dB/m/kHz)	0.5
shear-wave velocity	c_s (m/s)	197
shear-wave attenuation factor[1]	α_s (dB/m/kHz)	50

[1] Taken from Reference 9 for a medium sand.

The two-dimensional axisymmetric FEM utilized an eigenvalue solver to find the resonance frequency of the 021 mode of a medium-sand-filled core.

While maintaining the compressional wave speed constant, the shear speed was incrementally varied from 0 m/s to 197 m/s. The resonance frequencies were then used to infer the sound speed of the sample assuming a fluid-filled elastic waveguide model B.1, and the inferred sound speed was compared with the simulated compressional wave speed measured by Hamilton *et al.* [101]. The maximum mesh size of ten elements per shear wavelength was maintained in each simulation. Since eigenvalues converged with such a mesh, the error associated with under-meshing slower waves present in the system, such as the Stoneley wave between elastic solids or Rayleigh waves at the outer edge of the core liner, was determined to be negligible. Attenuation was incorporated by making the compressional and shear speed inputs complex

$$c_{\mathrm{p,s}}^{*} = \left[\frac{1}{c_{\mathrm{p,s}}} - i \frac{\alpha_{\mathrm{p,s}}}{\omega} \right]^{-1}. \tag{4.10}$$

where $\alpha_{\mathrm{p,s}}$ has units of nepers per meter taken from Reference 9 for a medium sand.

The error in the resonance technique associated with neglecting shear is displayed in Figure 4.8 for core liners D7 and D14. The sound speed inference error is reported as the difference between the inferred sound speed and the simulated compressional wave speed in meters per second. The error increases in magnitude quadratically with the shear speed, however it remains within 4 m/s for D7 and within 2 m/s for D14. The fluid assumption under predicts the intrinsic sound speed as a function of shear speed due to an effective decrease in bulk modulus K, since the simulation increases the shear modulus

G while maintaining the p-wave modulus M constant, where $M = K + \frac{4}{3}G$. The coefficients of the second-order polynomials, of the form $k_1 c_s^2 + k_2 c_s + k_3$, fitted to the simulated error in Figure 4.8 are presented in Table 4.4.

Table 4.4: Coefficients from the quadratic polynomial fits to the simulated data in Figure 4.8 using liners D7 and D14.

coefficient	D7 (L=20 cm)	D7 (L=10 cm)	D14 (L=20 cm)
k_1 $(\mathrm{m/s})^{-1}$	-8.066×10^{-5}	-5.441×10^{-5}	-5.174×10^{-5}
k_2	1.171×10^{-4}	8.897×10^{-4}	3.395×10^{-4}
k_3 (m/s)	2.283×10^{-3}	2.612×10^{-2}	1.874×10^{-2}

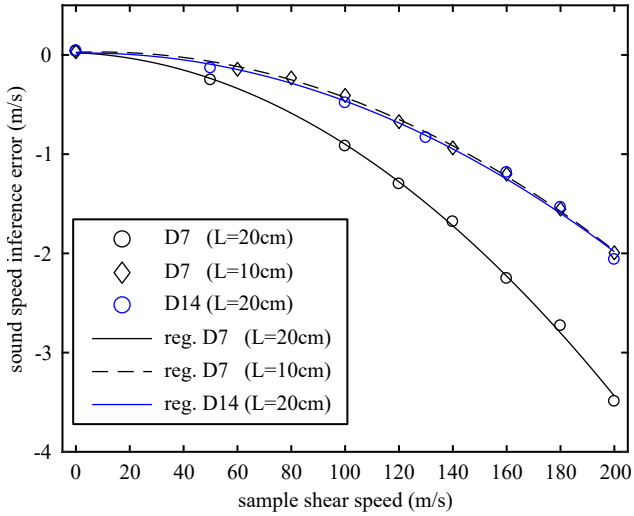

Figure 4.8: Error in the resonance measurement from neglecting shear wave motion in different core liners. Solid and dashed lines are second-order polynomial regressions fit to the simulated data.

The reason for the different rates of error is due to the aspect ratio of the different sediment cylinders. As discussed in Section 4.2.2, the narrower the core liner is with respect to its length, the closer the resonance frequency is to the cutoff frequency. In this region, a small change in resonance frequency

can produce large changes in the waveguide phase speed and therefore in the inferred intrinsic sediment sound speed. This is demonstrated by simulating a 10-cm-long D7 core with approximately the same aspect ratio as that of a 20-cm-long D14 core. Although the resonance frequencies were 1.5 kHz higher for the 10-cm-long core than for the 20-cm-long core, the error as a function of shear speed were approximately equal. The extent of this error was simulated by incrementally increasing the length of the core sample in the simulation, while maintaining the cross-section constant and a shear speed equal to 197 m/s. Error associated with the fluid assumption as a function of core liner aspect ratio is plotted in Figure 4.9. An exponential decay function, of the form $k_1(L/b)^{k_2} + k_3$, was fit to the simulated data, where coefficients are shown in Table 4.5. The value k_3 represents an asymptotic error from measuring a medium sand core with infinite aspect ratio using the resonance technique.

Table 4.5: Coefficients from the exponential decay curve fitted to the simulated data in Figure 4.9 using liner D7.

coefficient	value
k_1 (m/s)	7.848
k_2	-1.073
k_3 (m/s)	-4.738

The error associated with neglecting shear motion within a marine sediment is on the same order as the experimental uncertainty inherent to the resonance measurement outlined in Section D and can therefore be neglected for marine sediments with shear speeds lower than 197 m/s. Note that the

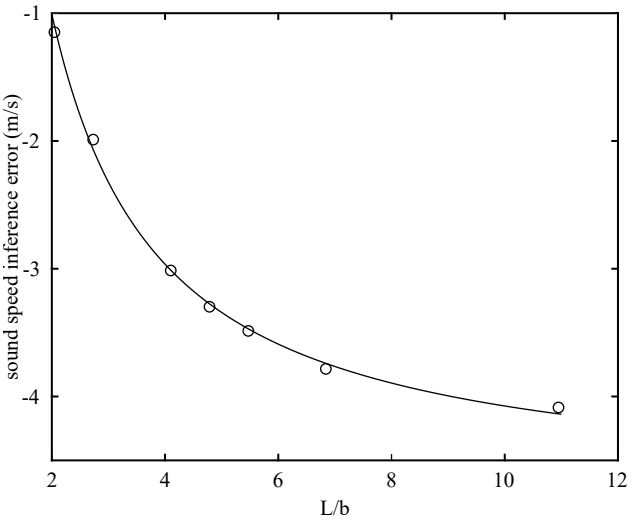

Figure 4.9: Error in the resonance measurement for medium sand as a function of sample aspect ratio for liner D7. The solid line is a nonlinear regression that predicts the asymptotic error for a core with an infinitely large aspect ratio.

majority of marine sediments contain some fraction of finer particles, such as silt and clay, and organic matter. These constituents have been shown to significantly decrease the sediment shear modulus [9] and therefore decrease the error associated with assuming the sediment behaves as a fluid.

4.5 Conclusion

An automated core and resonance logger was constructed from off-the-shelf parts and lab equipment and two oils were tested using its pitch-catch and resonance modes over a frequency band spanning from 15 kHz to 3.5 MHz. CARL sound speed and attenuation measurements agreed with a standard immersion pitch-catch-type measurement at 1 MHz, and agreed with theoretical

values using Kramers–Krönig relations for the entire frequency band of the CARL experiment. Measuring marine sediments with shear speeds less than 197 m/s with the resonance mode were investigated and determined to underestimate intrinsic sound speed values by a maximum of 4.7 m/s, because the technique does not take shear motion into account. Since this underestimation is smaller than the intrinsic uncertainty of the measurement, this effect can be ignored for marine sediments.

CARL has successfully measured the acoustic properties of core samples extracted from four field experiments on the United States Gulf Coast [97, 102, 103], one of which is described in Chapter 5 [104, 105].

Chapter 5

Toward the ultrasonic sensing of organic carbon in seagrass-bearing sediments

5.1 Introduction

Seagrass meadows form the foundation of many shallow water coastal ecosystems across the globe by providing sediment stabilization, nutrient cycling, and production and export of organic carbon (C_{org}). They provide nursery and foraging grounds for fish and an assortment of ecosystem services to resident species, including waterfowl, the endangered dugong, and green turtles. The economic value of global seagrass ecosystems is estimated at $1.9 trillion annually [4]. Recent studies have shown that seagrass meadows are also a globally significant carbon stock, with about twice the average C_{org} storage per hectare (ha) as terrestrial soils [106]. Seagrasses occupy less than 0.2% of the worlds oceans, but contribute to 10% of oceanic C_{org} burial [6]. Protecting the carbon stored in forests is recognized as an important step towards mitigating anthropogenic greenhouse gas emissions. Recognition of the presence of the massive amount of carbon in the coastal ecosystems (mangroves, salt marshes, seagrasses) has led to initiatives to protect these stocks of organic carbon, as well [7, 41]. Seagrasses are among the world's most valuable, and also rapidly disappearing, organic carbon ecosystems [4].

Uncertainties in the estimates of carbon sequestered within seagrass meadows hinder the development of monitoring, recording, and verification frameworks for organic carbon climate mitigation projects. The most recent comprehensive compilation of data, from 946 distinct sites across the world, presented two ranges of estimates for C_{org} stock of global seagrasses: 4.2 to 8.4 Pg C, or 9.8 to 19.8 Pg C, depending on the methodology used for sediment C_{org} estimation [106]. So, for each methodology, there is an uncertainty of a factor of two in these estimates. One major reason for this uncertainty is that the total area of global seagrass coverage is poorly known [107]. Another reason for the uncertainty is that seagrass carbon pools are generally estimated from point-based sediment core sampling, extrapolated statistically across seagrass meadows. Core sampling of under-water seagrass-bearing sediments is a difficult, labor-intensive, and time-consuming process. Subsequent laboratory processing of the sediment samples and the elemental analysis of C_{org} are also time-consuming and expensive. These hurdles limit the number of seagrass sediment cores taken from this ecosystem, and thus contribute to the continuation of uncertainties in the estimates of C_{org} in global seagrass meadows.

Studies have demonstrated the potential for *in situ* measurements of various soil characteristics, such as water content, salinity, temperature, nutrient status etc., using the dielectric, magnetic and acoustic properties of soil [108–111]. But to date, to the author's knowledge, there is no published study on estimating soil carbon using the transmission of acoustic or electro-

magnetic energy through the soil media. The only reliable methods of estimating soil carbon are the laboratory-based methods of combustion or elemental analysis. Development of a reliable method for estimating soil carbon using a portable non-destructive method would be a significant step towards developing in situ methods for easily assessing sediment C_{org} and thus decreasing the uncertainties in the estimates of C_{org} in global seagrass meadows.

Recent studies have demonstrated that there is a well-correlated relationship between the C_{org} stored in seagrass-bearing sediment and various sediment properties such as density, grain size, and porosity [42,43,112]. These findings are consistent with the literature that have shown how fine-grain mineral particles, such as silt and clay, bind to organic material to form complex, porous, low-density sediment fabrics [11] and protect the trapped organic matter (OM) within small pore spaces from microbial decomposition. These same bulk sediment properties have been shown to measurably affect how sound propagates through marine sediment [9,113], but these effects have been mainly attributed to the inorganic mineral constituents that make up marine sediment. Recently, sound propagation in mud has been modeled by considering clay platelets that form "card-house" flocs due to electrostatic van der Waals forces, which suspend granular particles such as silt and sand [32, 114, 115]. How OM affects sediment acoustic properties remains less studied requiring further investigation. The objective of this study is to explore the relationship between C_{org} and sediment acoustic properties, based on a theoretical understanding of sound propagation characteristics in saturated unconsolidated

porous media, with the ultimate goal of developing an acoustical method for estimating C_{org} in seagrass-bearing sediments. To this end, sediment cores from a field experiment in a shallow coastal seagrass meadow were studied. The transmission characteristics of ultrasonic acoustic waves at incremental vertical profiles were measured along with other bulk sediment properties and compared with C_{org}.

5.2 Materials and methods

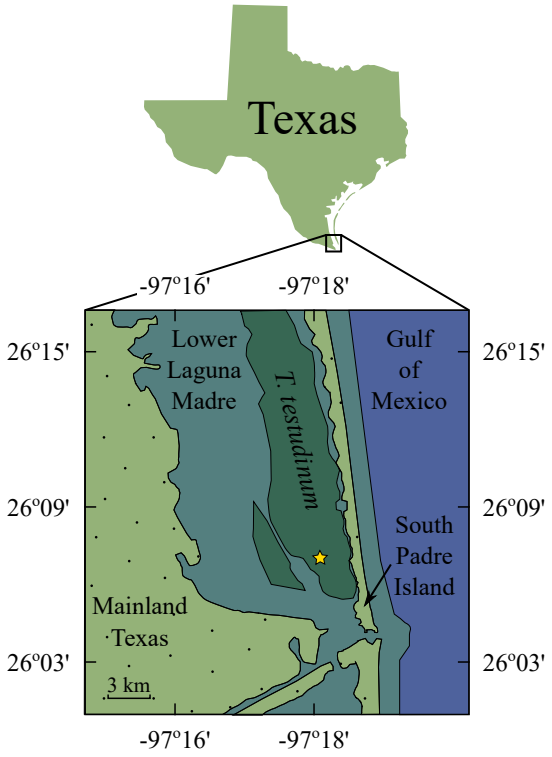

Figure 5.1: The experimental site was located in the Lower Laguna Madre, Texas, USA and marked with a yellow star. Dark green regions represent the *T. testudinum* seagrass meadow.

A field experiment was conducted in the Lower Laguna Madre, which is located on the southern Gulf of Mexico coast of Texas, USA, between the mainland and the barrier South Padre Island. The Lower Laguna Madre is one of five hypersaline coastal ecosystems in the world [116] and contains no river inlets. The site of interest, denoted by the yellow star in Figure 5.1 consisted mainly of *Thalassia testudinum*, also known as turtle grass, and had an average water depth of one meter. This seagrass meadow, shown in dark green, covers roughly 65% of the lagoon and accounts for 75% of seagrass cover along the Texas coast [117].

Five sediment core samples were extracted from the seagrass meadow by driving 7.85-cm-diameter 0.2-cm-wall-thickness polyvinyl chloride (PVC) tubes into the lagoon floor via manual percussion. Once inserted into the sediment, each core was capped at the top and removed slowly with a hand cranked winch while laterally perturbing the core to facilitate extraction. The bottom of the core was capped underwater to avoid air entrapment in the sample. Of the five cores, one was sampled from a nearby bare patch free of seagrass cover located within the meadow. Cores were stored vertically on the boat under shade until they were transferred to the shore-based laboratory for analysis.

5.2.1 Acoustical analysis

Cores were maintained vertical in the laboratory at 24° C and were scanned with the Core And Resonance Logger (CARL) within 24 hours of

extraction [97]. The measurement procedure used in this work is described in Section 4.2.1, with the following exceptions. CARL measured sound speed across the diameter of the core with a pair of Geotek 250-kHz rolling core-logger transducers. Measurements were performed along the length of the core in 2-cm vertical increments downward from the water-sediment interface. At each depth-increment, 20-μs-long tone bursts swept from 100 kHz to 300 kHz in 20 kHz increments were generated by an Agilent 33522A function generator. The signal was amplified by a Krohn-Hite 7500 amplifier, conditioned by a Reson VP2000 pre-amplifier, and acquired and averaged on an Agilent DSO-X 2004A oscilloscope.

For this work, only sound speeds measured at 300 kHz are reported. At lower frequencies near or below the acoustic resonance of the gas volumes encapsulated in the plant tissue or free bubbles in the sediment itself due to anaerobic decomposition [118, 119], sound speed is more sensitive to bubble size and volume fraction of gas than the C_{org} of the sediment [120, 121]. Also, when the sediment particle size is on the order of or larger than the acoustic wavelength, known as the region of multiple scattering, there is large attenuation of acoustic waves and a dramatic drop in sound speed [29, 65, 122] independent of the C_{org} sequestered in the sediment. The ratio of mean grain diameter to acoustic wavelength remained within 0.002 to 0.034 for this study. Encapsulated bubbles with resonances higher than 300 kHz, or coarser sediment fragments could result in unaccounted experimental uncertainty. In the aforementioned cases, a bi-modal cross-correlation between the received signal

through the reference material and through the sample was identified. To minimize the unaccounted experimental uncertainty, the time aligned signals were manually inspected to insure the data analysis algorithm picked the correct cross-correlation peak corresponding with the earlier direct arrival through the sediment phase rather than the slower scattered arrival.

In Appendix E, an X-ray computed tomography scan of a segrass-bearing sediment core, extracted from the same seagrass meadow during a subsequent experiment, is provided to show the larger shell hash particles and the gas encapsulated in the seagrass tissue and sediment. Also, a bubbly sediment model was fit to sound speed data as a function of frequency taken at two depths from a seagrass-bearing core and a bare core. It is then shown that the bubbly sediment model converges with the bubble-free sediment model at 300 kHz.

5.2.2 Sediment properties

After the acoustic measurements were completed, the cores were vertically preserved in a freezer and sliced in the same 2-centimeter increments scanned by CARL. By freezing the cores, samples confined within the PVC core liner could be sliced cleanly using a bandsaw without significantly altering the sediment structure. The water-sediment interface was marked before freezing to account for any potential expansion, and only a negligible amount of expansion was observed. The dimensions and weight of each sediment slice were recorded to calculate the frozen bulk density as the frozen weight divided

by the volume it occupied. The slices were placed in an oven at 65° C for 3–4 days until their dry weight reached an equilibrium value that was recorded to determine dry bulk density. Porosity was then calculated using

$$\beta = \frac{m_{\text{frozen}} - m_{\text{dry}}}{\rho_{\text{ice}} V}, \tag{5.1}$$

where m_{frozen} and m_{dry} are the frozen and dried mass of the slice, respectively, ρ_{ice} is the density of ice, and V is the volume of the slice. Frozen density values were corrected to the ambient temperature of the laboratory where the cores were acoustically logged by

$$\rho_{\text{wet}} = \frac{m_{\text{dry}} + \beta V \rho_{\text{water}}}{V}, \tag{5.2}$$

where ρ_{wet} is the corrected sediment wet bulk density, and ρ_{water} is the water density at 24° C. Depending upon the calculated porosity, corrected wet density values were 1% to 6% greater than the frozen density values.

Since the sound speed of a material is a function of both its density and stiffness, the primary wave (p-wave) modulus was reported in order to remove the interdependence sound speed has with density. The p-wave modulus (M) is the dynamic (acoustic) and frequency-dependent stiffness sensed by a compressional wave [123] and is defined as

$$M = \rho_{\text{wet}} c_{\text{sed}}^2, \tag{5.3}$$

where c_{sed} is the sound speed of the sediment. The p-wave modulus can also be expressed in terms of the bulk modulus K and shear modulus G, and is

$M = K + \frac{4}{3}G$. However, since the shear wave speed was not measured with CARL, it was not possible to isolated K and G, and they were hence combined into the same effective stiffness variable. Due to the fluid-like consistency of the organic-rich fine-grained sediments reported in this study, the p-wave modulus is approximately equal to the bulk modulus because values of G are orders of magnitude smaller than K. In addition, due to the high content of fine-grains present in seagrass-bearing sediments, the reduction in effective density from poroelastic effects discussed in Chapter 3 is not accounted for in determining M, and is assumed to be small. The effective density referred to by the EDFM requires more investigation to adequately quantify and account for poroelastic effects in sediments with a wide particle size distribution.

Sediment particle-size distribution was determined using a laser-diffraction particle-size analyzer for all particles smaller than 500 μm and a dry sieving technique was used for larger particles. In preparation for particle size analysis, a 10-g subsample of the dried sediment was wet-sieved through a 500 μm sieve. Wet sieving was performed to minimize fine particles adhering to larger particles to help control measurement bias. Both coarse and fine particles were dried in the same aforementioned manner. Dried coarse particles mainly consisting of plant litter, shell hash, and other carbonate fragments, were vibrated and sorted through a stack of 710, 1000, 2000, and 2800 μm sieves. Dried fine particles were gently homogenized with a mortar and pestle and sprinkled into a Malvern Hydro LV, where they were dispersed for 4 minutes with an ultrasonic in-line sonicator set to maximum power to insure adequate

particle dispersion and analyzed using a Malvern Mastersizer 3000 [124]. Cumulative distribution functions (CDFs) from both coarse and fine particles were combined proportionally to their recorded dry mass and used to compute grain size statistics [22]. Mud content (MC) is defined explicitly as the sum of both clay and silt-sized particles according to the Wentworth Scale [10], and was computed from the CDFs evaluated at 62.5 μm and evaluated for every sample slice. Sand content was similarly computed and defined as any particle larger than 62.5 μm and smaller than 2 mm. Coarse particles larger than 2 mm mainly consisted of shell hash and carbonate fragments.

5.2.3 Organic carbon content

The remaining unsorted dried sample was then homogenized gently with a mortar and pestle and passed through a 63 μm sieve. A 0.5-g subsample from the fines were placed on a ceramic crucible and into a Thermo Scientific Muffle Furnace heated to 500° C for 4 hours. This process volatilized all the C_{org} and other organic materials in the sample. Then 5 mg of the ash containing the inorganic carbon (C_{inorg}) among other inorganic materials was placed into a PerkinElmer 2400 CHNS/O Series II Elemental Analyzer. The C_{inorg} was determined by taking the post-muffle to pre-muffle weight ratio and multiplying it by the percent carbon content of the ash. The total percent carbon content of the sample was recorded by placing 5 mg of the fines directly into the elemental analyzer. The C_{org} was then calculated by subtracting the C_{inorg} from the total carbon content [119]. The C_{org} values are thus estimated

from the particles less than 63 μm in size and presented as a percentage of the dry mass of each 2-cm core section.

5.3 Results

A large difference in all measured sediment parameters was observed between the seagrass-bearing sediment cores and the bare-patch sediment cores. Figure 5.2 shows sediment composition separated into grain size (left) and C_{org} (right). Compared to the bare-patch sediment core, the seagrass-bearing sediment cores contained more C_{org}, more coarse particles such as plant litter, shell hash, and carbonate fragments, along with greater MC. These constituents resulted in sediment with higher porosity, lower density and lower stiffness.

In addition, a large contrast in segrass-bearing sediment properties was observed as a function of depth. Near the water-sediment interface, MC as much as 70% and C_{org} values as high as 6% were found whereas 45 cm below the water-sediment interface, 20% MC was reported with C_{org} values as low as 0.5% by dry mass. Sediment properties acquired in both seagrass and bare patches were consistent with literature values reported in this site [125].

The relationship between sediment p-wave modulus and density was used to identify two regimes plotted in Figure 5.3. Sediment with lower stiffness and density values followed a line of constant sound speed equal to that of the seawater, until the sediment stiffness surpassed a threshold of 4.2 GPa. This threshold was used to distinguish between the isovelocity regime and the stiffness-dominated regime. The depth at which this threshold occurred

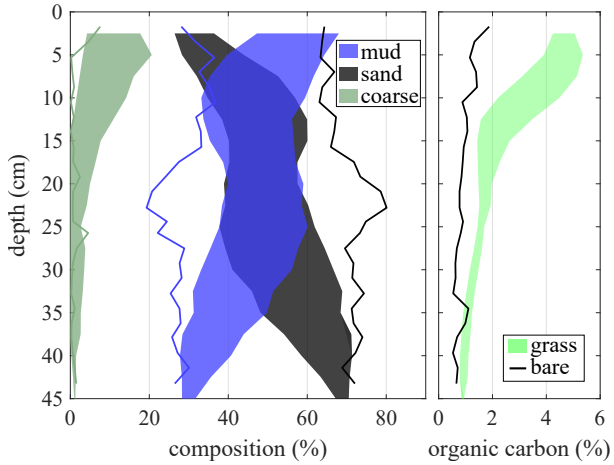

Figure 5.2: Sediment composition (left) and organic carbon (right) depth profiles for the seagrass cores (shaded regions) and for the bare patch core (lines). Shaded regions represent a standard deviation on either side of the mean depth-averaged in 5-centimeter bins. Since only one bare sediment core was collected, no spread in the data was reported.

varied between 10 cm to 20 cm into the sediment. For the remainder of the paper, sediment property comparisons will be performed within these respective regimes.

Pearson correlation coefficients (r-values) were determined and tabulated for the following sediment properties: mud content (MC), percent organic carbon (C_{org}), dry bulk density (ρ_{dry}), porosity (β), and sediment p-wave modulus (M) (Table 5.1). Since MC, dry bulk density, and porosity have been shown to be good predictors of C_{org} [43], they were chosen as candidate parameters to compare with p-wave modulus of the sediment. Two r-values were found between each parameter. The top values within each cell correspond with the data in the isovelocity regime, while the bottom values correspond

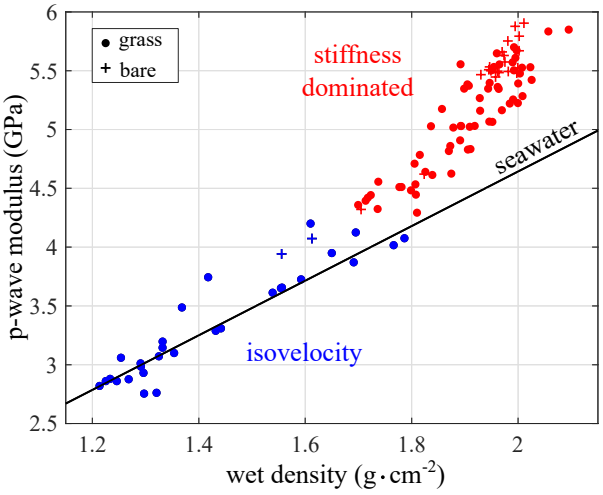

Figure 5.3: Stiffness-mass relationship identifies two regimes of interest: a regime with equal sound speed to that of the seawater (isovelocity) and a stiffness-dominated regime. Data taken from seagrass and bare cores are represented as dots and crosses, respectively.

with the data in the stiffness-dominated regime. Off-diagonal elements contain a number of asterisks pertaining to a P-value range defined as the probability of attaining at least the corresponding r-value under the null hypothesis.

In the stiffness-dominated regime, all sediment parameters, particularly p-wave modulus, correlated well to C_{org} with P-values less than 0.001. Porosity and MC were positively correlated with C_{org}, while dry density and p-wave modulus were negatively correlated with C_{org}. In this regime, p-wave modulus correlated well with all sediment properties except MC. In the isovelocity regime, there was an overall higher correlation of C_{org} to all sediment properties with the exception of MC, and like in the stiffness-dominated regime, C_{org} correlated best with p-wave modulus. The only sediment properties that

Table 5.1: Top right triangle: Pearson correlation coefficients (r-values) between variables determined from all seagrass cores with in isovelocity (top) and stiffness-dominated (bottom) regimes. Bottom left triangle: Cross-diagonal elements represent P-values for corresponding r-values.

	MC (%)	C_{org} (%)	ρ_{dry} (g·cm^{-2})	β (%)	M (GPa)
		0.39	-0.52	0.54	-0.46
MC (%)		0.74	-0.55	0.44	-0.55
	*		-0.93	0.93	-0.94
C_{org} (%)	**		-0.84	0.78	-0.88
	*	**		-0.997	0.94
ρ_{dry} (g·cm^{-2})	**	**		-0.90	0.92
	*	**	**		-0.95
β (%)	**	**	**		-0.81
	*	**	**	**	
M (GPa)	**	**	**	**	

$^{**}P < 0.001$, $^{*}P < 0.05$

correlated well with MC was C_{org} in the stiffness-dominated regime. Though all correlations with MC in the isovelocity regime were statistically significant, corresponding P-values were consistently greater than 0.001.

In both regimes, C_{org} correlated best with p-wave modulus compared with other sediment properties in Table 5.1. A line-of-best-fit was plotted showing the trend of p-wave modulus as a function of percent C_{org} for each regimes (Figure 5.4). Empirical regressions were performed only on the seagrass-bearing sediment cores (denoted by dots) although data points from the bare patch sediment core are also shown in the figure as crosses. Equations for empirical regressions displayed in Figure 5.4 are

$$M = -0.986 C_{org} + 6.361 \tag{5.4}$$

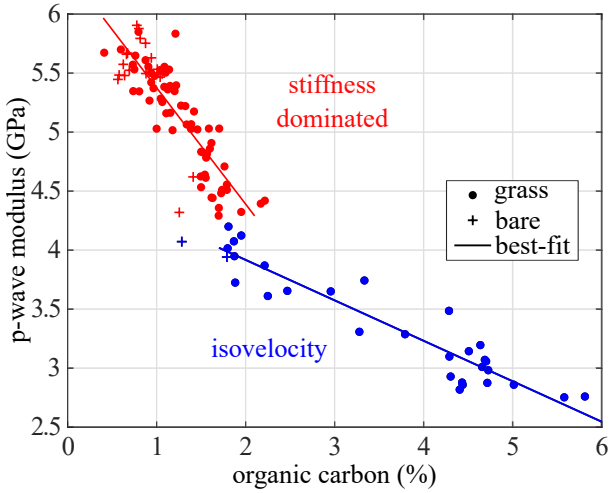

Figure 5.4: P-wave modulus shows a strong correlation with C_{org} in both isovelocity and stiffness-dominated regimes. Only data taken from seagrass cores (dots) were used to perform empirical fits.

and

$$M = -0.343C_{\text{org}} + 4.603 \tag{5.5}$$

for the stiffness-dominated and isovelocity regimes, respectively, where M has units of gigapascals. The regimes identified in Figure 5.3 are similarly separated into two unique linear regimes when comparing sediment stiffness with C_{org}. The transition between the two regimes occurred at a C_{org} value of roughly 1.8% and was also identified by a 0.5 GPa reduction in p-wave modulus. This reduction in acoustic stiffness coincided with a 10% increase in porosity plotted in Figure 5.5. Unlike in Figure 5.4, where the rate at which p-wave modulus decreased with C_{org} differed between regimes, the rate at which porosity increased with C_{org} remained relatively constant, though the regimes were distinguishable by the 10% shift discussed at the transition.

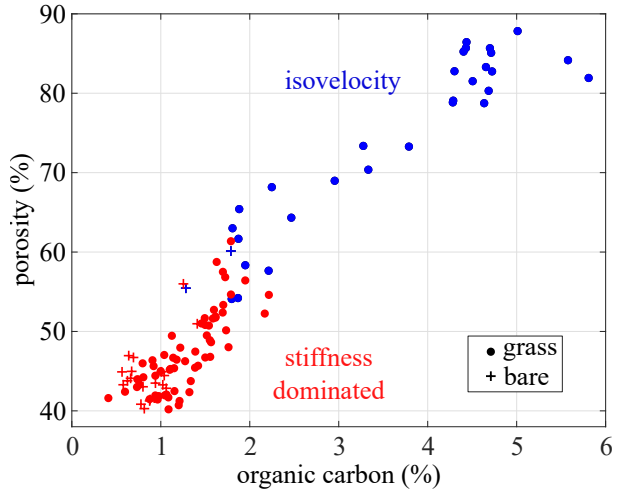

Figure 5.5: Data shows pronounced porosity increase near the transition between regimes.

There was a distinct positive linear relationship between MC and C_{org} in the stiffness-dominated regime that spanned the entire range of MC measured in this data set (Figure 7). When transitioning into the isovelocity regime, the data became scattered spanning a similar range of MC seen in the stiffness-dominated regime.

5.4 Discussion

For the chosen experimental site, these data suggest that, compared with dry bulk density, p-wave modulus can serve as an equally good predictor of C_{org} in the isovelocity regime and a slightly better predictor of C_{org} in the stiffness-dominated regime. In other words, the presence C_{org} affects both the acoustic stiffness and the density of sediment in different ways depending on

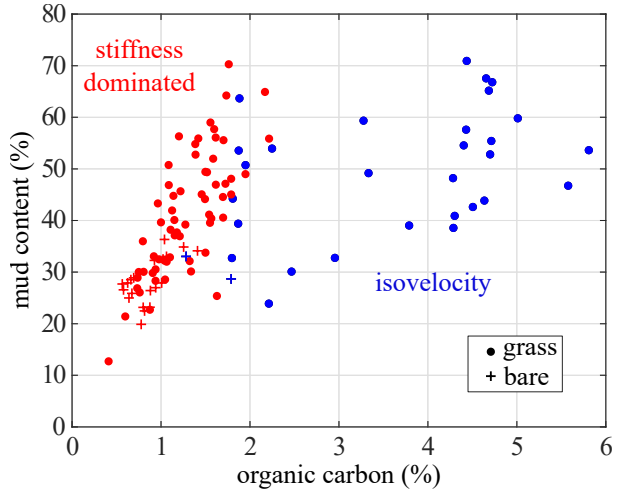

Figure 5.6: Mud content shows strong correlation with C_{org} only in the stiffness-dominated regime.

the regime. To this end, a representative physical model is desired to better understand the mechanisms responsible for the changes in sediment properties caused by the presence of C_{org}.

The purpose of this work is to better understand the relationship between independent variables that constitute the sediment, such as MC and C_{org}, and dependent variables, such as p-wave modulus, dry bulk density, and porosity. The r-values from Table 5.1 show an expected interdependence among dependent variables, since the minerals are denser and stiffer than water or the OM. For example, to first order, the more porous the sediment, the fewer minerals are contained within a unit volume, and the less dense and less stiff the sediment becomes. However, it is the sediment constituents that ultimately control porosity. Although p-wave modulus correlates well with dry bulk density and porosity, p-wave modulus is also ultimately controlled

by the sediment constituents. Based on the results of this study, observations reported in the sedimentology literature, and established models for sound propagation in granular media, two separate physical mechanisms are postulated to explain the dependence between p-wave modulus and C_{org} in the stiffness-dominated and isovelocity regimes, respectively.

Within the stiffness-dominated regime, as C_{org} increases, small deposits of OM begin to absorb onto the surfaces of the clay platelets and grains, creating compliant layers between the otherwise stiffer frame comprised of grain-to-grain contacts [126, 127], thereby reducing the acoustic stiffness of the sediment. In natural sediment, Ransom *et al.* observed patches of OM adsorbed onto mineral surfaces with transmission electron microscopy (TEM) [128], though how this phenomenon can affect bulk sediment properties was not addressed by his work. Sound propagation in consolidated granular sediments have been successfully modeled as slip-stick processes between neighboring grain micro-asperities separated by very thin interstitial seawater [129]. The contact area referred to in this framework is precisely where organic matter is most protected from decomposition [127] and can therefore affect bulk wave propagation.

Once a threshold is reached over which mineral surfaces and pores spaces become saturated with OM, the mineral constituents push apart, approaching an organic-rich suspension, where the sediment begins to behave more like a low-density water-like organic slurry or sludge comprised of digestates such as lignin and humic acid, represented by the isovelocity regime. This

saturation point is posed to be equivalent to the C_{org} "refractory background level" described in [130,131] and related to the mineral surface area [132]. However, since mineral surface area was not measured, the data presented here can not directly compare the saturation point observed with that of the literature, though many experimental sites included in Mayer [132] showed values of C_{org} consistent with that of the transition region of this study. Organic matter has also been categorized into low and high-density states [133], which depend on origin of the OM and whether it is adsorbed. Extending these findings to the results of this study, it is believed that the more stable high-density OM adsorbed onto mineral surfaces accounted for the majority of the C_{org} found in the stiffness-dominated regime, while in the isovelocity regime, the OM can only remain in a low-density state since the mineral surfaces have theoretically become saturated. Mayer claims that adsorption of C_{org} onto mineral surfaces is the dominated mechanism that drives long-term C_{org} sequestration in marine sediment [133]. Without the presence of the above- and below-seagrass biomass to help stabilize the sediment, this organic-rich sludge described by the isovelocity regime would likely erode more easily, explaining why seagrass-bearing sediments can sequester above the refractory background level. More investigation is required to assess the validity of this hypothesis and address if or where these two regimes exists across different sediment types or different seagrass species. However, this phase change represented by the organic-rich isovelocity regime found within the top 20 cm of sediment, appears to be less dependent upon sediment type and could potentially be applied to isovelocity

regimes located in different seagrass meadows and sediments.

The MC of sediment has been shown to increase sediment porosity, which in turn decreases sediment density and stiffness [9, 113], and could be another factor attributing to the decrease in stiffness independent of C_{org}. Although a negative trend between MC and C_{org} was observed, Pearson correlation coefficients suggest that within the *T. testudinum* seagrass meadow studied, it was the organic material that played the dominated role in controlling sediment density and stiffness in both regimes. The presence of fine-grained minerals, however is closely related to C_{org} content [134–136] due to the increase in mineral surface area [132]. In fact, Curry *et al.* directly observed two mechanisms that preserve OM from digestion in fine-grained sediments using TEM: OM adsorption onto mineral surfaces and encapsulation within small pores of the sediment microfabric that were inaccessible to enzymes used in the study [34]. These observations in the microscale are consistent with data reported in Figure 5.6 within the stiffness-dominated regime. However, once the saturation point is surpassed in the isovelocity regime, OM is no longer protected from microbial attack by the fine-grained minerals and becomes weakly correlated with MC. Mayer *et al.* showed that low-density organic particles cannot account for grain-size dependence of bulk C_{org} in a continental shelf region [133]. The weak correlation to MC in the isovelocity regime is further evidence that much of the bulk C_{org} in the upper carbon-rich layer is low-density organic material. Since sediments with higher MC have the capacity to store more C_{org} and yield lower sediment stiffness, these correlations pro-

vide promise that sediment stiffness could be used to sense C_{org} acoustically for sediment with a wider range of MC than was found at this experimental site.

5.5 Conclusion

Sediment-sequestered organic carbon ranging from 0.5% to 6% by dry mass of the *T. testudinum* seagrass meadow in the Lower Laguna Madre correlated best with sediment p-wave modulus compared to other sediment properties such as MC and density. Since the Lower Laguna Madre is predominately comprised of fine sand with a high p-wave modulus, the reduction in stiffness seen when the seagrass meadow incorporates its organic-rich sludge in the sediment provided a measurable contrast that can be detected via acoustical means. While seagrasses more commonly grow in sandy sediments, seagrasses that grow in silt or clay deposits with MC greater than 70% may provide a less detectable contrast in p-wave modulus with the background sediment due to the presence of C_{org}. However, the background sediments with high MC could still yield high C_{org} due to an inherently larger refractory background level. While the methods reported here are *ex situ*, the strong correlations in both stiffness and density demonstrated in this study show promise toward the development of an acoustic *in situ* organic carbon sensor that could be applied to sample large areas minimizing the need to spatially extrapolate, as well as facilitating studies on spatiotemporal changes in organic carbon stocks using acoustic means.

Chapter 6

Conclusion

The acoustic behavior of marine sediments has been studied extensively, and yet optimization of modern sonar systems and underwater acoustic remote sensing systems still requires an improved understanding. This is particularly true for fine-grained sediments, and for cases where significant organic matter is present. Three separate but related sediment acoustics studies were conducted and described in this dissertation.

The first study illustrated one way that the acoustic properties of the sediment can be dependent on the time-varying changes of the overlying water (bottom water). In general, the acoustic effects of variability in the water column are known and well understood with regard to propagation in the water column, but this variability is typically assumed not to alter the acoustic reflectivity from the ocean bottom. In a laboratory experiment conducted at high angles of incidence, temporal variations in bottom water salinity caused a change in bottom loss up to 15 dB and induced 180-degree phase shifts in the reflected signal from two kaolinite-based clays. Then, the diffusion coefficients of the clays were inferred from the experiment. The diffusion in the card-packed clay was an order of magnitude slower than the card-house clay.

This difference was expected and was attributed to the more constrictive card-packed microstructure [50]. Using these inferred diffusion coefficients, bottom loss was modeled at lower frequencies, where the following criteria were developed: given the time scale of a salinity or temperature fluctuation of the bottom water and the diffusion coefficient of the sediment, a characteristic frequency can be determined. Below this frequency, bottom water fluctuations can cause significant variability in bottom loss. In this case, the pore water salinity or temperature can be more accurately approximated as the time-averaged history of the bottom water salinity or temperature. However, if the operating frequency is higher than the characteristic frequency, such fluctuations can be ignored, since the pore water has the same properties as the bottom water. Quantifying the variability in bottom loss is of interest to any shallow water sound propagation application where the majority of interactions with the sediment occur at high angles of incidence, such as shallow water sonar, port protection, and fishery monitoring.

The second study was conducted to investigate the importance of including poroelastic physics when modeling granular sediment as a fluid in a geoacoustic inference scenario. This was achieved by using an idealized water-saturated granular sediment cylinder, suspended in a water-filled glass tube waveguide with pressure release boundary conditions. The resonance frequencies of the system were measured and the phase speed in the waveguide was calculated. Finite element simulations of the resonance measurement were conducted to infer the sediment sound speed. In each simulation, the sedi-

ment domain was modeled by different sediment acoustics fluid models. The only sediment acoustics model that produced inferred sound speeds consistent with an independent set of high-frequency direct measurements of the water-saturated glass beads was one that accounted for poroelastic effects in the sediment.

In preparation for the third study, the Core and Resonance Logger (CARL) was developed, which combined the low-frequency resonance technique with the high-frequency pitch-catch pulse techniques to span an extended frequency range of nearly four orders of magnitude. The apparatus was comprised of inexpensive off-the-shelf equipment, financially accessible to scientists. A set of verification measurements were performed using two oils with power-law attenuation frequency dependence. Since the resonance method assumes the sediment behaves as a fluid, finite-element modeling was employed to quantify the error associated with a sample of finite shear modulus within the range of most unconsolidated marine sediments. The error was within the intrinsic error of the measurement and was ignored. CARL has successfully measured over 60 cores taken during field experiments conducted in the Gulf of Mexico, including those presented in this document within a seagrass meadow in South Padre Island, TX.

Perhaps the most novel result uncovered and reported here is a strong correlation between the primary-wave (p-wave) modulus and the organic carbon content in seagrass-bearing sediment. Interstitial organic carbon is a constituent that has been completely ignored in sediment acoustics modeling

efforts, and yet is ubiquitous in all marine sediment, particularly in seagrass-bearing sediments. Further, this organic carbon correlation is stronger than the correlation between p-wave modulus and mud content. The correlations in bulk material properties combined with observations made in the fine-grained sedimentology literature [126, 127, 132, 133] inspired a hypothesis that could explain the relationship between p-wave modulus and organic carbon. The hypothesis can be divided into a stiffness-dominated regime of low organic carbon and an isovelocity regime of high organic carbon. In the stiffness-dominated regime, deposits of organic material adsorb onto the surfaces of clay platelets and grains, creating compliant layers among grain contacts, which effectively reduce the overall stiffness of the sediment. Once the mineral surfaces and pore spaces become saturated with organics, the minerals begin to separate and form an organic-rich suspension in the isovelocity regime.

These experimental demonstrations, however, all require more study *in situ* across different sediment types and geographical locations to further address their implication for underwater acoustic applications. Limitations of the findings reported in this document are presented along with recommendations to better address such limitations in future work.

6.1 Limitations and recommendations

A limitation of the work accounting for salt diffusion into fine-grained sediments (Chapter 2) is that the laboratory measurements and simulations were performed with drastic salinity fluctuations to demonstrate the upper

bound in associated bottom loss variability in the ocean. Although fluctuations can occur in the ocean on this order in riverine and estuarine environments, fluctuations farther out on the continental shelf are less extreme. To address this in any given environment, the maximum change in bottom loss can be calculated by first assuming there is no diffusion into the sediment. If the change in bottom loss is negligible for the given application, the fluctuation can be ignored at any frequency. Provided the coefficient of thermal and salt diffusivity in the sediment are known, the framework developed here can used to determine the acoustic effects of any bottom water fluctuation in the ocean. However, more investigation is required to adequately predict the diffusion coefficient of salt in marine sediments with different mineral content, microstructure, and particle size distributions.

A sound speed over-prediction was observed when neglecting poroelastic physics during a geoacoustic inference process performed in a laboratory experiment with water-saturated mono-disperse glass beads (Chapter 3). This effect has not yet been demonstrated with natural sandy sediments across different grain size distributions. However, in theory, the extent of this overestimation would diminish by either reducing the operating frequency or performing the inference with lower permeability, i.e. finer-grained, sediments. In addition, the layered waveguide presented here may be more sensitive to this effect than compared with a typical shallow water ocean waveguide. A geoacoustic inference in a more realistically scaled acoustic propagation experiment is recommended to better quantify the effect of neglecting poroelasticity

in the real world.

A correlation was found in sediment collected beneath a seagrass meadow, between p-wave modulus and organic carbon (Chapter 5). The correlation is based on 113 measurements taken from only one seagrass meadow. More work is required to assess if this correlation can be applied uniformly to other seagrass meadows with different sediment types, as well as non-seagrass-bearing sediment. If the correlation among sites are different, a site-specific calibration must be performed.

Findings from this work have demonstrated significant ramifications when accounting for effects that have historically been neglected in the field of underwater acoustics. In addition, the author hopes this work inspires a new subset of sediment acoustics relating to organic biogeochemical processes that may help bridge the gap in knowledge between the microfabric and bulk sediment properties [11]. These findings are not only relevant to the field of underwater acoustics, but extend into applications within climate science toward developing new methods to more rapidly monitor the health of valuable marine carbon sinks, which are considered vital in mitigating climate change.

Appendices

Appendix A

Pitch-catch algorithm

This is the signal processing algorithm used to find the time delay and ratio of spectral amplitudes at the center frequency of the received tone bursts through the reference and sample during a CARL measurement.

DC offsets in the signals are removed, and any cross-talk observed in the received signals is removed. Next, the absolute value of the signals are temporarily normalized by their maximum value, and the time at which the sample signal surpasses a threshold twice that of the noise is marked for both signals (Figure 4.4a). The normalization improves the likelihood that the time determined by the threshold is at the same phase front in both the reference and sample signal. A cross correlation between the reference and sample signal is also performed to align the phase fronts. The peak of the cross correlation with the time delay nearest to that found by the threshold processing is chosen as the initial time delay between reference and sample signal Δt_1, and the signals are time aligned. This two-step time alignment scheme is useful when the sample contains gas and the correlator is more likely to pick earlier arrival through the sediment pertaining to the threshold value.

Next, the multipaths present in the signal from the transducer ring-

down are zeroed. To automate this process, the envelope of reference signal squared is calculated by performing the absolute value of the hilbert transform of the squared pulse. Near the tail of the pulse, the time at which the value of the envelope becomes less than 10 percent of its maximum is found. Subsequently, the nearest zero crossing is found and all signal after this point is zeroed. The nearest zero crossing in the aligned sample signal is then found and all signal received after this zero crossing is similarly zeroed (Figure 4.4b).

The reference and sample signals are then down-sampled to four points per wavelength and digitally band-pass filtered at cutoff frequencies 10% above and below the center frequency of the pulse with a fourth-order Butterworth filter. The filtered down-sampled signal is then resampled back to its original sampling rate. After band-pass filtering, an additional time delay Δt_2 is found using another cross correlation, the signals are time aligned further and similarly segmented (Figure 4.4c). The total time delay Δt between reference and sample signals used to calculate the sample sound speed in Equation 4.2 is $\Delta t = \Delta t_1 + \Delta t_2$. In preparation for preforming the Fourier transform, the pulses are downsampled again and zero-padded such that the number of points $\mathrm{NFFT} = 2^{11}$. The Fourier transform is then performed for both signals and evaluated at the center frequency of the pulse (Figure 4.4d). Once the time delay and ratio of spectral amplitudes are calculated between the nearest two reference signals, a linear interpolation in depth is performed and the sound speed and attenuation are calculated using Equations 4.2–4.3.

Appendix B

Fluid-filled elastic tube waveguide corrections

B.1 Axisymmetric modes

The exact dispersion relation from Lafleur and Shields [86] for the axisymmetric modes of an arbitrary-thickness elastic tube waveguide with inner radius b, outer radius d, wall density ρ_{t}, compressional wave speed C_{c}, and shear wave speed C_{s}, filled with a liquid of density ρ_{L} and free-field sound speed C_{L} is

$$\begin{aligned}
1 + [L_{11}(P_m)L_{00}(T_m)]\left(\frac{\pi^2 q_{0m}^2 bdP_m^2 T_m^2}{8E_m^2}\right) + [L_{11}(T_m)L_{00}(P_m)]\left(\frac{\pi^2 bdE_m^2}{8q_{0m}^2}\right) \\
+ [L_{10}(P_m)L_{01}(T_m) + L_{01}(P_m)L_{10}(T_m)]\left(\frac{\pi^2 bdP_m T_m}{8}\right) \\
+ [bL_{11}(P_m)L_{10}(T_m) + d(1+Q_m b)L_{11}(P_m)L_{01}(T_m)]\left(\frac{\pi^2 P_m^2 T_m}{8E_m} - \frac{\pi^2 P_m^2 q_{0m}^2 T_m}{8E_m^2}\right) \\
+ [bL_{11}(T_m)L_{10}(P_m) + d(1+Q_m b)L_{11}(T_m)L_{01}(P_m)]\left(\frac{\pi^2 P_m E_m}{8q_{0m}^2} - \frac{\pi^2 P_m}{8}\right) \\
+ [(1+Q_m b)L_{11}(T_m)L_{11}(P_m)]\left(\frac{\pi^2 P_m^2}{8q_{0m}^2} + \frac{\pi^2 P_m^2 q_{0m}^2}{8E_m^2} - \frac{\pi^2 P_m^2}{4E_m}\right) = 0, \quad \text{(B.1)}
\end{aligned}$$

where the following relations are defined

$$P_m = \sqrt{k_{\mathrm{c}}^2 - q_{0m}^2}, \quad T_m = \sqrt{k_{\mathrm{s}}^2 - q_{0m}^2}, \quad X_{0m} = b\sqrt{k_{\mathrm{L}}^2 - q_{0m}^2}, \qquad \text{(B.2)}$$

$$E_m = q_{0m}^2 - k_{\mathrm{s}}^2/2, \quad Q_m = \frac{\rho_{\mathrm{L}}\omega^2 b J_0(X_{0m})}{2\rho_{\mathrm{t}} C_{\mathrm{s}}^2 X_{0m} J_1(X_{0m})}, \qquad \text{(B.3)}$$

$$q_{0m} = \omega/C_{0m}, \quad k_{\mathrm{c}} = \omega/C_{\mathrm{c}}, \quad k_{\mathrm{s}} = \omega/C_{\mathrm{s}}, \quad k_{\mathrm{L}} = \omega/C_{\mathrm{L}}, \tag{B.4}$$

$$L_{ij}(y) = J_i(dy)Y_j(by) - J_j(by)Y_i(dy), \tag{B.5}$$

where J and Y are bessel functions of the first and second kind, respectively, and m is the modal branch number, where $m = 0, 1, 2, 3, ...$ Since Equation B.1 is limited to axisymmetric wave propagation, the first integer from the subscript notation $0m$ is zero. To convert from mechanical properties to compressional and shear wave speeds, the relations

$$C_{\mathrm{c}} = \sqrt{\frac{Y(1-\nu)}{\rho_{\mathrm{t}}(1+\nu)(1-2\nu)}}, \quad C_{\mathrm{s}} = \sqrt{\frac{Y}{2\rho_{\mathrm{t}}(1+v)}}, \tag{B.6}$$

can be used, where Y is the Young's modulus and ν is the Poisson's ratio of the tube wall.

B.2 Non-axisymmetric modes: elastic shell

The dispersion relation from Fuller and Fahy [96] for all propagating modes of a thin-walled fluid-filled elastic shell is

$$\det(M_{ij}) = 0, \tag{B.7}$$

where M is a 3×3 matrix with components

$$M_{11} = -\Omega^2 + (q_{nm}a)^2 + \frac{1}{2}(1-\nu)n^2, \quad M_{12} = \frac{1}{2}(1+\nu)n(q_{nm}a), \quad M_{13} = \nu(q_{nm}a),$$
$$M_{21} = M_{12}, \quad M_{22} = -\Omega^2 = \frac{1}{2}(1-\nu)(q_{nm}a)^2 + n^2, \quad M_{23} = \nu,$$
$$M_{31} = M_{13}, \quad M_{32} = M_{23}, \quad M_{33} = -\Omega^2 + 1 + \beta^2[(q_{nm}a)^2 + n^2]^2 - \text{FL}. \tag{B.8}$$

In Equations B.8, $h = d - b$ is the shell thickness, $a = (b + d)/2$ is the shell radius, $\beta^2 = h^2/(12a^2)$ is the shell thickness parameter, ν is the Poisson's ratio of the shell, $\Omega = \omega a/c_{\text{e}}$ is the non-dimensional frequency, and $c_{\text{e}} = [Y/((1 - \nu^2)\rho_{\text{t}})]^{1/2}$ is the extensional phase speed of the shell material *in vacuo* [137,138]. The fluid loading term FL is given by

$$\text{FL} = \Omega^2(\rho_{\text{L}}/\rho_{\text{t}})(h/a)^{-1}(k_m^{\text{r}}a)^{-1}[J_n(k_m^{\text{r}}a)/J_n'(k_m^{\text{r}}a)], \tag{B.9}$$

where the radial fluid wavenumber $k_m^{\text{r}}a$ is coupled to the axial wavenumber q_{nm} written as

$$k_m^{\text{r}}a = \pm[\Omega^2(c_{\text{e}}/c_L)^2 - (q_{nm}a)^2]^{1/2}, \tag{B.10}$$

$$q_{nm} = \omega/C_{nm}, \tag{B.11}$$

where C_{nm} is the axial phase speed in the thin fluid-filled shell at circumferential mode number n and modal branch number m. The two fluid-filled elastic tube waveguide models, converge when $h/a << 1$ and $n = 0$.

B.3 Free-field sound speed correction

The free-field sound speed of the fluid C_{L} can be solved by implementing a zero finder algorithm on either Equation B.1 if $n = 0$ or Equation B.8 if $h/a << 1$, provided the measured axial phase speed C_{nm} in the waveguide using the resonance tube technique, all other measured dimensions and tabulated material properties of the tube, i.e. $b, d, \rho_{\mathrm{t}}, Y, \nu$, and the density of the liquid ρ_{L} are known. The axial phase speed using the resonance tube technique with pressure release boundary conditions is calculated by

$$C_{nm}(f_{nml}) = f_{nml}\frac{2L}{l}, \tag{B.12}$$

where L is the length of the fluid column, $l = 1, 2, 3, ...$ is the axial mode number between two pressure release boundaries, and f_{nml} is the resonance frequency at mode number nml.

Appendix C

CARL transducer loading

In resonance mode (Section 4.2.2), the Core and Resonance Logger (CARL) transducers sense the resonance frequencies and standing-wave pattern of the core sample through a thin plastic core liner. The resonance frequencies were shown in Figure 4.5 to vary as the position of the transducers the anti-nodes of the standing wave patterns. Since the elastic waveguide models in Appendix B do not include this mass loading effect, it is imperative to the measurement to investigate where this effect is minimized, such that the resonance frequency can be more accurately estimated. To this end, a 3-dimensional finite element model (FEM) of a 30-in-long D7 core liner from Table 4.1, filled with synthetic oil (Table 4.2) to a height of 25.2 cm, was simulated in COMSOL. Resonance frequencies were computed using the eigenfrequency solver, and the maximum element size was set to one tenth of a wavelength in the oil. Mode numbers 021, 025, and 026 were investigated.

First, the eigenfrequency at each mode was computed without the transducers present. Next, synthetic-oil-filled cylindrical core logger transducers that made contact with the core liner walls were introduced into the simulation, shown in Figure C.1a. The shape of the contact area approximated

an ellipse with a major and minor axis of 2.5 cm and 2 cm, respectively. To reduce the number of elements by 4, two planes of symmetry were prescribed. The geometry of the simulated transducers were based on a loaned set of Geotek rolling core logger transducers previously used for CARL measurements in the field. The simulated transducer was prescribed pressure release boundaries, excluding where the transducer and core liner made contact. Although the simplified model of the transducer may load the sample differently in the simulation than in the measurement, the effect due to loading can be qualitatively studied.

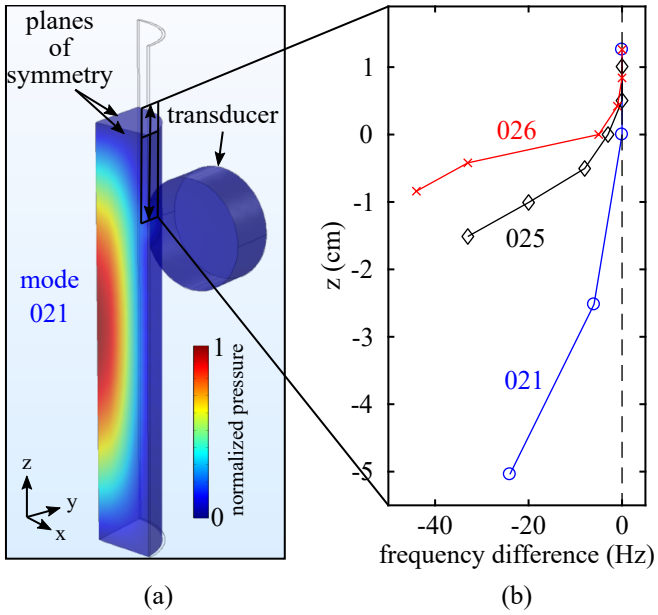

Figure C.1: (a) The simulated pressure field at the 021 mode is shown. (b) The resonance frequency difference due to the presence of the transducers is plotted for modes 021, 025, and 026 at various transducer positions. The dashed black line corresponds to the transducer-free system.

At each mode, the transducers were incrementally lowered, and the

eigenfrequencies of the system were computed at each depth increment. Figure C.1b shows the difference between the resonance frequency with and without the transducers at several transducer positions. The vertical dashed black line marks where the system's resonance frequency with the transducers present converges with the resonance frequency without the transducers present.

As the transducers were lowered from the top of the core liner, toward the first anti-node, a reduction in resonance frequency was observed that deviated from the transducer-free system. The resonance frequencies converged as the transducer was moved above the air-sample interface. This convergence was attributed to effectively decreasing the portion of the contact area below the air-sample interface. Mode 021 reached convergence at $z = 0$ cm, while 025 and 026 did not reach convergence until $z = 0.5$ cm and 0.8 cm, respectively. Theoretically, the resonance frequencies would converge with the transducer-free system, if a point-mass loading was applied at the nulls of the standing wave. However, since the finite contact area encompassed a larger portion of the standing-wave at higher-order modes, a 0.5-cm-resolution scan in depth was performed above the air-sample interface to adequately measure the correct resonance frequency, and bypass the transducer loading effect.

Appendix D

CARL uncertainty analysis

D.1 Pitch-catch mode

In pitch-catch mode, uncertainty is estimated by first propagating the uncertainty through Equation 4.2 assuming the inner diameter of the core liner D is constant between reference and sample measurements. Partial derivatives taken with respect to the uncertain parameters are given by

$$\frac{\partial c}{\partial c_{\mathrm{w}}} = -\left[\frac{1}{c_{\mathrm{w}}} - \frac{\Delta t}{D}\right]^{-2} \frac{1}{c_{\mathrm{w}}^2}, \tag{D.1a}$$

$$\frac{\partial c}{\partial t} = -\left[\frac{1}{c_{\mathrm{w}}} - \frac{\Delta t}{D}\right]^{-2} \frac{1}{D}, \tag{D.1b}$$

$$\frac{\partial c}{\partial D} = \left[\frac{1}{c_{\mathrm{w}}} - \frac{\Delta t}{D}\right]^{-2} \frac{\Delta t}{D^2}. \tag{D.1c}$$

Next, partial derivatives are performed assuming the inner diameter of the core liner and transducer separation distance varied between reference and sample measurements. The altered sample sound speed equation including a change in the sample inner diameter is

$$c = \left[\frac{1}{c_{\mathrm{w}}} + \frac{\Delta D}{D}\left[\frac{1}{c_{\mathrm{w}}} - \frac{1}{c_{\mathrm{o}}}\right] - \frac{\Delta t}{D}\right]^{-1}, \tag{D.2}$$

where c_{o} is the sound speed of the oil in the CARL transducer. The altered sound speed equation including a change in the transducer separation distance

$\hat{D}$ is

$$c = \left[\frac{1}{c_\mathrm{w}} + \frac{\Delta\hat{D}}{Dc_\mathrm{o}} - \frac{\Delta t}{D}\right]^{-1}. \tag{D.3}$$

Partial derivates of Equations D.2 and D.3 are

$$\frac{\partial c}{\partial \Delta D} = -\left[\frac{1}{c_\mathrm{w}} + \frac{\Delta D}{D}\left[\frac{1}{c_\mathrm{w}} - \frac{1}{c_\mathrm{o}}\right] - \frac{\Delta t}{D}\right]^{-2}\left[\frac{1}{c_\mathrm{w}} - \frac{1}{c_\mathrm{o}}\right]\frac{1}{D}, \tag{D.4a}$$

$$\frac{\partial c}{\partial \Delta \hat{D}} = \left[\frac{1}{c_\mathrm{w}} + \frac{\Delta\hat{D}}{Dc_\mathrm{o}} - \frac{\Delta t}{D}\right]^{-2}\frac{1}{Dc_\mathrm{o}}, \tag{D.4b}$$

respectively. The quadrature sum of Equations D.1a and D.4a yield the uncertainty estimate for the CARL sound speed measurement and equates to

$$\mathrm{d}c = \left[\left(\frac{\partial c}{\partial c_\mathrm{w}}\mathrm{d}c_\mathrm{w}\right)^2 + \left(\frac{\partial c}{\partial t}\mathrm{d}t\right)^2 + \left(\frac{\partial c}{\partial D}\mathrm{d}D\right)^2 + \left(\frac{\partial c}{\partial \Delta D}\mathrm{d}\Delta D\right)^2 + \left(\frac{\partial c}{\partial \Delta \hat{D}}\mathrm{d}\Delta\hat{D}\right)^2\right]^{1/2}, \tag{D.5}$$

where $\mathrm{d}c_\mathrm{w}$ is determined by propagating the temperature resolution uncertainty of the thermocouple through an empirical equation for the sound speed of water described in Coppens [49], $\mathrm{d}t$ combines the standard error of the time delays calculated between the two nearest reference measurements and the resolution error, $\mathrm{d}D = \mathrm{d}\Delta D = 0.5$ mm, and $\mathrm{d}\hat{D} = 0.35$ mm is determined by measuring the distance the transducers could be manually perturbed.

For uncertainty in the attenuation measurement, the partials derivates from Equation 4.3 are

$$\frac{\partial \alpha}{\partial D} = -\frac{20}{D^2}\log_{10}\left[\frac{|S_\mathrm{w}(f_0)|}{|S(f_0)|}\right] \tag{D.6a}$$

$$\frac{\partial \alpha}{\partial S_\mathrm{w}} = \frac{20}{D\ln(10)|S_\mathrm{w}(f_0)|}, \tag{D.6b}$$

where ln is the natural log. Similarly, partials are summed in quadrature to yield the uncertainty in the attenuation give as

$$\mathrm{d}\alpha = \left[\left(\frac{\partial\alpha}{\partial D}\mathrm{d}D\right)^2 + \left(\frac{\partial\alpha}{\partial S_\mathrm{w}}\mathrm{d}S_\mathrm{w}\right)^2\right]^{1/2}, \tag{D.7}$$

where $\mathrm{d}S_\mathrm{w}$ is the standard error of the spectral amplitude calculated for the two nearest reference measurements.

D.2 Resonance mode

In resonance mode, uncertainty in the length of the sample and the frequency resolution of the measurement are propagated through Equation 4.6 and is of the form

$$\mathrm{d}C_{nm} = f_{nml}\frac{2L}{l}\left[\left(\frac{\mathrm{d}f}{f_{nml}}\right)^2 + \left(\frac{\mathrm{d}L}{L}\right)^2\right]^{1/2}, \tag{D.8}$$

where $\mathrm{d}C_{nm}$ is the phase speed uncertainty. Particularly for resonances near the cutoff for the modes with $m > 1$, the sound speed inference using the Lafleur and Shields [86] or Fuller and Fahy [96] models in Appendix B is most sensitive and inversely proportional to the inner radius. To conservatively incorporate this uncertainty in to the sound speed calculation, the model inference is performed twice. In the first inference, the lower bounds for the phase speed $C_{nm} - \mathrm{d}C_{nm}$ and the inner radius $b - \mathrm{d}b$ are used as model inputs to calculate the sample sound speed lower bound. Conversely, in the second inference, the upper bounds for the phase speed $C_{nm} + \mathrm{d}C_{nm}$ and the inner radius $b + \mathrm{d}b$ are used to calculate the sample sound speed upper bound.

Appendix E

Accounting for bubbles in seagrass-bearing sediment

Organic-rich seagrass-bearing sediment contains complex air channels within the aerenchyma (tissue) of the plant, as well as bubbles in the sediment formed by the decomposition of organic material. The acoustic response of the sediment is dominated by the presence of these voids at a frequency below or near their resonance, but converge to the background medium at frequencies sufficiently above resonance. While investigating the relationship between organic carbon and sediment acoustic properties of seagrass-bearing sediment in Chapter 5, correlations were made at the highest frequency measured by CARL (300 kHz) to minimize the effect the air voids had on the acoustic properties. This appendix begins with an X-ray Computed Tomography (CT) scan rendering of a representative seagrass-bearing sediment core to help the reader visualize the complexities associated with the different sediment constituents, such as the coarse shell hash, seagrass tissue, and voids. Next, a bubbly sediment model was fit to sound speed data taken at two depths from a seagrass-bearing sediment and bare patch core from Chapter 5. Using the best fit parameter set, a sediment model free of bubbles was also plotted to demonstrate that near 300 kHz, the bubbly sediment model and bubble-free

sediment model sound speeds converged.

E.1 Seagrass-bearing sediment

A 20-cm sediment core was taken from the same *T. testudinum* seagrass meadow described in Chapter 5 on a subsequent experiment to image the internal structure of the core using X-ray CT performed in the University of Texas High-Resolution X-ray Computed Tomography Facility (UTCT). The output from the CT scan consisted of N 16-bit cross-sectional images of the scanned core, where N is the number of one-voxel-thick layers taken along the length of the scan. A voxel is a three-dimensional pixel that is assigned a grey value from 0 to 255 based on the average electron density within each voxel. Materials with a high electron density, such as shells and sediment grains, appeared bright and were assigned higher grey values closer to 255, while materials with a low electron density, such as gas, appeared dark and were assigned lower grey values closer to 0. For this CT scanned, the voxel size or resolution of the image was (38.1 μm)$\times$(38.1 μm)$\times$(38.1 μm).

Using the Aviso Lite software provided by UTCT, the raw CT images were stacked on top of one another to construct a three-dimensional image of the core. Then, grey value thresholds were assigned to each constituent and voxels could thus be segmented. For example, gas was assigned grey values from 0–37, which was determined by measuring the average grey value from the air outside of the core. Shell hash was assigned grey values from 119–255, by taking the lower and upper limits of several shell hash fragments. Sea-

grass tissue threshold values were found in a similar manner. Since sediment grains and water have similar grey values to those assigned to the shell hash and seagrass tissue, respectively, there was significant speckle present that required more post processing. Shrinking and growing functions were used to average out the speckle formed by sediment grains and high porosity sediment to produce the processed three-dimensional rendering.

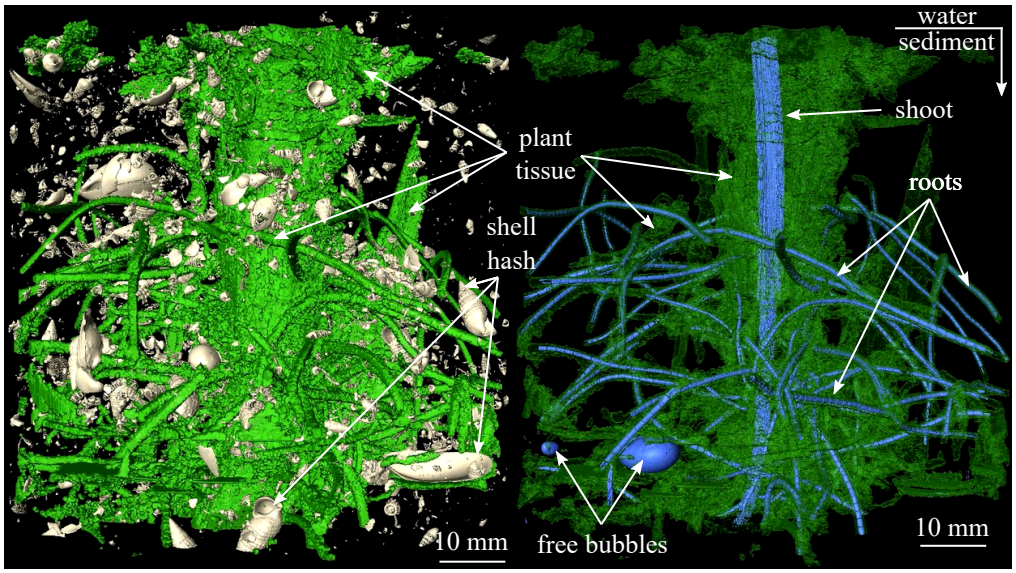

Figure E.1: Two renderings of a CT scan of a seagrass-bearing sediment core are presented. The sediment was substracted from the rendering to reveal the internal structure of the (a) below-ground biomass (green), and coarser shell hash (white), and the (b) encapsulated gas bubbles (blue) observed within the top 8 cm of the core.

The top 8 cm of the seagrass-bearing sediment core is shown in Figure E.1, where the sediment was subtracted from the rendering to reveal different structures present in the core. Figure E.1a presents a rendering of the

seagrass tissue, shown in green, and fragments of shell from decaying organisms such as gastropods and crustaceans within the sediment, shown in white. Figure E.1b depicts the seagrass tissue as a translucent green to reveal the structure of the gas channels within the seagrass shoot and roots, shown in blue, as well as some free bubbles found within the sediment, also shown in blue. In the shoot, multiple vertically-oriented cylindrical air channels were observed that tapper in diameter as they connect to the leaves. The voids present within the roots had a different structure. The cross section along each root consisted of a cylindrical volume of plant tissue surrounded by an annulus of air, and encapulated by another layer of tissue. The annulus of air was not continuous along the length of the root, but was segmented by thin tissue layers into multiple discrete 2-mm-long tubular voids. Although a bubbly sediment acoustics model that specifically accounts for these complex seagrass-tissue-encapsulated bubbles does not currently exist, a bubbly sediment model developed for spherical bubbles [120] adequately described the dispersion observed in samples presented in Chapter 5.

E.2 Bubbly sediment model fit

A bubbly sediment model developed by Dogan *et al.* [120] was fit to sound speed data in both a seagrass-bearing sediment and bare patch core at a depth of 4 cm (Figure E.2a) and 38 cm (Figure E.2b). The model assumed the background sediment behaved as an EDFM [26] outlined in Chapter 3 Section 3.2.2. Dogan *et al.* describe that at frequencies below bubble reso-

nance, the compliance of the bubble dominates and reduces the sediment sound speed. As the frequency increases above bubble resonance, a 180° phase shift occurs in the bubble response, resulting in a faster sound speed than would be observed in the bubble-free sediment. As the frequency becomes sufficiently higher than bubble resonance, sound speed of the bubbly sediment and the bubble-free sediment converge [120]. The dispersion observed within the frequency regime of the experiment (100 kHz to 300 kHz) occurred mostly above bubble resonance. This fitting exercise was performed not to suggest that this bubbly sediment model is appropriate for the complex voids observed in seagrass-bearing sediment, but to demonstrate that 300 kHz is sufficiently higher than the resonance frequency of the gas channels, such that the sound speed of the bubbly sediment converges to that of the bubble-free sediment.

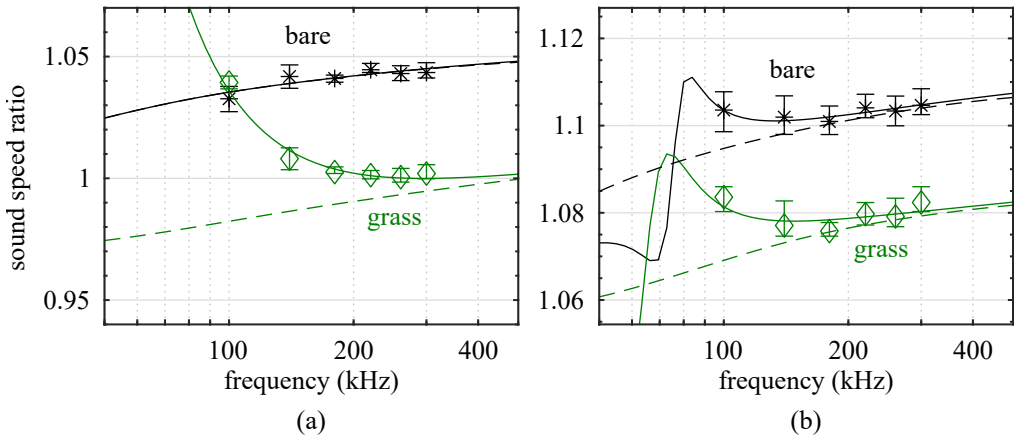

Figure E.2: Sound speed ratio CARL measurements for a seagrass-bearing (green diamonds) and bare patch (black astricks) sediment cores measured at a depth of (a) 4 cm and (b) 38 cm. A gassy EDFM (solid line) was fit to data. A bubble-free EDFM (dashed line) using the same input parameters used in the gassy EDFM is shown to converge near 300 kHz.

All input parameters used to plot the bubbly EDFM models in Figure E.2 are displayed in Table E.1. Sediment permeability, pore-water viscosity, mean bubble radius, and void fraction were the fitted parameters, while porosity and mean grain diameter were directly measured and held fixed. The shear wave speed c_s and attenuation α_s were taken from near by *in situ* measurements at 1 kHz [139], and used to calculate the complex shear modulus G^* of the form

$$G^* = \rho_\mathrm{sed} c_\mathrm{s}^{*2}, \tag{E.1}$$

where c_s^* is the complex shear speed given by

$$c_\mathrm{s}^* = \left[\frac{1}{c_\mathrm{s}} - i\frac{\alpha_\mathrm{s}}{\omega}\right]^{-1}. \tag{E.2}$$

Although the EDFM assumes the sediment behaves as a fluid, the complex shear modulus was required by the bubbly EDFM to account for viscous, thermal, interfacial, and elastic bubble damping coefficients in the near-field, to adequately calculate the resonance frequency. The sediment tortuosity was coupled to the permeability, mean grain diameter and porosity using the Kozeny-Carmen relation from Equation 3.15. The remaining parameters were either taken from tabulated values in the literature [9, 120] or directly calculated from measured temperature and salinity of the pore-water using relations from References 48, 49. The best-fit model was determined by minimizing an error function of the form presented in Reference 85, which was a least squares approach weighted by the inverse of the covariance matrix. The covariance matrix was a diagonal matrix composed from the measured variance in sound

speed data at each discrete frequency point. Once the best-fit model parameter set was found, it was then inputted into the bubble-free EDFM and plotted in Figure E.2 with dashed lines.

Table E.1: Input parameters to the bubbly EDFM models used in Figure E.2 for two distinct depths and cores. All parameters above the horizontal line are input parameters to the bubble-free EDFM model.

parameter	symbol	seagrass (4 cm)	seagrass (38 cm)	bare (4 cm)	bare (38 cm)
density of pore water[E]	ρ_w (kg/m^3)	1027.9	1027.9	1027.9	1027.9
density of grain[T1]	ρ_g (kg/m^3)	2648	2648	2648	2648
bulk modulus of pore water[E]	K_w (GPa)	2.39	2.39	2.39	2.39
bulk modulus of grain[T1]	K_g (GPa)	36.0	36.0	36.0	36.0
porosity[M]	β	0.832	0.442	0.554	.450
mean grain diameter[M]	d (μm)	16.59	56.41	56.95	81.06
permeability[F]	κ (m^2)	6.950×10^{-9}	1.623×10^{-12}	1.290×10^{-11}	1.079×10^{-11}
tortuosity[C]	τ	1.06	2.74	1.73	1.59
pore-water viscosity[F]	η (Pa $\cdot$ s)	39.63×10^{-3}	7.38×10^{-3}	13.47×10^{-3}	8.88×10^{-3}
bubble radius[F]	r_0 (mm)	1.046	0.220	-	0.122
void fraction[F]	Γ	7.309×10^{-3}	3.567×10^{-5}	-	5.220×10^{-6}
sediment shear modulus[M]	G (MPa)	1.520	6.534	0.9650	2.526
imaginary shear modulus[M]	G$'$ (MPa)	0.175	1.492	0.87	0.226
ratio of specific heats of air[T2]	γ_a	1.4	1.4	1.4	1.4
thermal diffusivity of air[T2]	ν_a (m^2/s)	2.08×10^{-5}	2.08×10^{-5}	2.08×10^{-5}	2.08×10^{-5}
surface tension[T2]	σ (N/m)	72.57×10^{-3}	72.57×10^{-3}	72.57×10^{-3}	72.57×10^{-3}

[M] Measured parameter

[E] Empirically calculated using relations in References 48, 49.

[T1] Tabulated parameter taken from Reference 9.

[T2] Tabulated parameter taken from Reference 120.

[F] Fitted parameter.

[C] Coupled to permeability, mean grain diameter, and porosity using Equation 3.15.

The best-fit bubbly sediment model agreed well with the sound speed data at both depths for the seagrass and bare patch core. The fitted parameters also yield reasonable values. For example, although the tortuosity was not constrained in the parameter space search, it remained between theoretical bounds $1 \leq \tau \leq 3$ [25]. It was also shown that the bubbly sediment model mostly converged with the bubble-free model near 300 kHz, with the exception of the seagrass-bearing core at 4 cm (Figure E.2a). However, at 300 kHz, the sound speed was reported to within only 1% of the bubble-free sediment. This demonstrates the small, yet inherent, uncertainty in assumption made in Chapter 5. It is also worth noting that in the bare patch core at 4 cm, the bubbly EDFM and bubble-free EDFM within the frequency regime of the measurement were indistinguishable. This meant that either there were not any bubbles present at that depth, or the bubble resonance occurred at a much lower frequency and the acoustic response was, therefore, insensitive to the presence such large bubbles. Since the model was under-constrained at such a frequency range, the bubble radius and void fraction for the 4-cm-depth bare patch core were not tabulated. The author admits this bubbly sediment model is an oversimplification of the physics responsible for the acoustic response of the voids. For this reason, investigation into modeling acoustic propagation through seagrass-bearing sediment below or near resonance is ongoing and requires further investigation.

Appendix F

Engineering drawings

Engineering drawings are provided for all custom-designed parts manufactured by the machinists at the Applied Research Laboratories. Since the drawings were originally requested in imperial units, they were not converted into SI units. The drawings include components from: the sample holder and tower used in Chapter 2, the piston (stinger) used in Chapters 3 and 4, the hydrophone holder used in Chapter 3, the time-of-flight fixture used in Chapters 3 and 4, and the Core and Resonance Logger (CARL) transducer assemblies and fixture system used in Chapter 4.

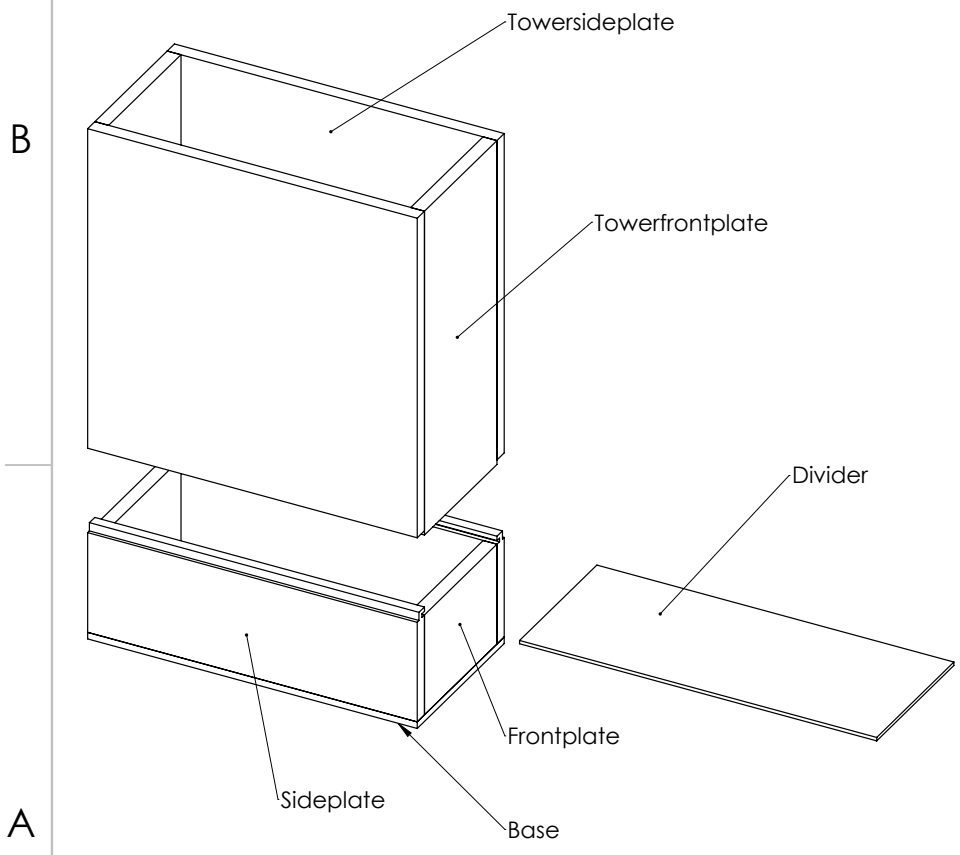

		DIMENSIONS ARE IN INCHES TOLERANCES: FRACTIONAL ± ANGULAR: MACH ± BEND ± TWO PLACE DECIMAL ± THREE PLACE DECIMAL ±		NAME	DATE
			DRAWN		
			CHECKED		
			ENG APPR.		
			MFG APPR.		
		MATERIAL: Polycarbonate	Q.A.		
			COMMENTS:		
NEXT ASSY	USED ON	FINISH			
APPLICATION		DO NOT SCALE DRAWING			

PROPRIETARY AND CONFIDENTIAL

THE INFORMATION CONTAINED IN THIS DRAWING IS THE SOLE PROPERTY OF <COMPANY NAME >. ANY REPRODUCTION IN PART OR AS A WHOLE WITHOUT THE WRITTEN PERMISSION OF <COMPANY NAME> IS PROHIBITED.

Gabe Venegas

SIZE	DWG. NO.	REV.
A	sampleholderassem	
SCALE:1:5	WEIGHT:	SHEET 1 OF 1

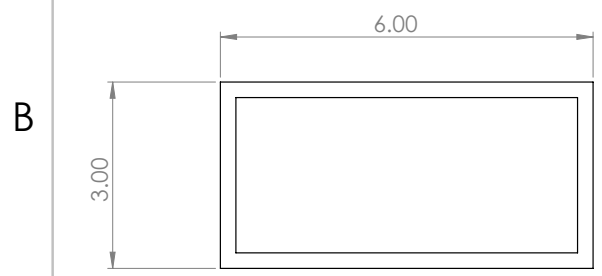

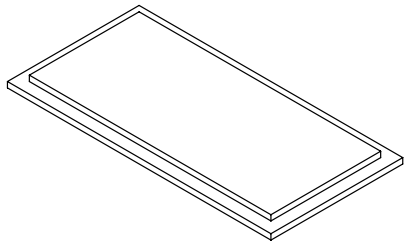

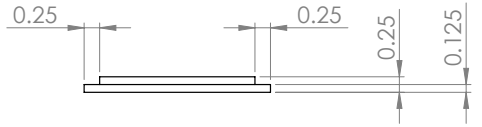

		UNLESS OTHERWISE SPECIFIED:		NAME	DATE
		DIMENSIONS ARE IN INCHES TOLERANCES: FRACTIONAL ± ANGULAR: MACH ± BEND ± TWO PLACE DECIMAL ± THREE PLACE DECIMAL ±	DRAWN		
			CHECKED		
			ENG APPR.		
			MFG APPR.		
		INTERPRET GEOMETRIC TOLERANCING PER:	Q.A.		
		MATERIAL polycarbonate	COMMENTS:		
NEXT ASSY	USED ON	FINISH			
APPLICATION		DO NOT SCALE DRAWING			

PROPRIETARY AND CONFIDENTIAL

THE INFORMATION CONTAINED IN THIS DRAWING IS THE SOLE PROPERTY OF <INSERT COMPANY NAME HERE>. ANY REPRODUCTION IN PART OR AS A WHOLE WITHOUT THE WRITTEN PERMISSION OF <INSERT COMPANY NAME HERE> IS PROHIBITED.

TITLE:

Gabe Venegas

SIZE	DWG. NO.	REV
A	Base	
SCALE: 1:2	WEIGHT:	SHEET 1 OF 1

1.50

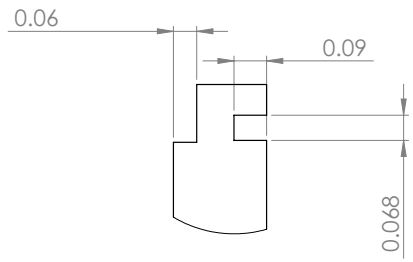

DETAIL B

SCALE 3 : 1

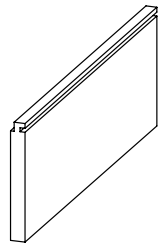

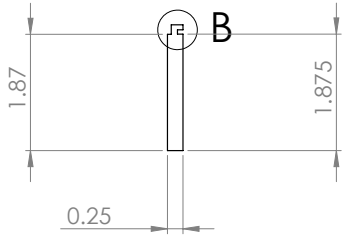

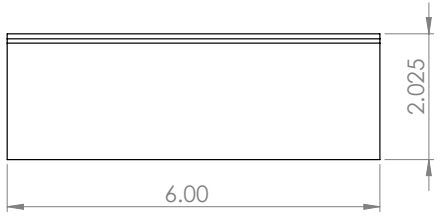

		UNLESS OTHERWISE SPECIFIED:		NAME	DATE
		DIMENSIONS ARE IN INCHES TOLERANCES: FRACTIONAL ± ANGULAR: MACH ± BEND ± TWO PLACE DECIMAL ± THREE PLACE DECIMAL ±	DRAWN		
			CHECKED		
			ENG APPR.		
			MFG APPR.		
		INTERPRET GEOMETRIC TOLERANCING PER:	Q.A.		
		MATERIAL polycarbonate	COMMENTS:		
NEXT ASSY	USED ON	FINISH			
APPLICATION		DO NOT SCALE DRAWING			

TITLE:

Gabe Venegas

SIZE	DWG. NO.	REV
A	Frontplate	
SCALE: 1:2	WEIGHT:	SHEET 1 OF 1

151

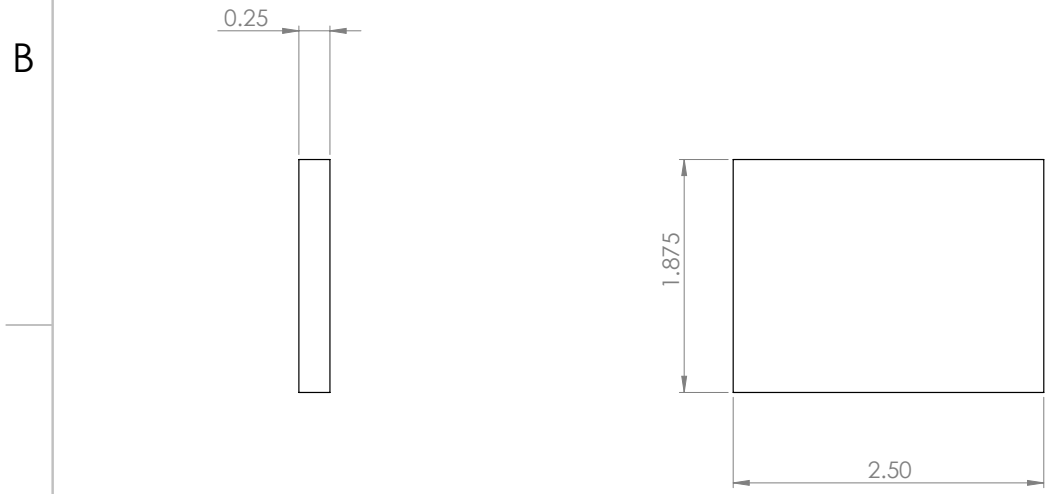

		UNLESS OTHERWISE SPECIFIED:		NAME	DATE
		DIMENSIONS ARE IN INCHES TOLERANCES: FRACTIONAL ± ANGULAR: MACH ± BEND ± TWO PLACE DECIMAL ± THREE PLACE DECIMAL ±	DRAWN		
			CHECKED		
			ENG APPR.		
			MFG APPR.		
		INTERPRET GEOMETRIC TOLERANCING PER:	Q.A.		
		MATERIAL: Polycarbonate	COMMENTS:		
NEXT ASSY	USED ON	FINISH			
APPLICATION		DO NOT SCALE DRAWING			

TITLE: Gabe Venegas

SIZE	DWG. NO.	REV
A	Side Plate	
SCALE: 1:1	WEIGHT:	SHEET 1 OF 1

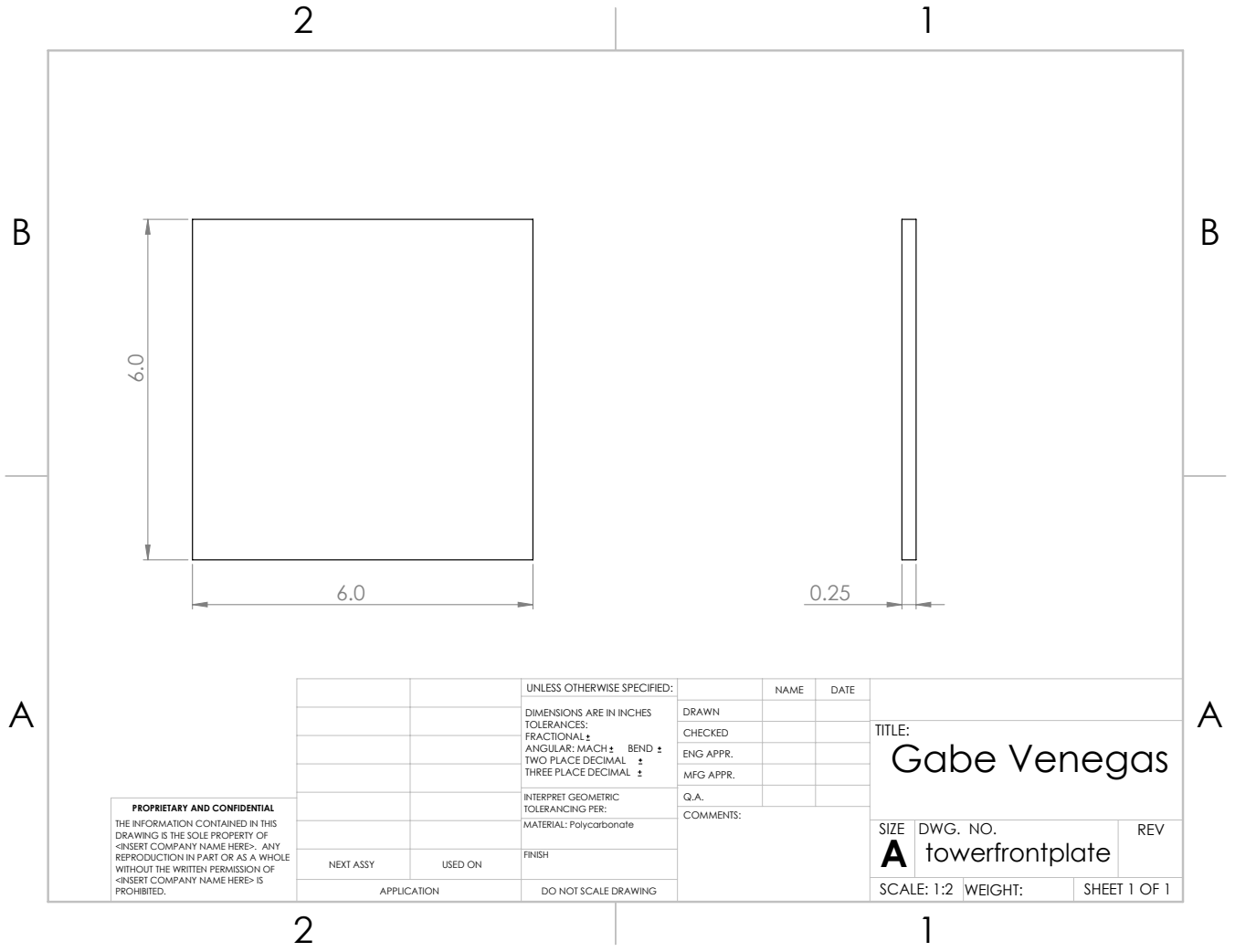

		UNLESS OTHERWISE SPECIFIED:		NAME	DATE
		DIMENSIONS ARE IN INCHES TOLERANCES: FRACTIONAL ± ANGULAR: MACH ± BEND ± TWO PLACE DECIMAL ± THREE PLACE DECIMAL ±	DRAWN		
			CHECKED		
			ENG APPR.		
			MFG APPR.		
		INTERPRET GEOMETRIC TOLERANCING PER:	Q.A.		
		MATERIAL: Polycarbonate	COMMENTS:		
NEXT ASSY	USED ON	FINISH			
APPLICATION		DO NOT SCALE DRAWING			

TITLE:

Gabe Venegas

SIZE	DWG. NO.	REV
A	towerfrontplate	
SCALE: 1:2	WEIGHT:	SHEET 1 OF 1

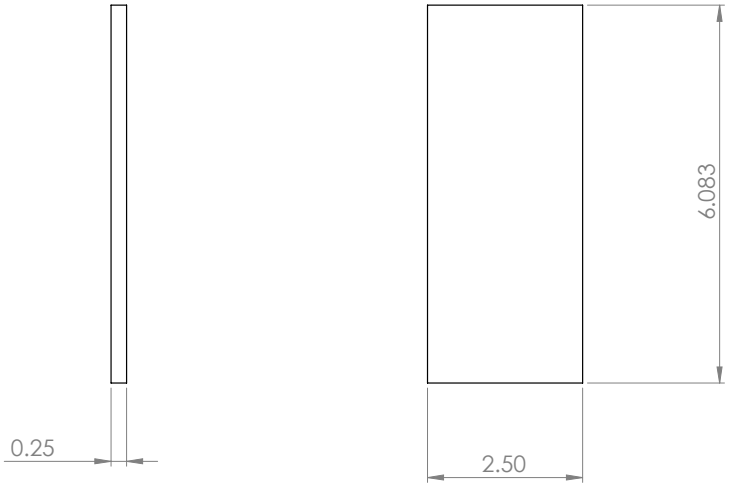

		UNLESS OTHERWISE SPECIFIED:		NAME	DATE
		DIMENSIONS ARE IN INCHES TOLERANCES: FRACTIONAL ± ANGULAR: MACH ± BEND ± TWO PLACE DECIMAL ± THREE PLACE DECIMAL ±	DRAWN		
			CHECKED		
			ENG APPR.		
			MFG APPR.		
		INTERPRET GEOMETRIC TOLERANCING PER:	Q.A.		
		MATERIAL: Polycarbonate	COMMENTS:		
NEXT ASSY	USED ON	FINISH			
APPLICATION		DO NOT SCALE DRAWING			

TITLE: Gabe Venegas

SIZE	DWG. NO.	REV
A	towersideplate	
SCALE: 1:2	WEIGHT:	SHEET 1 OF 1

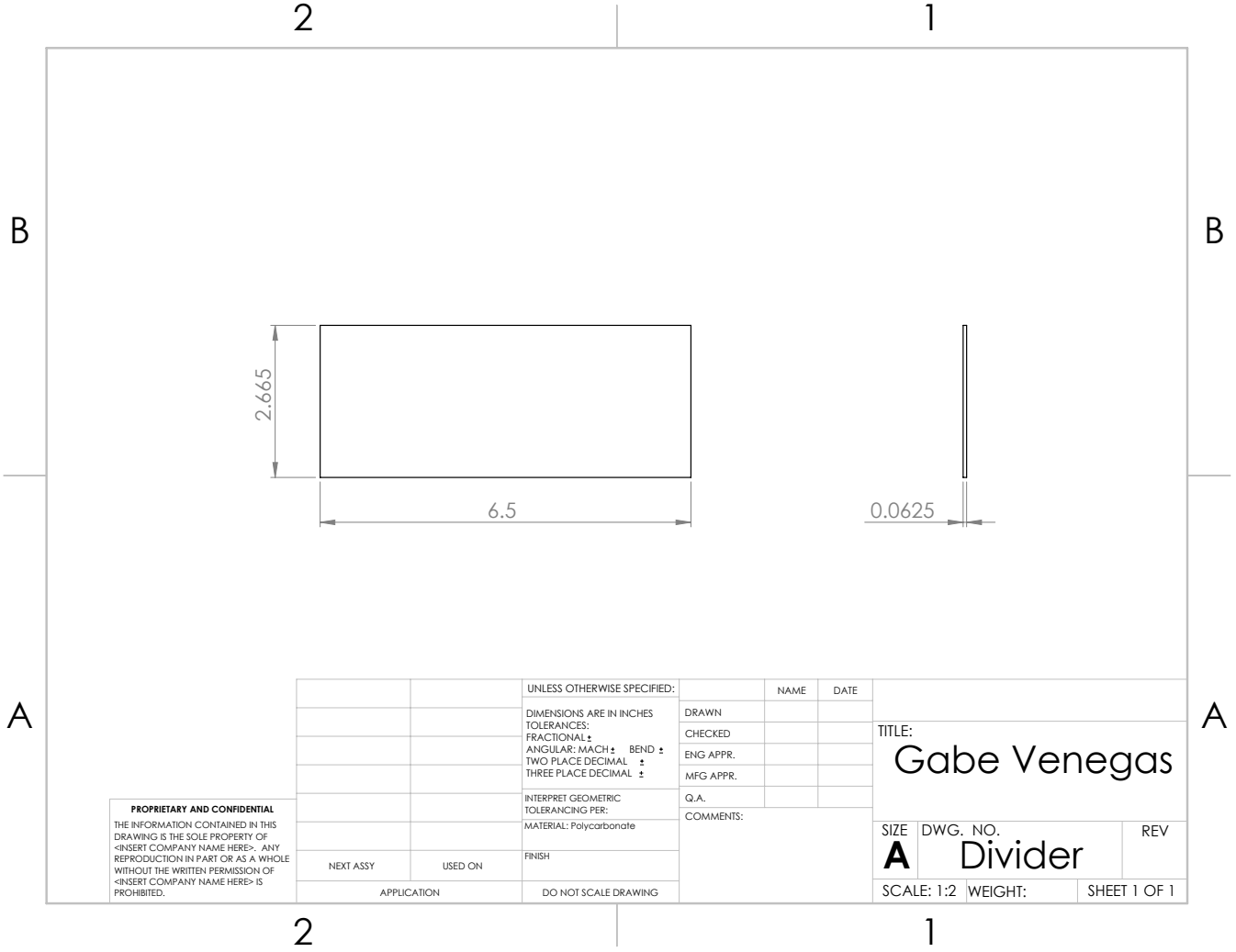
2
1
B
A
2.665
6.5
0.0625
UNLESS OTHERWISE SPECIFIED:
DIMENSIONS ARE IN INCHES
TOLERANCES:
FRACTIONAL ±
ANGULAR: MACH ± BEND ±
TWO PLACE DECIMAL ±
THREE PLACE DECIMAL ±
INTERPRET GEOMETRIC TOLERANCING PER:
MATERIAL: Polycarbonate
FINISH
NEXT ASSY
USED ON
APPLICATION
DO NOT SCALE DRAWING
NAME
DATE
DRAWN
CHECKED
ENG APPR.
MFG APPR.
Q.A.
COMMENTS:
TITLE:
Gabe Venegas
SIZE
A
DWG. NO.
Divider
REV
SCALE: 1:2
WEIGHT:
SHEET 1 OF 1
PROPRIETARY AND CONFIDENTIAL
THE INFORMATION CONTAINED IN THIS DRAWING IS THE SOLE PROPERTY OF <INSERT COMPANY NAME HERE>. ANY REPRODUCTION IN PART OR AS A WHOLE WITHOUT THE WRITTEN PERMISSION OF <INSERT COMPANY NAME HERE> IS PROHIBITED.

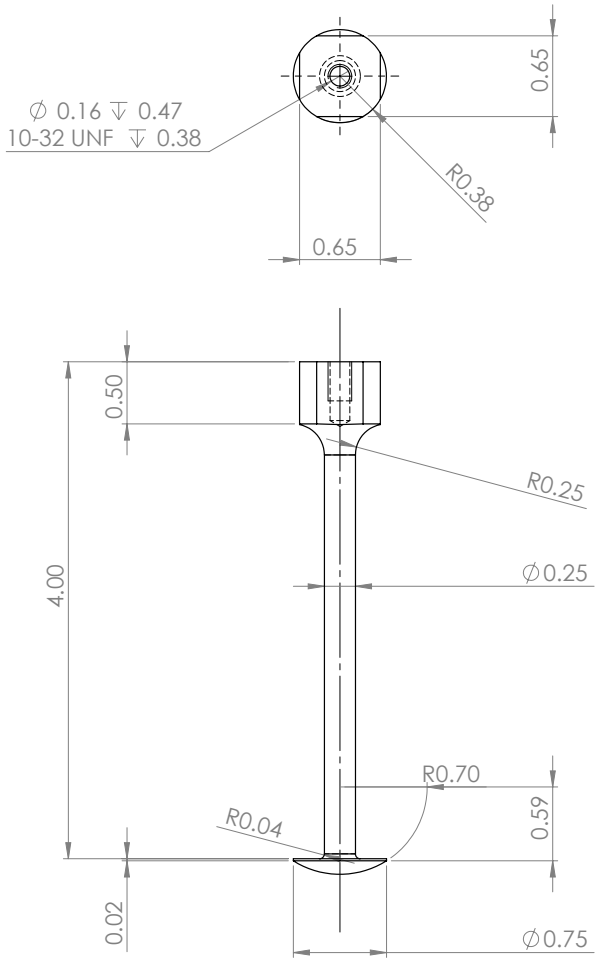

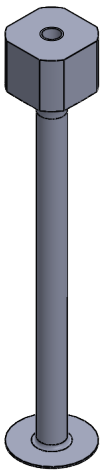

DIMENSIONS ARE IN INCHES TOLERANCES: TWO PLACE DECIMAL ±.005		NAME	DATE
	DRAWN	Gabe Venegas	2/25/14
	CHECKED	Preston Wilson	
	ENG APPR.		
	MFG APPR.		
	Q.A.		
MATERIAL: Aluminum	COMMENTS:		
FINISH			
DO NOT SCALE DRAWING			

Gabe Venegas (781)632-6488

Stinger

SIZE	DWG. NO.	REV.
A	001	
SCALE:1:1	WEIGHT:	SHEET 1 OF 1

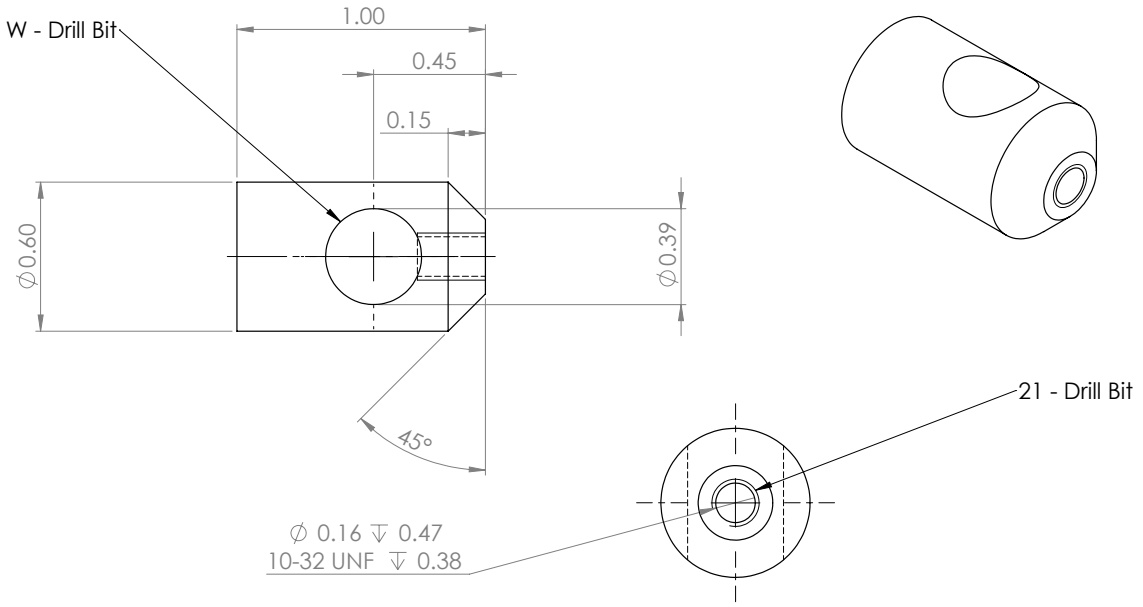

		UNLESS OTHERWISE SPECIFIED:		NAME	DATE
		DIMENSIONS ARE IN INCHES TOLERANCES: FRACTIONAL ± ANGULAR: MACH ± BEND ± TWO PLACE DECIMAL ± THREE PLACE DECIMAL ±	DRAWN		
			CHECKED		TITLE:
			ENG APPR.		
			MFG APPR.		
		INTERPRET GEOMETRIC TOLERANCING PER:	Q.A.		
		MATERIAL	COMMENTS:		SIZE DWG. NO. REV
NEXT ASSY	USED ON	FINISH			Hydrophoneholder
APPLICATION		DO NOT SCALE DRAWING			SCALE: 2:1 WEIGHT: SHEET 1 OF 1

5 4 3 2 1

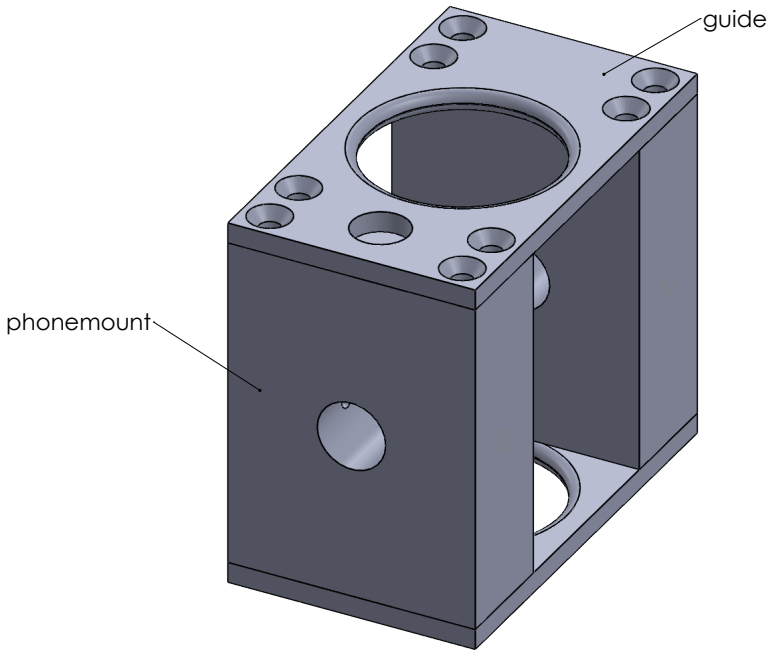

		DIMENSIONS ARE IN INCHES TOLERANCES: FRACTIONAL ± ANGULAR: MACH ± BEND ± TWO PLACE DECIMAL ± THREE PLACE DECIMAL ±		NAME	DATE
			DRAWN		
			CHECKED		
			ENG APPR.		
			MFG APPR.		
		MATERIAL: Aluminum	Q.A.		
			COMMENTS:		
NEXT ASSY	USED ON	FINISH			
APPLICATION		DO NOT SCALE DRAWING			

Gabe Venegas

SIZE	DWG. NO.	REV.
A	TimeofFlight	
SCALE:1:2	WEIGHT:	SHEET 1 OF 1

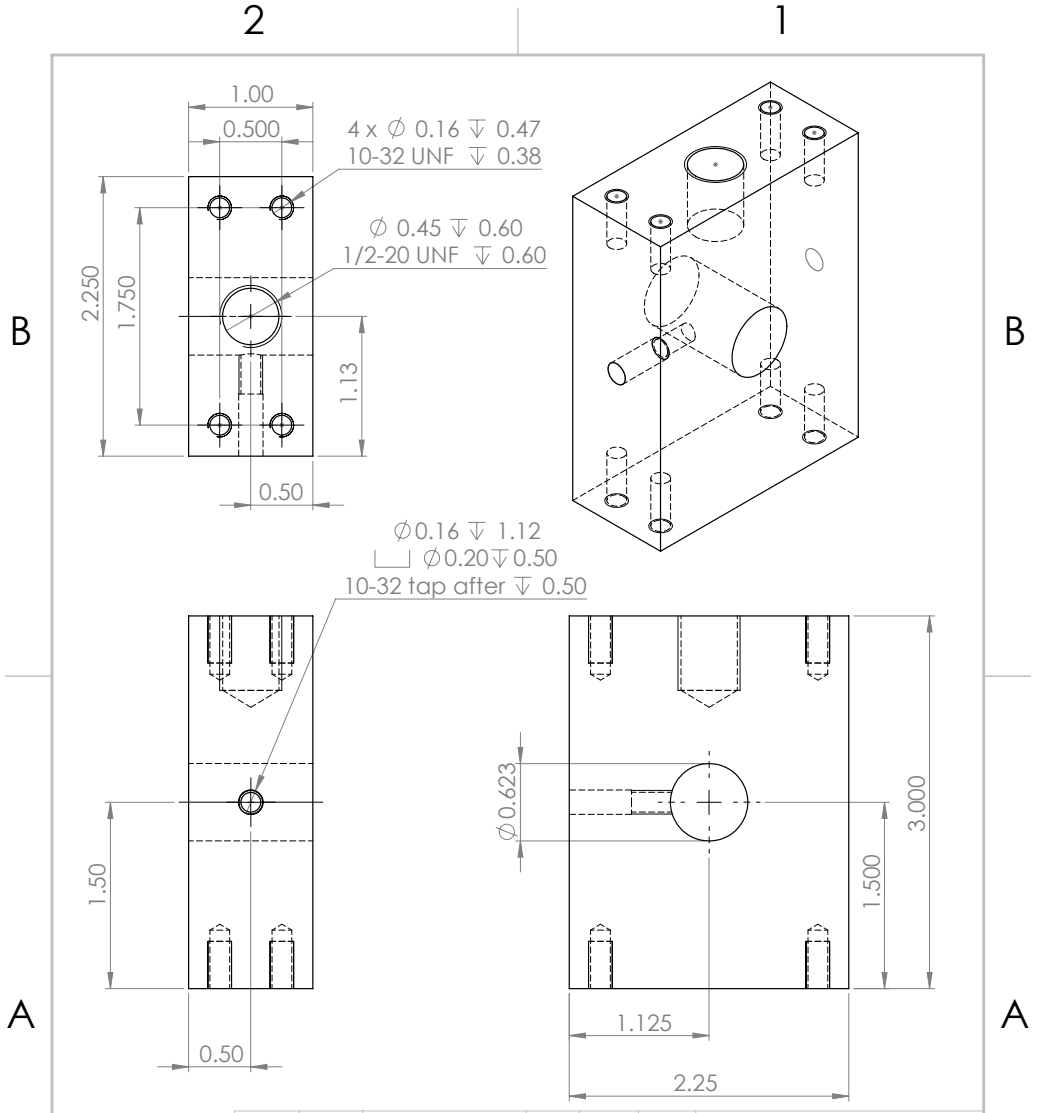
2
1
B
A
1.00
0.500
4 x ∅ 0.16 ↧ 0.47
10-32 UNF ↧ 0.38
∅ 0.45 ↧ 0.60
1/2-20 UNF ↧ 0.60
2.250
1.750
1.13
0.50
⌴ ∅0.20↧0.50
10-32 tap after ↧ 0.50
1.50
∅0.623
3.000
1.500
1.125
2.25
PROPRIETARY AND CONFIDENTIAL
THE INFORMATION CONTAINED IN THIS DRAWING IS THE SOLE PROPERTY OF <COMPANY NAME >. ANY REPRODUCTION IN PART OR AS A WHOLE WITHOUT THE WRITTEN PERMISSION OF <COMPANY NAME> IS PROHIBITED.
DIMENSIONS ARE IN INCHES
TOLERANCES:
FRACTIONAL ±
ANGULAR: MACH ± BEND ±
TWO PLACE DECIMAL ± .01
THREE PLACE DECIMAL ± .005
MATERIAL
Aluminum
FINISH
NEXT ASSY
USED ON
APPLICATION
DO NOT SCALE DRAWING
NAME
DATE
DRAWN
CHECKED
ENG APPR.
MFG APPR.
Q.A.
COMMENTS:
Please make 2
Gabe Venegas
7816326488
ONR2032-1
SIZE
A
DWG. NO.
phonemount1
REV.
SCALE:1:1
WEIGHT:
SHEET 1 OF 1

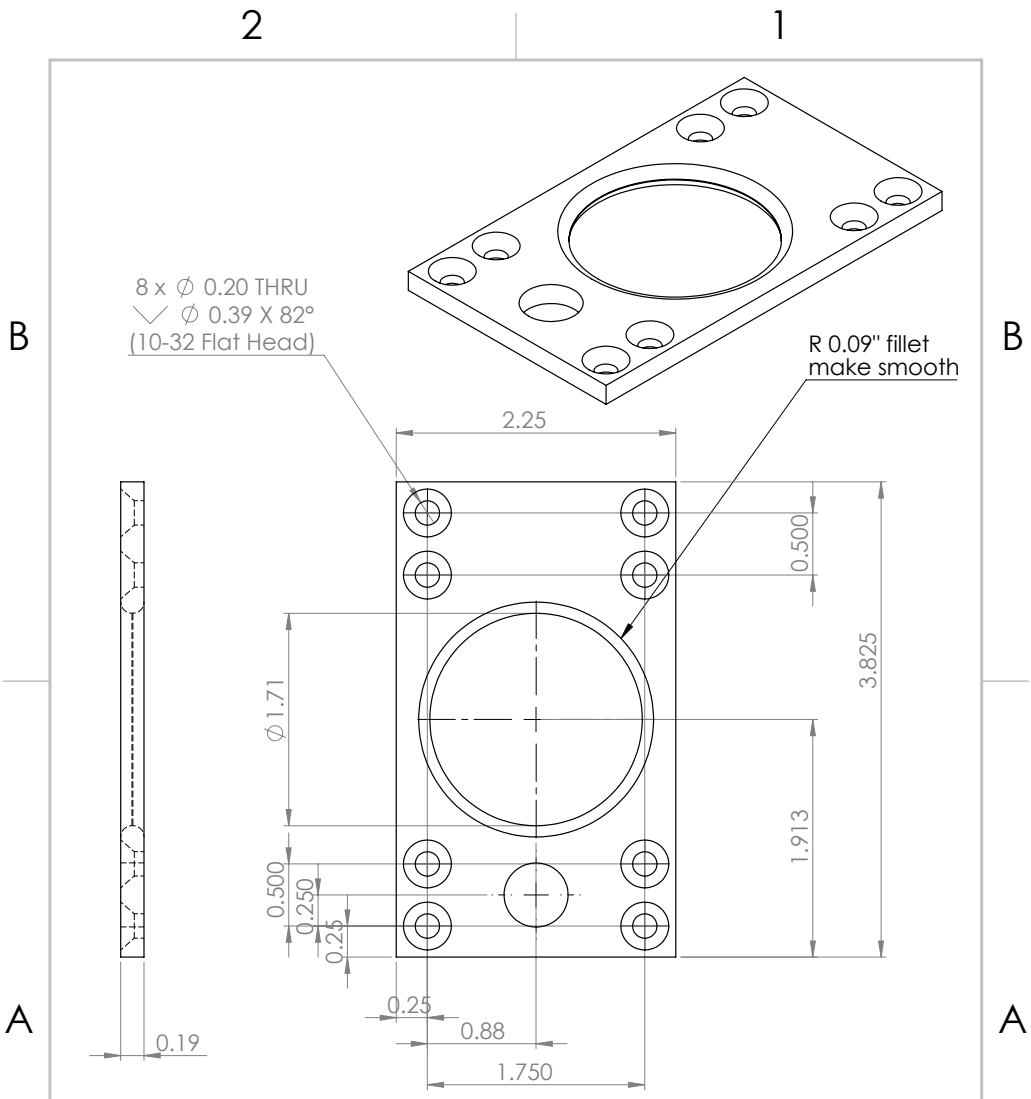

		DIMENSIONS ARE IN INCHES TOLERANCES: FRACTIONAL ± ANGULAR: MACH ± BEND ± TWO PLACE DECIMAL ± .01 THREE PLACE DECIMAL ± .005		NAME	DATE
			DRAWN		
			CHECKED		
			ENG APPR.		
			MFG APPR.		
			Q.A.		
		MATERIAL Aluminum	COMMENTS:		
NEXT ASSY	USED ON	FINISH			
APPLICATION		DO NOT SCALE DRAWING			

PROPRIETARY AND CONFIDENTIAL

THE INFORMATION CONTAINED IN THIS DRAWING IS THE SOLE PROPERTY OF <COMPANY NAME >. ANY REPRODUCTION IN PART OR AS A WHOLE WITHOUT THE WRITTEN PERMISSION OF <COMPANY NAME> IS PROHIBITED.

Please make 2

Gabe Venegas
7816326488
ONR2032-1

SIZE	DWG. NO.	REV.
A	guide	
SCALE:1:1	WEIGHT:	SHEET 1 OF 1

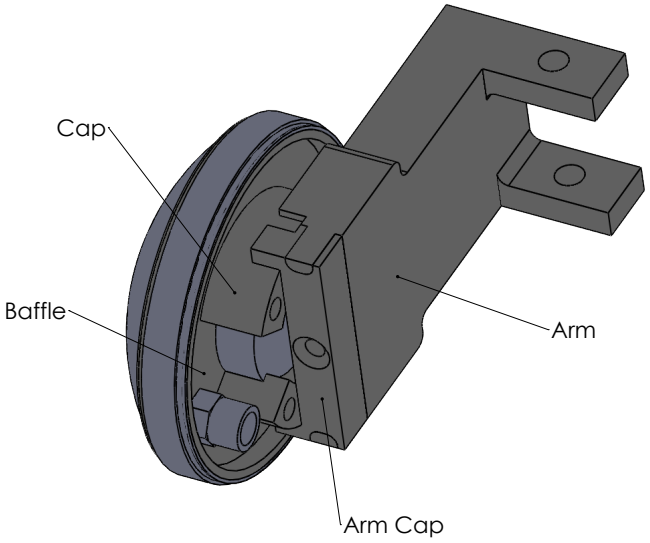

		DIMENSIONS ARE IN INCHES TOLERANCES: FRACTIONAL ± ANGULAR: MACH ± BEND ± TWO PLACE DECIMAL ± THREE PLACE DECIMAL ±		NAME	DATE
			DRAWN		
			CHECKED		
			ENG APPR.		
			MFG APPR.		
		MATERIAL: Aluminum	Q.A.		
			COMMENTS:		
NEXT ASSY	USED ON	FINISH			
APPLICATION		DO NOT SCALE DRAWING			

PROPRIETARY AND CONFIDENTIAL

THE INFORMATION CONTAINED IN THIS DRAWING IS THE SOLE PROPERTY OF <COMPANY NAME >. ANY REPRODUCTION IN PART OR AS A WHOLE WITHOUT THE WRITTEN PERMISSION OF <COMPANY NAME> IS PROHIBITED.

Gabe Venegas

SIZE	DWG. NO.	REV.
A	CARL Assembly	
SCALE:1:1	WEIGHT:	SHEET 1 OF 1

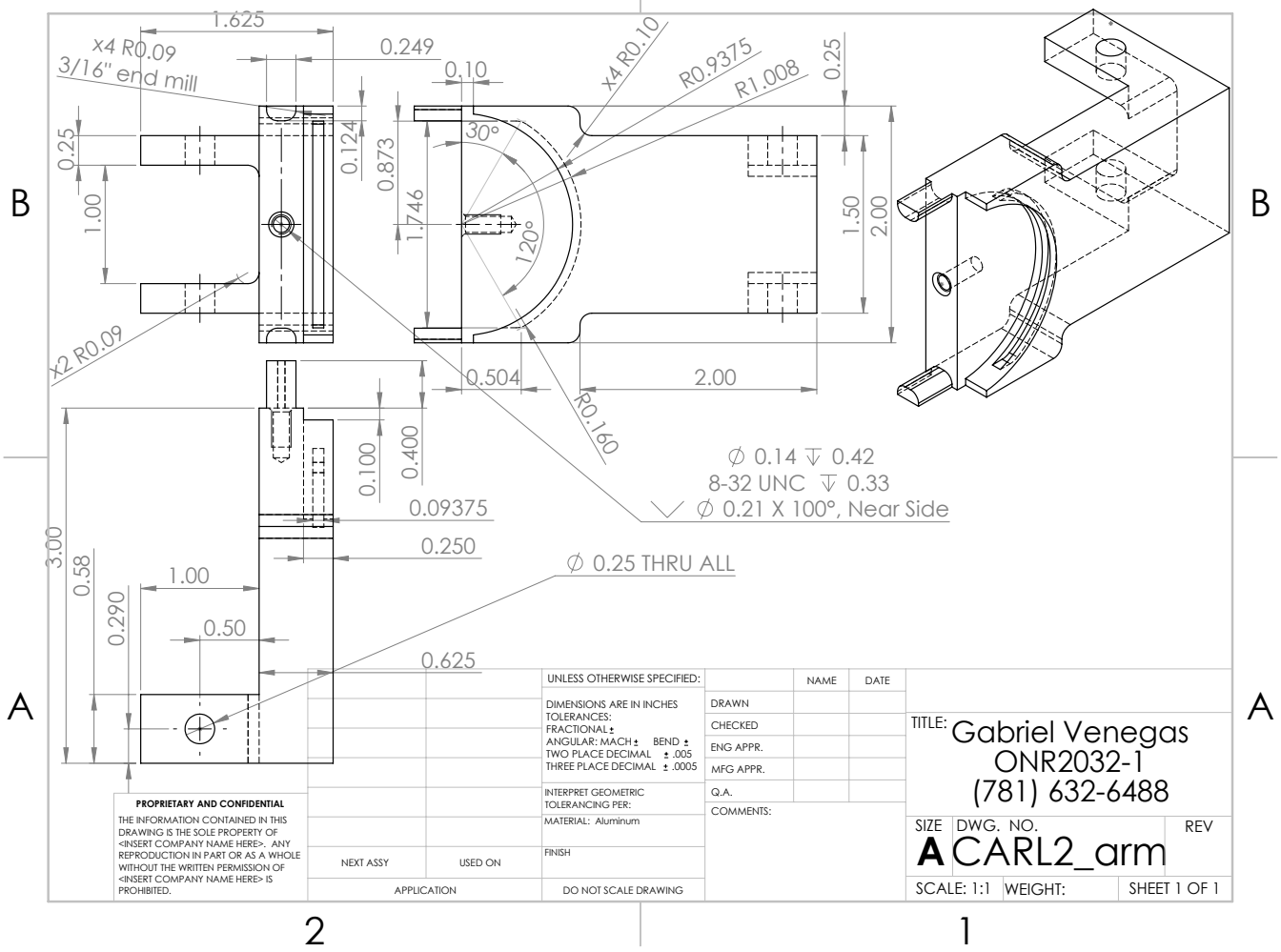
2
1
B
A
1.625
0.249
0.10
x4 R0.09
3/16" end mill
x4 R0.10
R0.9375
R1.008
0.25
0.25
1.00
0.124
0.873
1.746
30°
120°
1.50
2.00
x2 R0.09
0.504
2.00
R0.160
0.100
0.400
∅ 0.14 ↧ 0.42
8-32 UNC ↧ 0.33
∅ 0.21 X 100°, Near Side
0.09375
0.250
∅ 0.25 THRU ALL
3.00
0.58
0.290
1.00
0.50
0.625
UNLESS OTHERWISE SPECIFIED:
DIMENSIONS ARE IN INCHES
TOLERANCES:
FRACTIONAL ±
ANGULAR: MACH ± BEND ±
TWO PLACE DECIMAL ± .005
THREE PLACE DECIMAL ± .0005
INTERPRET GEOMETRIC TOLERANCING PER:
MATERIAL: Aluminum
FINISH
NEXT ASSY
USED ON
APPLICATION
DO NOT SCALE DRAWING
NAME
DATE
DRAWN
CHECKED
ENG APPR.
MFG APPR.
Q.A.
COMMENTS:
PROPRIETARY AND CONFIDENTIAL
THE INFORMATION CONTAINED IN THIS DRAWING IS THE SOLE PROPERTY OF <INSERT COMPANY NAME HERE>. ANY REPRODUCTION IN PART OR AS A WHOLE WITHOUT THE WRITTEN PERMISSION OF <INSERT COMPANY NAME HERE> IS PROHIBITED.
TITLE:
Gabriel Venegas
ONR2032-1
(781) 632-6488
SIZE
A
DWG. NO.
CARL2_arm
REV
SCALE: 1:1
WEIGHT:
SHEET 1 OF 1

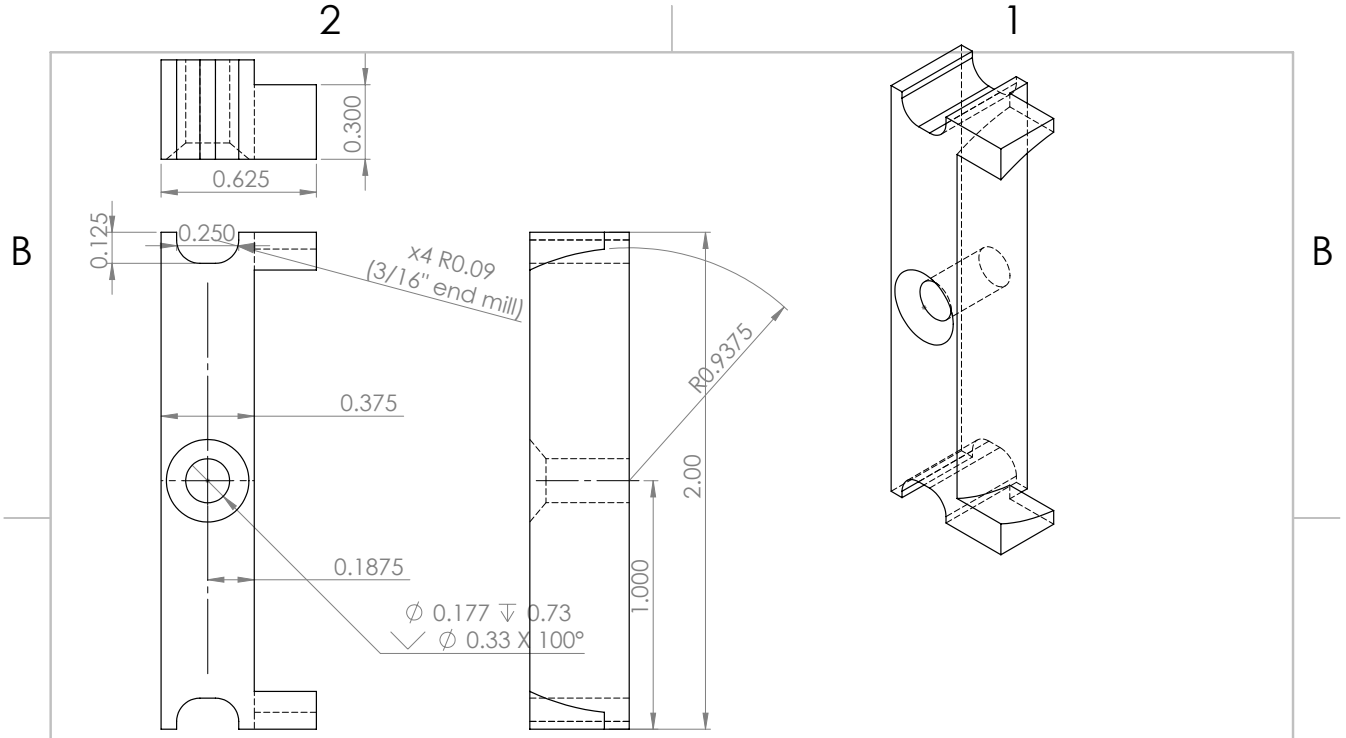

		UNLESS OTHERWISE SPECIFIED:		NAME	DATE
		DIMENSIONS ARE IN INCHES TOLERANCES: FRACTIONAL ± ANGULAR: MACH ± BEND ± TWO PLACE DECIMAL ± .005 THREE PLACE DECIMAL ± .0005	DRAWN		
			CHECKED		
			ENG APPR.		
			MFG APPR.		
		INTERPRET GEOMETRIC TOLERANCING PER:	Q.A.		
		MATERIAL: Aluminum	COMMENTS:		
NEXT ASSY	USED ON	FINISH			
APPLICATION		DO NOT SCALE DRAWING			

TITLE: Gabriel Venegas
ONR2032-1
(781) 632-6488

SIZE	DWG. NO.	REV
A	Arm cap	
SCALE: 2:1	WEIGHT:	SHEET 1 OF 1

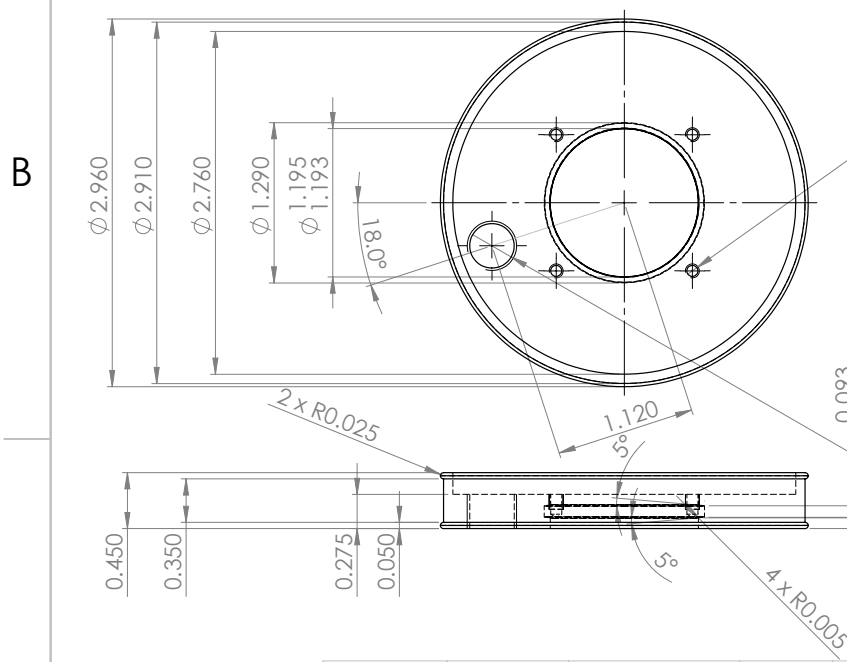

		UNLESS OTHERWISE SPECIFIED:		NAME	DATE
		DIMENSIONS ARE IN INCHES TOLERANCES: FRACTIONAL ± ANGULAR: MACH ± BEND ± TWO PLACE DECIMAL ± THREE PLACE DECIMAL ±	DRAWN		
			CHECKED		
			ENG APPR.		
			MFG APPR.		
		INTERPRET GEOMETRIC TOLERANCING PER:	Q.A.		
		MATERIAL	COMMENTS: Aluminum		
NEXT ASSY	USED ON	FINISH			
APPLICATION		DO NOT SCALE DRAWING			

TITLE:

Gabe Venegas
ONR2032-1
7816326488

SIZE	DWG. NO.	REV
A	CAR_Baffle_nobushing	
SCALE: 1:1	WEIGHT:	SHEET 1 OF 1

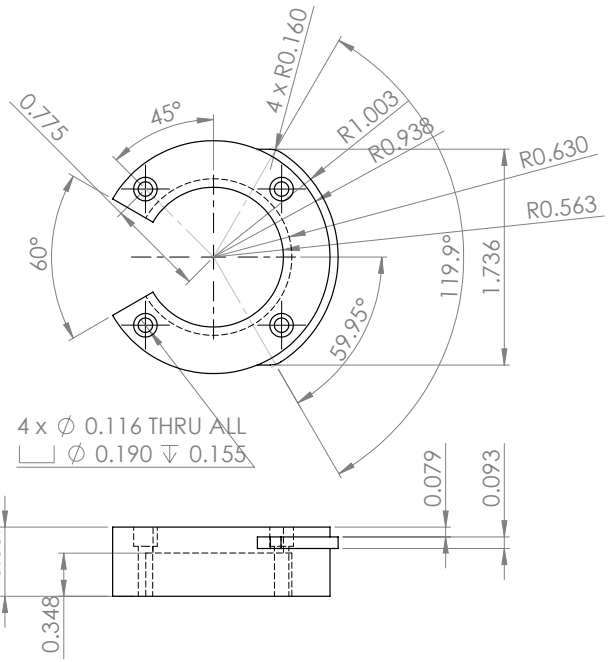

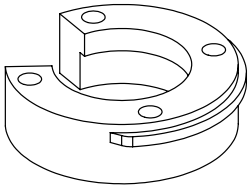

		UNLESS OTHERWISE SPECIFIED:		NAME	DATE
		DIMENSIONS ARE IN INCHES TOLERANCES: FRACTIONAL ± ANGULAR: MACH ± BEND ± TWO PLACE DECIMAL ± THREE PLACE DECIMAL ±	DRAWN		
			CHECKED		
			ENG APPR.		
			MFG APPR.		
		INTERPRET GEOMETRIC TOLERANCING PER:	Q.A.		
		MATERIAL	COMMENTS: Aluminum		
NEXT ASSY	USED ON	FINISH			
APPLICATION		DO NOT SCALE DRAWING			

TITLE:

Gabe Venegas
ONR2032-1
7816326488

SIZE	DWG. NO.	REV
A	CAD_Cap_nobushing	
SCALE: 1:1	WEIGHT:	SHEET 1 OF 1

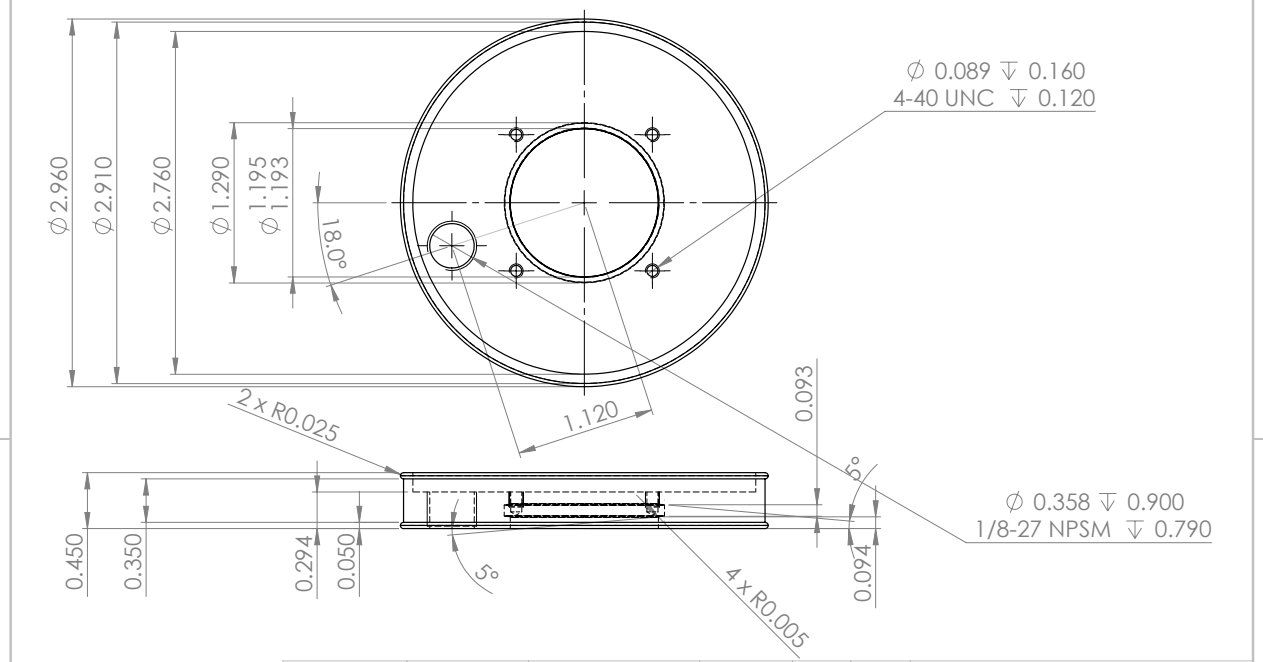

		UNLESS OTHERWISE SPECIFIED:		NAME	DATE
		DIMENSIONS ARE IN INCHES TOLERANCES: FRACTIONAL ± ANGULAR: MACH ± BEND ± TWO PLACE DECIMAL ± THREE PLACE DECIMAL ±	DRAWN		
			CHECKED		
			ENG APPR.		
			MFG APPR.		
		INTERPRET GEOMETRIC TOLERANCING PER:	Q.A.		
		MATERIAL	COMMENTS: Aluminum		
NEXT ASSY	USED ON	FINISH			
APPLICATION		DO NOT SCALE DRAWING			

1 MHz Baffle

TITLE:

Gabe Venegas
ONR2032-1
7816326488

SIZE	DWG. NO.	REV
A	CARL_Baffle_nobushing_1M	
SCALE: 1:1	WEIGHT:	SHEET 1 OF 1

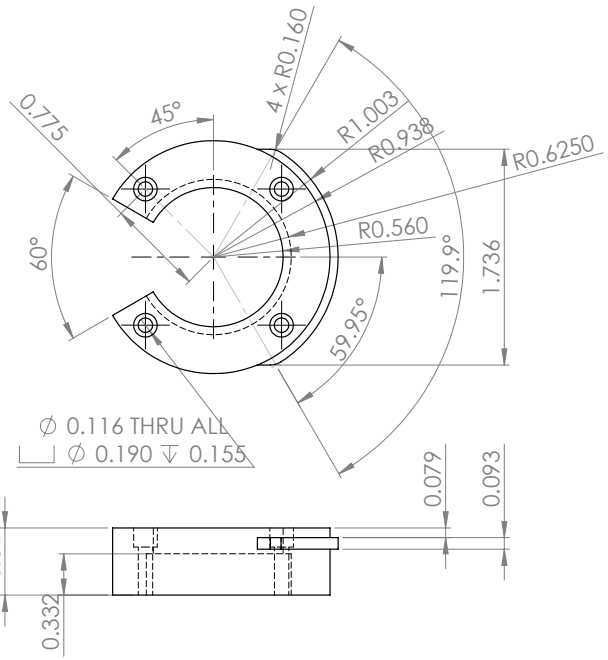

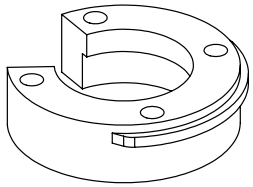

		UNLESS OTHERWISE SPECIFIED:		NAME	DATE
		DIMENSIONS ARE IN INCHES TOLERANCES: FRACTIONAL ± ANGULAR: MACH ± BEND ± TWO PLACE DECIMAL ± THREE PLACE DECIMAL ±	DRAWN		
			CHECKED		
			ENG APPR.		
			MFG APPR.		
		INTERPRET GEOMETRIC TOLERANCING PER:	Q.A.		
		MATERIAL	COMMENTS: Aluminum		
NEXT ASSY	USED ON	FINISH			
APPLICATION		DO NOT SCALE DRAWING			

1 MHz Cap

TITLE:

Gabe Venegas
ONR2032-1
7816326488

SIZE	DWG. NO.	REV
A	CARL_Cap_nobushing_1MH	
SCALE: 1:1	WEIGHT:	SHEET 1 OF 1

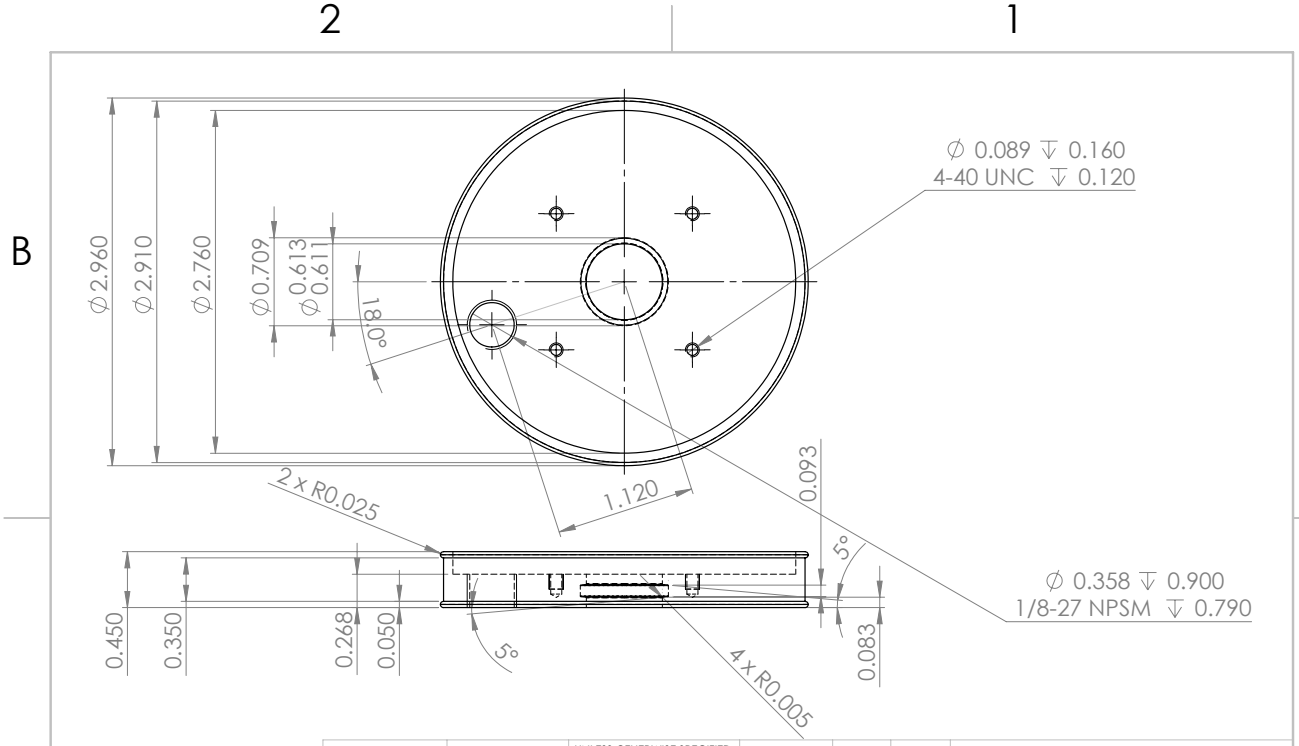

		UNLESS OTHERWISE SPECIFIED:		NAME	DATE
		DIMENSIONS ARE IN INCHES TOLERANCES: FRACTIONAL ± ANGULAR: MACH ± BEND ± TWO PLACE DECIMAL ± THREE PLACE DECIMAL ±	DRAWN		
			CHECKED		
			ENG APPR.		
			MFG APPR.		
		INTERPRET GEOMETRIC TOLERANCING PER:	Q.A.		
		MATERIAL	COMMENTS: Aluminum		
NEXT ASSY	USED ON	FINISH			
APPLICATION		DO NOT SCALE DRAWING			

7.5 MHz Baffle

TITLE:

Gabe Venegas
ONR2032-1
7816326488

SIZE	DWG. NO.	REV
A	CARL_Baffle_nobushing_7.5M	
SCALE: 1:1	WEIGHT:	SHEET 1 OF 1

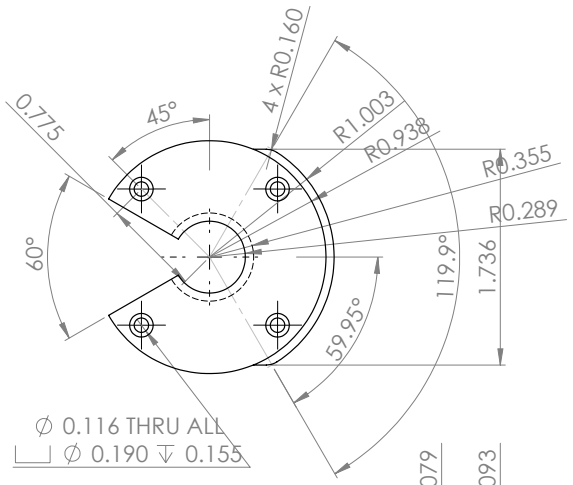

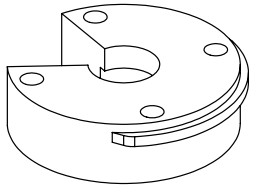

		UNLESS OTHERWISE SPECIFIED:		NAME	DATE
		DIMENSIONS ARE IN INCHES TOLERANCES: FRACTIONAL ± ANGULAR: MACH ± BEND ± TWO PLACE DECIMAL ± THREE PLACE DECIMAL ±	DRAWN		
			CHECKED		
			ENG APPR.		
			MFG APPR.		
		INTERPRET GEOMETRIC TOLERANCING PER:	Q.A.		
		MATERIAL	COMMENTS: Aluminum		
NEXT ASSY	USED ON	FINISH			
APPLICATION		DO NOT SCALE DRAWING			

7.5 MHz Cap

TITLE:

Gabe Venegas
ONR2032-1
7816326488

SIZE	DWG. NO.	REV
A		

SCALE: 1:1	WEIGHT:	SHEET 1 OF 1

Bibliography

[1] T. S. Garrison, *Oceanography: An Invitation to Marine Science*. Cengage Learning, Independence, 2012.

[2] D. A. Ross, *Introduction to Oceanography*. Harper Colins, New York, 1995.

[3] D. Pauly, V. Christensen, S. Guénette, T. J. Pitcher, U. R. Sumaila, C. J. Walters, R. Watson, and D. Zeller, "Towards sustainability in world fisheries," *Nature*, vol. 418, p. 689, 2002.

[4] M. Waycott, C. M. Duarte, T. J. B. Carruthers, R. J. Orth, W. C. Dennison, and S. Olyarnik, "Accelerating loss of seagrasses across the globe threatens coastal ecosystems," *Proc. Natl. Acad. Sci. U.S.A.*, vol. 106, pp. 12377–12381, 2009.

[5] D. C. Donato, J. B. Kauffman, D. Murdiyarso, S. Kurnianto, M. Stidham, and M. Kanninen, "Mangroves among the most carbon-rich forests in the tropics," *Nature Geoscience*, vol. 4, p. 293, 2011.

[6] C. M. Duarte, J. J. Middelburg, and N. Caraco, "Major role of marine vegetation on the oceanic carbon cycle," *Biogeosciences*, vol. 2, pp. 1–8, 2005.

[7] L. Pendleton, D. C. Donato, B. C. Murray, S. Crooks, W. A. Jenkins, S. Sifleet, C. Craft, J. W. Fourqurean, J. B. Kauffman, N. Marbà, *et al.*, "Estimating global blue carbon emissions from conversion and degradation of vegetated coastal ecosystems," *PLOS ONE*, vol. 7, p. e43542, 2012.

[8] H. Viders, *Marine Conservation for the 21st Century*. Best Publishing Company, West Palm Beach, 1995.

[9] D. R. Jackson and M. D. Richardson, *High-Frequency Seafloor Acoustics*. New York: Springer, 1991.

[10] C. K. Wentworth, "A scale of grade and class terms for clastic sediments," *J. Geol.*, vol. 30, pp. 377–392, 1922.

[11] R. H. Bennett, W. R. Bryant, and M. H. Hulbert, *Microstructure of Fine-Grained Sediments: From Mud to Shale*. New York: Springer-Verlag, 1991. Frontiers in Sedimentary Geology.

[12] J. F. Lynch, G. Jin, R. Pawlowicz, D. Ray, A. J. Plueddemann, C.-S. Chiu, J. H. Miller, R. H. Bourke, A. R. Parsons, and R. Muench, "Acoustic travel-time perturbations due to shallow-water internal waves and internal tides in the Barents Sea Polar Front: Theory and experiment," *J. Acoust. Soc. Am.*, vol. 99, pp. 803–821, 1996.

[13] D. B. Reeder, "Field observation of low-to-mid-frequency acoustic propagation characteristics of an estuarine salt wedge," *J. Acoust. Soc. Am.*,

vol. 139, pp. 21–29, 2016.

[14] E. L. Hamilton, "Prediction of in-situ acoustic and elastic properties of marine sediments," *Geophysics*, vol. 36, pp. 266–284, 1971.

[15] D. C. Rhoads, "Organism-sediment relationships on the muddy seafloor," *Oceanography and Mar. Biol. Annu. Rev.*, vol. 12, pp. 263–300, 1974.

[16] W. T. Wood, K. M. Martin, W. Jung, and J. Sample, "Seismic reflectivity effects from seasonal seafloor temperature variation," *Geophys. Res. Lett.*, vol. 41, pp. 6826–6832, 2014.

[17] G. R. Venegas, P. S. Wilson, and J. D. Sagers, "Laboratory measurements of reflection coefficient from a water-mud interface after varying bottom water salinity," vol. 29, p. 070001, ASA, 2016.

[18] E. L. Hamilton, "Low sound velocities in high-porosity sediments," *J. Acoust. Soc. Am.*, vol. 28, pp. 16–19, 1956.

[19] E. L. Hamilton, "Elastic properties of marine sediments," *J. Geophys. Res.*, vol. 76, pp. 579–604, 1971.

[20] G. Shumway, "Sound speed and absorption studies of marine sediments by a resonance method—Part I," *Geophysics*, vol. 25, pp. 451–467, 1960.

[21] G. Shumway, "Sound speed and absorption studies of marine sediments by a resonance method—Part II," *Geophysics*, vol. 25, pp. 659–682, 1960.

[22] R. Folk and W. Ward, "Brazos River Bar: A study of the significance of grain size parameters," *J. Sed. Petr.*, vol. 27, pp. 3–26, 1957.

[23] M. A. Biot, "Theory of propagation of elastic waves in a fluid-saturated porous solid. I. Low-frequency range," *J. Acoust. Soc. Am.*, vol. 28, pp. 168–178, 1956.

[24] M. A. Biot, "Theory of propagation of elastic waves in a fluid-saturated porous solid. II. Higher frequency range," *J. Acoust. Soc. Am.*, vol. 28, pp. 179–191, 1956.

[25] R. D. Stoll, *Sediment Acoustics*. Springer, New York, 1989.

[26] K. L. Williams, "An effective density fluid model for acoustic propagation in sediments derived from Biot theory," *J. Acoust. Soc. Am.*, vol. 110, pp. 2276–2281, 2001.

[27] N. P. Chotiros, *Acoustics of the Seabed as a Poroelastic Medium*. Springer Nature, Switzerland, 1989.

[28] K. Lee, E. Park, and W. Seong, "High frequency measurements of sound speed and attenuation in water-saturated glass-beads of varying size," *J. Acoust. Soc. Am.*, vol. 126, pp. EL28–EL33, 2009.

[29] M. Kimura, "Velocity dispersion and attenuation in granular marine sediments: Comparison of measurements with predictions using acoustic models," *J. Acoust. Soc. Am.*, vol. 129, pp. 3544–3561, 2011.

[30] J. P. Sessarego and R. Guillermin, "High-frequency sound speed, attenuation, and reflection measurements using water-saturated glass beads of different sizes," *IEEE J. Ocean. Eng.*, vol. 37, pp. 507–515, 2012.

[31] K. L. Williams, D. R. Jackson, E. I. Thorsos, D. Tang, and S. G. Schock, "Comparison of sound speed and attenuation measured in a sandy sediment to predictions based on the Biot theory of porous media," *IEEE J. Ocean. Eng.*, vol. 27, pp. 413–428, 2002.

[32] A. D. Pierce, W. L. Siegmann, and E. M. Brown, "Characterization of mud sediments using the frequency dependence of phase velocity and attenuation of compressional waves," *Proc. Mtgs. Acoust.*, vol. 142, pp. 2591–2591, 2017.

[33] Y. Furukawa, J. L. Watkins, J. Kim, K. J. Curry, and R. H. Bennett, "Aggregation of montmorillonite and organic matter in aqueous media containing artificial seawater," *Geochem. Trans.*, vol. 10, pp. 1–11, 2009.

[34] K. J. Curry, R. H. Bennett, L. M. Mayer, A. Curry, M. Abril, P. M. Biesiot, and M. H. Hulbert, "Direct visualization of clay microfabric signatures driving organic matter preservation in fine-grained sediment," *Geochim. Cosmochim. Acta*, vol. 71, pp. 1709–1720, 2007.

[35] W. G. Zhang and G. G. Gawarkiewicz, "Dynamics of the direct intrusion of gulf stream ring water onto the mid-atlantic bight shelf," *Geophysical Research Letters*, vol. 42, pp. 7687–7695, 2015.

[36] P. C. Mangelsdorf, "Salinity measurements in estuaries," in *Estuaries* (G. H. Lauff, ed.), pp. 71–79, Am. Assoc. Adv. Sci. pub. no. 83, Washington DC, 1967.

[37] W. J. Toulis, "Theory of a resonance method to measure the acoustic properties of sediments," *Geophysics*, vol. 21, pp. 299–304, 1956.

[38] P. S. Wilson, A. H. Reed, J. C. Wilbur, and R. A. Roy, "Evidence of dispersion in an artificial water-saturated sand sediment," *J. Acoust. Soc. Am.*, vol. 121, pp. 824–832, 2007.

[39] R. S. Winokur and S. Chanesman, "A pulse method for sound speed measurements in cored ocean bottom sediments (no. im-66-5," tech. rep., Naval Oceanographic Office, NSTL Station, MS, 1966.

[40] M. D. Richardson, "Spatial variability of surficial shallow water sediment geoacoustic properties," in *Ocean Seismo-Acoustics: Low Frequency Underwater Acoustics*, pp. 527–536, Plenum Press, New York, 1986.

[41] E. Mcleod, G. L. Chmura, S. Bouillon, R. Salm, M. Björk, C. M. Duarte, C. E. Lovelock, W. H. Schlesinger, and B. R. Silliman, "A blueprint for blue carbon: toward an improved understanding of the role of vegetated coastal habitats in sequestering CO_2," *Front. Ecol. Environ.*, no. 10, pp. 552–560, 2011.

[42] O. Serrano, P. Lavery, C. M. Duarte, G. A. Kendrick, A. M. Calfat, P. H. York, A. D. Steven, and P. I. Macreadie, "Can mud (silt and

clay) concentration be used to predict soil organic carbon content within seagrass ecosystems?," *Biogeosciences*, vol. 13, pp. 4915–4926, 2016.

[43] M. Dahl, D. Deyanova, S. Gütschow, M. E. Asplund, L. D. Lyimo, V. Karamfilov, R. Santos, M. Björk, and M. Gullström, "Sediment properties as important predictors of carbon storage in Zostera marina meadows: a comparison of four european areas," *PLOS ONE*, vol. 11, p. e0167493, 2016.

[44] R. J. Urick, *Principles of Underwater Sound for Engineers*. McGraw-Hill, New York, 1967.

[45] S. D. Rajan and G. V. Frisk, "Seasonal variations of the sediment compressional wave-speed profile in the Gulf of Mexico," *J. Acoust. Soc. Am.*, vol. 91, pp. 127–135, 1992.

[46] D. R. Jackson and M. D. Richardson, "Seasonal temperature gradients within a sandy seafloor: Implications for acoustic propagation and scattering," *Proc. Inst. Acoust. Conf.*, vol. 23, pp. 361–368, 2001.

[47] L. Brekhovskikh, *Waves in Layered Media*. Elsevier, Amsterdam, 2012.

[48] "Summary of data treatment for the International one atmosphere equation of state for seawater," Tech. Rep. 38, UNESCO Tech. Pap. in Mar. Sci., 1981. in press.

[49] A. B. Coppens, "Simple equations for the speed of sound in Neptunian waters," *J. Acoust. Soc. Am.*, vol. 69, pp. 862–863, 1981.

[50] M. S. Ballard and K. M. Lee, "Examining the effects of microstructure on geoacoustic parameters in fine-grained sediments," *J. Acoust. Soc. Am.*, vol. 140, pp. 1548–1557, 2016.

[51] J. D. Sagers, M. R. Haberman, and P. S. Wilson, "Ultrasonic measurements of the reflection coefficient at a water/polyurethane foam interface," *J. Acoust. Soc. Am.*, vol. 134, pp. EL271–EL275, 2013.

[52] T. P. Pialucha, "The reflection coefficient from interface layers in NDT of adhesive joints," *Ph.D. thesis, University of London, UK*, 1992.

[53] Y. Cencel and A. Ghajar, *Heat and Mass Transfer: Fundamentals and Applications*. Tata McGraw-Hill, New Delhi, 2011.

[54] C. J. Fell and H. P. Hutchison, "Diffusion coefficients for sodium and potassium chlorides in water at elevated temperatures," *J. Chem. Eng. Data*, vol. 16, pp. 427–429, 1971.

[55] P. Grathwohl, *Diffusion in Natural Porous Media*, vol. 1. Springer Science & Business Media, Berlin/Heidelberg, 2012.

[56] R. D. Stoll, "Acoustic waves in ocean sediments," *Geophysics*, vol. 42, pp. 715–725, 1977.

[57] E. L. Cussler, *Diffusion: Mass Transfer in Fluid Systems*. Cambridge University Press, Cambridge, 2009.

[58] R. H. Bennett, W. R. Bryant, and G. H. Keller, "Clay fabric and geotechnical properties of selected submarine sediment cores from the Mississippi Delta," *Natl. Oceanic Atmos. Adm. Prof. Pap.*, vol. 9, pp. 1–86, 1977.

[59] J. K. Enderby and L. J. Thompson, "Overpressured marine sediments. Volume 3: Thermal conductivity, electrical resistivity, and permeability of saturated sediment at various porosities," Tech. Rep. DI-14-08-0001-17289, Texas A&M Res. Found., College Station, TX USA, 1981.

[60] R. H. Bennett, K. M. Fischer, D. L. Lavoie, W. R. Bryant, and R. Rezak, "Porometry and fabric of marine clay and carbonate sediments: Determinants of permeability," *Mar. Geol.*, vol. 89, pp. 127–152, 1989.

[61] P. C. Hines, J. C. Osler, J. G. Scrutton, and L. J. Halloran, "Time-of-flight measurements of acoustic wave speed in a sandy sediment at 0.6–20 kHz," *IEEE J. Ocean. Eng.*, vol. 35, pp. 502–515, 2010.

[62] E. L. Hamilton and R. T. Bachman, "Sound velocity and related properties of marine sediments," *J. Acoust. Soc. Am.*, vol. 72, pp. 1891–1904, 1982.

[63] J.-X. Zhou, X.-Z. Zhang, and D. Knobles, "Low-frequency geoacoustic model for the effective properties of sandy seabottoms," *J. Acoust. Soc. Am.*, vol. 125, pp. 2847–2866, 2009.

[64] M. A. Zimmer, L. D. Bibee, and M. D. Richardson, "Measurement of the frequency dependence of the sound speed and attenuation of seafloor sands from 1 to 400 kHz," *IEEE J. Ocean. Eng.*, vol. 35, pp. 538–557, 2010.

[65] T. F. Argo, *Laboratory measurements of sound speed and attenuation of water-saturated granular sediments.* Ph.D. dissertation, Univ. of Texas at Austin, Austin, TX, 2012.

[66] H. R. A. Mallock, "The damping of sound by frothy liquids," *Proc. R. Soc. Lond. A*, vol. 84, pp. 391–395, 1910.

[67] A. B. Wood, *A Textbook of Sound.* G. Bell and Sons, London, 1941.

[68] K. L. Williams, "Adding thermal and granularity effects to the effective density fluid model," *J. Acoust. Soc. Am.*, vol. 133, pp. EL431–EL437, 2013.

[69] A. A. Atchley and A. Prosperetti, "The crevice model of bubble nucleation," *J. Acoust. Soc. Am.*, vol. 86, pp. 1065–1084, 1989.

[70] G. Shumway, "A resonant chamber method for sound speed velocity and attenuation measurements in sediments," *Geophysics*, vol. 21, pp. 305–319, 1956.

[71] C. A. Greene, P. S. Wilson, and R. B. Coffin, "Acoustic determination of methane hydrate dissociation pressures," *Proc. 7th Int. Conf. Gas Hydrates*, pp. 1–11, 2011.

[72] E. Silberman, "Sound velocity and attenuation in bubbly mixtures measured in standing wave tubes," *J. Acoust. Soc. Am.*, vol. 29, pp. 925–933, 1957.

[73] K. M. Lee, K. T. Hinojosa, M. S. Wochner, T. F. Argo, P. S. Wilson, and R. S. Mercier, "Sound propagation in water containing large tethered spherical encapsulated gas bubbles with resonance frequencies in the 50 Hz to 100 Hz range," *J. Acoust. Soc. Am.*, vol. 130, pp. 3325–3332, 2011.

[74] C. N. Dolder and P. S. Wilson, "Using one-dimensional waveguide resonators to measure phase velocities in bubbly liquids," *J. Acoust. Soc. Am.*, vol. 141, pp. 2832–2839, 2017.

[75] P. S. Wilson and K. H. Dunton, "Laboratory investigation of the acoustic response of seagrass tissue in the frequency band 0.5–2.5 kHz," *J. Acoust. Soc. Am.*, vol. 125, pp. 1951–1959, 2009.

[76] C. J. Wilson, P. S. Wilson, C. A. Greene, and K. H. Dunton, "Seagrass leaves in 3-D: Using computed tomography and low-frequency acoustics to investigate the material properties of seagrass tissue," *J. Exp. Mar. Biol. Ecol.*, vol. 395, pp. 128–134, 2010.

[77] C. J. Wilson, P. S. Wilson, and K. H. Dunton, "Assessing the low frequency acoustic characteristics of *Macrocystis pyrifera*, *Egregia menziessi*, and *Laminaria solidungula*," *J. Acoust. Soc. Am.*, vol. 133, pp. 3819–3826, 2013.

[78] J. R. Johnson, G. R. Venegas, P. S. Wilson, and J.-P. Hermand, "Low frequency acoustic properties of posidonia oceanica seagrass leaf blades," *J. Acoust. Soc. Am.*, vol. 141, pp. EL555–EL560, 2017.

[79] J. R. Johnson, G. R. Venegas, P. S. Wilson, and J.-P. Hermand, "Measurement of low-frequency tissue response of the seagrass posidonia oceanica," *J. Acoust. Soc. Am.*, vol. 141, pp. EL433–EL438, 2017.

[80] J. Van Vleck and D. Middleton, "A theoretical comparison of the visual, aural, and meter reception of pulsed signals in the presence of noise," *J. Appl. Phy.*, vol. 17, pp. 940–971, 1946.

[81] H. Ramp and E. Wingrove, "Principles of pulse compression," *IRE Trans. Mil. Electron.*, pp. 109–116, 1961.

[82] J. S. Bendat and A. G. Piersol, *Engineering Applications of Correlation and Spectral Analysis*. Wiley-Interscience, New York, 1980.

[83] V. A. Del Grosso and C. W. Mader, "Speed of sound in pure water," *J. Acoust. Soc. Am.*, vol. 52, pp. 1142–1446, 1972.

[84] F. A. L. Dullien, "Single phase flow through porous media and pore structure," *Chem. Eng. J.*, vol. 10, pp. 1–34, 1975.

[85] M. K. Sen and P. L. Stoffa, *Global Optimization Methods in Geophysical Inversion*. Cambridge University Press, Cambridge, 2013.

[86] L. D. Lafleur and F. D. Shields, "Low-frequency propagation modes in a liquid-filled elastic tube waveguide," *J. Acoust. Soc. Am.*, vol. 97, pp. 1435–1445, 1995.

[87] M. Mota, J. A. Teixeira, W. R. Bowen, and A. Yelshin, "Binary spherical particle mixed beds: Porosity and permeability relationship measurement," *Trans. Filt. Soc.*, vol. 1, pp. 101–106, 2001.

[88] K. Klusácek and P. Schneider, "Effect of size and shape of catalyst microparticles on pellet pore structure and effectiveness," *Chem. Eng. Sci.*, vol. 36, pp. 53–527, 1981.

[89] N. E. Olague, D. M. Smith, and M. Ciftcioglu, "Knedsen diffusion in ordered sphere packings," *AIChE J.*, vol. 34, pp. 1907–1909, 1988.

[90] E. Hamilton, G. Shumway, H. Menard, and C. Shipek, "Acoustic and other physical properties of shallow-water sediments off San Diego," *J. Acoust. Soc. Am.*, vol. 28, pp. 1–14, 1956.

[91] A. S. Laughton, "Sound propagation in compacted ocean sediments," *Geophysics*, vol. 22, pp. 233–260, 1957.

[92] G. Shumway, "Sound velocity vs. temperature in water-saturated sediments," *Geophysics*, vol. 23, pp. 494–505, 1958.

[93] J. D. Bennell, *Acoustic properties of marine sediments.* PhD thesis, University of Wales (UCNW, Bangor: Physical Oceanography), 1979.

[94] R. Carbo and A. Molero, "Temperature dependence of high frequency sound attenuation in porous marine sediments," *Acust. Acta Acust.*, vol. 88, pp. 190–194, 2002.

[95] M. J. Buckingham and M. D. Richardson, "On tone-burst measurements of sound speed and attenuation in sandy marine sediments," *IEEE J. Ocean. Eng.*, vol. 27, pp. 429–453, 2002.

[96] C. Fuller and F. J. Fahy, "Characteristics of wave propagation and energy distributions in cylindrical elastic shells filled with fluid," *Journal of sound and vibration*, vol. 81, pp. 501–518, 1982.

[97] G. R. Venegas, P. S. Wilson, K. M. Lee, M. S. Ballard, A. R. McNeese, and K. M. Dorgan, "Core and Resonance Logger (CARL) measurements of fine-grained sediments containing infauna," *Proc. Mtgs. Acoust.*, vol. 31, p. 005001, 2017.

[98] B. E. Treeby, B. T. Cox, E. Z. Zhang, S. K. Patch, and P. C. Beard, "Measurement of broadband temperature-dependent ultrasonic attenuation and dispersion using photoacoustics," *IEEE Trans. Ultrason. Ferroelect. Freq. Control*, vol. 56, pp. 1666–1676, 2009.

[99] K. R. Waters, M. S. Hughes, J. Mobley, G. H. Brandenburger, and J. G. Miller, "On the applicability of Kramers–Krönig relations for ultrasonic attenuation obeying a frequency power law," *J. Acoust. Soc. Am.*, vol. 108, pp. 556–563, 2000.

[100] M. J. Buckingham, "Compressional and shear wave properties of marine sediments: Comparisons between theory and data," *J. Acoust. Soc. Am.*, vol. 117, pp. 137–152, 2005.

[101] E. Hamilton, H. Bucker, D. Keir, and J. Whitney, "Velocities of compressional and shear waves in marine sediments determined in situ from a research submersible," *J. Geophys. Res.*, vol. 75, pp. 4039–4049, 1970.

[102] K. M. Lee, G. R. Venegas, M. S. Ballard, P. S. Wilson, and K. M. Dorgan, "Acoustics of biologically active marine sediments," *Proc. Mtgs. Acoust.*, vol. 33, p. 005003, 2018.

[103] M. S. Ballard, K. M. Lee, J. D. Sagers, G. R. Venegas, A. R. McNeese, A. F. Rahman, J. T. Dubin, and P. S. Wilson, "Measurements and modeling of acoustic propagation in a seagrass meadow," *Proc. Mtgs. Acoust.*, vol. 33, p. 005002, 2018.

[104] G. R. Venegas, A. Aslan, I. M. Hinson, A. F. Rahman, K. M. Lee, M. S. Ballard, J. D. Sagers, A. R. McNeese, J. T. Dubin, and P. S. Wilson, "Effect of carbon content on sound speed and attenuation of sediments in seagrass meadows (A)," *J. Acoust. Soc. Am.*, vol. 143, p. 1797, 2018.

[105] G. R. Venegas, K. M. Lee, M. S. Ballard, P. S. Wilson, and A. F. Rahman, "Geoacoustic properties of seagrass-bearing sediments (A)," *J. Acoust. Soc. Am.*, vol. 144, p. 1844, 2018.

[106] J. W. Fourqurean, C. M. Duarte, H. Kennedy, N. Marb, M. Holmer, M. A. Mateo, E. T. Apostolaki, G. A. Kendrick, D. Krause-Jensen, K. J. McGlathery, and O. Serrano, "Seagrass ecosystems as a globally significant carbon stock," *Nat. Geosci.*, vol. 5, pp. 505–509, 2012.

[107] G. Chmura, F. Short, D. Torio, P. Arroya-Mora, P. Fajardo, M. Hatvany, and L. van Ardenne, "North America's blue carbon: assessing seagrass, salt marsh and mangrove carbon sinks a final report," tech. rep., Montreal, Canada: Commission for Environmental Cooperation, 2014.

[108] W. Brutsaert and J. N. Luthin, "The velocity of sound in soils near the surface as a function of the moisture content," *J. Geophys. Res.*, vol. 69, pp. 643–652, 1964.

[109] G. C. Topp, J. Davis, and A. P. Annan, "Electromagnetic determination of soil water content: Measurements in coaxial transmission lines," *Water Resour. Res.*, vol. 16, pp. 574–582, 1980.

[110] I. Flammer, A. Blum, A. Leiser, and P. Germann, "Acoustic assessment of flow patterns in unsaturated soil," *J. Appl. Geophys.*, vol. 46, pp. 115–128, 2001.

[111] J. A. Doolittle and E. C. Brevik, "The use of electromagnetic induction techniques in soils studies," *Geoderma*, vol. 223, pp. 33–45, 2014.

[112] M. E. Rohr, C. Bostrom, P. Canal-Vergés, and M. Holmer, "Blue carbon stocks in Baltic Sea eelgrass (*Zostera marina*) meadows," *Biogeosciences*,

vol. 13, pp. 6139–6153, 2016.

[113] D. Marion, A. Nur, H. Yin, and D. Han, "Compressional velocity and porosity in sand-clay mixtures," *Geophysics*, vol. 57, pp. 554–563, 1992.

[114] A. D. Pierce, W. L. Siegmann, and E. Brown, "Suspension theory for the effect of silt particles on attenuation of compressional waves in marine mud sediments," *Proc. Mtgs. Acoust.*, vol. 29, p. 005003, 2016.

[115] E. M. Brown, A. D. Pierce, and W. L. Siegmann, "Influence of sand/silt particle size distributions on compressional wave attenuation in marine mud," *Proc. Mtgs. Acoust.*, vol. 30, p. 005004, 2017.

[116] B. Javor, *Hypersaline Environments: Microbiology and Biogeochemistry*. New York: Springer-Verlag, 1989.

[117] C. P. Onuf, "Laguna Madre," in *Seagrass Status and Trends in the Northern Gulf of Mexico: 1940–2002: U.S. Geological Survey Scientific Investigations Report 2006-5287*, p. 267, 2007.

[118] U. DOE, "Carbon cycling and biosequestration: Report from the March 2008 Workshop," tech. rep., DOE/SC-108, US Department of Energy Office of Science, 2008.

[119] J. Howard, S. Hoyt, K. Isensee, M. Telszewski, E. Pidgeon, *et al.*, "Coastal blue carbon: Methods for assessing carbon stocks and emissions factors in mangroves, tidal salt marshes, and seagrasses," pp. 58–62, 2014.

[120] H. Dogan, P. R. White, and T. G. Leighton, "Acoustic wave propagation in gassy porous marine sediments: The rheological and the elastic effects," *J. Acoust. Soc. Am.*, vol. 141, pp. 2277–2288, 2017.

[121] K. M. Lee, M. S. Ballard, A. R. McNeese, and P. S. Wilson, "Sound speed and attenuation measurements within a seagrass meadow from the water column into the seabed," *J. Acoust. Soc. Am.*, vol. 141, pp. EL402–EL406, 2017.

[122] H. Yang and W. Seong, "High frequency compressional wave speed and attenuation measurements in water-saturated granular media with unimodal and bimodal grain size distributions," *J. Acoust. Soc. Am.*, vol. 143, pp. 659–665, 2018.

[123] G. Mavko, T. Mukerji, and J. Dvorkin, *The Rock Physics Handbook: Tools for Seismic Analysis of Porous Media*. Cambridge University Press, Cambridge, 2009.

[124] M. Ryżak and A. Bieganowski, "Methodological aspects of determining soil particle-size distribution using the laser diffraction method," *J. Plant Nutr. Soil Sci.*, vol. 174, pp. 624–633, 2011.

[125] A. L. Greene, "Applications of side scan and parametric echosounders for mapping shallow seagrass habitats and their associated organic carbon," master's thesis, School of Earth, Environ., Marine Sci., The Univ. of Texas Rio Grande Valley, 2017. Order No. 10263707.

[126] L. M. Mayer, "Extent of coverage of mineral surfaces by organic matter in marine sediments," *Geochim. Cosmochim. Acta*, vol. 63, pp. 207–215, 1999.

[127] L. M. Mayer, L. L. Schick, K. R. Hardy, R. Wagai, and J. McCarthy, "Organic matter in small mesopores in sediments and soils," *Geochim. Cosmochim. Acta*, no. 19, pp. 3863–3872, 2004.

[128] B. Ransom, R. Bennett, R. Baerwald, and K. Shea, "TEM study of in situ organic matter on continental margins: occurrence and the monolayer hypothesis," *Mar. Geol.*, vol. 138, pp. 1–9, 1997.

[129] M. J. Buckingham, "Wave propagation, stress relaxation, and grain-to-grain shearing in saturated, unconsolidated marine sediments," *J. Acoust. Soc. Am.*, vol. 108, pp. 2796–2815, 2000.

[130] R. A. Berner, "Burial of organic carbon and pyrite sulfur in the modern ocean: its geochemical and environmental significance," *Am. J. Sci.*, vol. 282, pp. 451–473, 1982.

[131] S. M. Henrichs and W. S. Reeburgh, "Anaerobic mineralization of marine sediment organic matter: rates and the role of anaerobic processes in the oceanic carbon economy," *Geomicrob. J.*, vol. 5, pp. 191–237, 1987.

[132] L. M. Mayer, "Surface area control of organic carbon accumulation in continental shelf sediments," *Geochim. Cosmochim. Acta*, vol. 58, pp. 1271–1284, 1994.

[133] L. M. Mayer, P. A. Jumars, G. L. Taghon, S. A. Macko, and S. Trumbore, "Low-density particles as potential nitrogenous foods for benthos," *J. Mar. Res.*, vol. 51, pp. 373–389, 1993.

[134] D. Anderson, "The effect of parent material and soil development on nutrient cycling in temperate ecosystems," *Biogeochem.*, vol. 5, pp. 71–97, 1988.

[135] H. Tiessen, J. Stewart, and H. Hunt, "Concepts of soil organic matter transformations in relation to organo-mineral particle size fractions," *Plant Soil*, vol. 76, pp. 287–295, 1984.

[136] J. Oades, "The retention of organic matter in soils," *Biogeochem.*, vol. 5, pp. 35–70, 1988.

[137] K. F. Graff, *Elastic Wave Motion in Solids*. Ohio State University Press, Columbus, 1976.

[138] W. H. Prosser, J. Dorighi, and M. R. Gorman, "Extensional and flexural waves in a thin-walled graphite/epoxy tube," *J. Compos. Mater.*, vol. 26, pp. 2016–2027, 1992.

[139] J. T. Dubin, *Sediment characterization using in situ measurements of acoustic properties*. Master's thesis, Univ. of Texas at Austin, Austin, TX, 2018.